Isomer Spectroscopy of ^{254}No

Thesis submitted in accordance with the requirements of the University of Liverpool for the degree of Doctor in Philosophy

by

Craig Gray-Jones

Oliver Lodge Laboratory

June 2008

Abstract

A number of experiments were carried out to clarify the structure and decay path of an isomeric state in ^{254}No [Gh73, He06, Ta06]. A band built on the 1298 keV $K^{\pi} = 8^{-}$ isomer was found. From the observed branching ratios in this band a two-proton configuration is favoured for this state, which further supports our earlier conclusions [He08] that the deformed shell closures in this mass region are at $Z = 100$ and $N = 152$, in contradiction to predictions by Skyrme-Hartree-Fock models [Cha06]. Furthermore, the level scheme of ^{254}No was extended to include a floating band and a systematic of reduced hindrance factors for $\Delta K = 8$ E1 transitions is given.

Acknowledgments

Firstly, I would like to thank Professor P.J. Nolan for allowing me to undertake this research at the University of Liverpool.

My sincere gratitude goes to my supervisor Professor Rolf-Dietmar Herzberg. I was fotunate to find myself under his tuition when completing my MPhys project back in 2003. His dedication, enthusiasm for teaching and sounds in tuneful succession inside the Wankkuri has been an inspiration over the last four years.

I would like to acknowledge the financial support provided by the EPSRC studentship.

Thank you to the academic and technical staff of the Univeristy of Jyväskylä, in particular Paul Greenlees, Steffan Ketelhut, Peter Jones, Sarah Eeckhaudt and Panu Rahkila for their expertise, dedication and hospitality.

Thank you to the academic and technical staff of the Liverpool Nuclear Physics Group, especially Dr. Eddie Paul and Dr. David Joss who were always happy to provide advice and direction.

Many thanks to the members of *Team Herzberg* over the years; thank you to Steven Moon for the funniest incident ever to take place on the slopes of Laajavuori; thank you to Danielle Rostron for the stripey mittens in Frankfurt; thank you to Philippos Papadakis for his jocular back-slapping and thank you to Janne Pakarinen for being our international striker.

Big thank you to my fellow finalists in the Nuclear Medical Imaging Group for all of their funny incidents. Thank you to David Scraggs for jumping out of the plane first and thank you to Alex Grint and David Oxley for picking me up in Vancouver and taking me straight to the beach.

Thank you to the football boys for turning up on time on cold and wet Sunday mornings and thank you to Liverpool's Sub-Aqua Club for cold and wet Sunday mornings!

Finally, I would like to thank my parents Ann and Elved and my sister Louise for their encouragment and support.

Contents

Chapter 1

Introduction

One of the main driving forces in nuclear physics for many years has been the quest to find the next spherical doubly-magic nucleus beyond ^{208}Pb within the region of the super-heavy elements.

It is thought that within this region of high mass and charge there exists an island of stability for nuclei with more than 100 protons. Various models have been put forward in order to predict where the borders of such an island may lie.

Initially, the first attempt to explain nuclear properties at a macroscopic scale was conducted by the liquid-drop model. Under the constraints of this model, the Coulomb repulsion between the protons overcomes the short-range attraction of the strong nuclear force at approximately $Z = 100$, which results in a prediction of the limit of spherical stability. This misconception was overcome by the introduction of quantal shell effects. The shell model formulated the concept of a specific arrangement of the nucleons within the nucleus and supported the experimental observation of enhanced nuclear stability at magic nucleon numbers 2, 8, 20, 28, 50, 82 and 126 for neutrons and 2, 8, 20, 28, 50, 82 for protons

Advancements built on the shell model have engineered various predictions as to where the next quantum shell closures may lie. Although the different approaches favour a variety of spherical proton and neutron magic numbers, they all agree on the idea of an island of stability.

Broadly, the theoretical approaches fall into two categories; macroscopic-microscopic models and self-consistent mean-field models. Macroscopic-microscopic models are composed of an oscillatory component described by the shell model and a smoothly varying component described by the liquid-drop model. Self-consistent mean-field models are formed from an iterative procedure and are a true implementation of the shell model. Both models are discussed in Chapter 2.

Figures 1.1 and 1.2 present a comparison of the models and approaches in the form of contour and density plots in the super-heavy region. The shell energy is displayed as a function of neutron and proton number to compare the relative strengths of shell effects. In the Woods-Saxon macroscopic-microscopic case (bottom panel of Figure 1.1), the shell energy is calculated by subtracting the spherical part of the macroscopic energy from the total binding energy. For the Hartree-Fock calculations

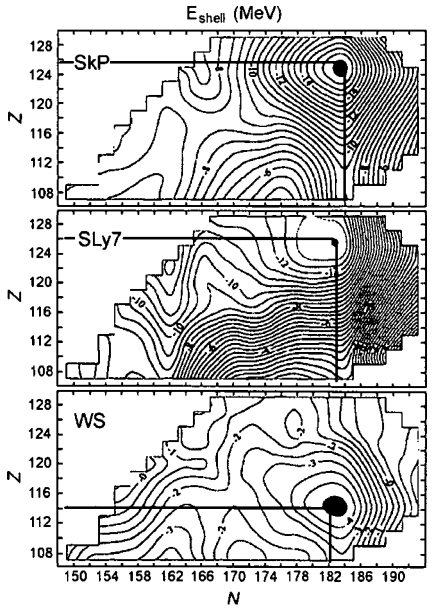

Figure 1.1: Shell correction energies calculated using two different parameterisations of the Skyrme-Hartree-Fock approach (two upper panels) and a Woods-Saxon macroscopic-microscopic approach (bottom panel) [Ćw96].

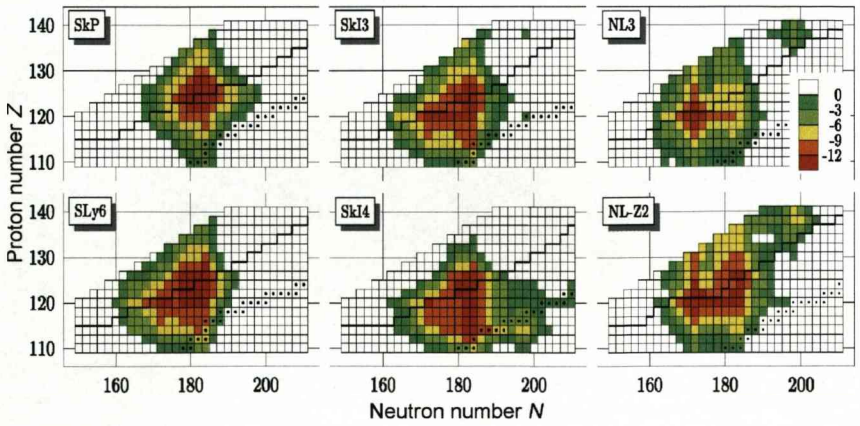

Figure 1.2: Total shell correction energy calculated for super-heavy nuclei around the expected island of stability. Calculations are the result of several parameterisations of the Skyrme-Hartree-Fock and relativistic mean-field approaches within the self-consistent mean-field model [Be01].

(the two upper panels of Figure 1.1) the same spherical part of the macroscopic energy is subtracted from the self-consistent ground-state energy. The area of strongest shell stability is marked in burgundy. The two Hartree-Fock calculations (SkP and SLy7 parameterizations) predict a shell gap around ($Z = 126$, $N = 184$). The macroscopic-microscopic calculations point towards a shell gap at ($Z = 114$, $N = 182$).

Calculations performed by Bender [Be01], predict a broad area of shell stabilization around $Z = 120$ and $N = 172$-184. The calculations were performed using different parameterisations of Skyrme-Hartree-Fock and relativistic mean-field models. The magic numbers for $Z,N \leq 82$ are reproduced by clearly defined sharp decreases in shell correction energy by the different parameterizations. This contrasts with the wide area of stability predicted in the super-heavy region, displayed in Figure 1.2, which is a consequence of the large single-particle level density and the occurrence of many low-j shells around the Fermi level.

It is a major challenge experimentally to investigate the single-particle levels in super-heavy nuclei. Experimentalists are met with the obstacle of extremely low

production cross-sections, for example, a high-spin K isomer was reported in the synthesis of the nucleus ^{270}Ds by Hofmann *et al.* [Ho01], which would provide an ideal hunting ground for information on single-particle states, but in total only eight α-decay chains were measured over a period of seven days.

An alternative approach is the study of relatively lighter well deformed nuclei in the $Z = 102$ region. Here, production cross-sections allow detailed spectroscopy (approximately 100 α-decays detected per hour for an in-beam analysis in this study), and deformation leads to the higher energy spherical single-particle orbitals around $Z = 120$ decreasing in energy and lying at or close to the Fermi surface. The spin orbit partners $2f_{7/2}$ and $2f_{5/2}$ are of special interest here because the size of a possible $Z = 114$ shell gap is directly linked to the strength of the spin-orbit interaction, discussed in Chapter 5.

Chapter 2

Theoretical Framework

This chapter begins by developing the description of the properties of the nucleus from a classical macroscopic procedure towards a microscopic approach. We shall discuss the nuclear properties relevant to this study and also outline nuclear decay modes which are used for tools for analysis in later chapters. The final section will address isomeric states and will focus on the type of isomer applicable to this investigation. This chapter is based upon [Ca00, Hey04, Kr88, Ri04].

2.1 The liquid-drop model

The liquid-drop model (LDM) was one of the first models proposed to explain the properties of the nucleus. The liquid drop is held together by its surface tension, representing a short-range attractive force holding the nucleus together. The short-range interaction has a hard repulsive core which results in the incompressibility of the nucleus. This imposes the condition that the total volume remains constant with a surface radius approximately equal to $1.2A^{1/3}$ fm. We may think of nuclear fission as the separation of the liquid drop into two fragments and the emission of particles in terms of the evaporation of molecules from the liquid surface.

This analogy also extends to the variation of binding energy per nucleon. The binding energy of a nucleus is defined as the energy required to break up the nucleus

into its constituent neutrons and protons. The mass of a nucleus bound by energy BE is less than the mass of its constituent particles by BE/c^2. Experimentally, it is revealed that the binding energy per nucleon is approximately constant for A greater than about 20, indicating that each nucleon only interacts with its nearest neighbours. This implies that the nuclear force saturates with increasing mass. The variation of the nuclear binding energy as a function of mass is described by the semi-empirical Bethe-Weizsäcker formula, derived from the LDM in order to produce a more satisfactory account of the binding-energy saturation, and is prescribed as follows

$$BE(A,Z) = a_v A - a_s A^{2/3} - a_c Z(Z-1) A^{-1/3} - a_A (A-2Z)^2 A^{-1} \pm \delta. \quad (2.1)$$

The four terms accompanied by subscripts on the right-hand side of the equation are referred to as the volume, surface, Coulomb and symmetry energy terms. The volume term $(a_v A)$ accounts for the saturation of the nuclear force permitting a contribution to the binding energy from within the nuclear volume. However, nucleons near to the surface have fewer nearest neighbours than within the interior and therefore we are required to subtract a surface term $\left(a_s A^{2/3}\right)$. A further reduction in binding energy results from electromagnetic repulsion of the protons which is compensated by the Coulomb term $\left(a_c Z(Z-1) A^{-1/3}\right)$. The Coulomb repulsion has an infinite range and as a consequence each proton feels the repulsion of all of the others.

Two further modifications, which have no classical basis, are included for the purpose of improving the reproduction of the experimental variation of binding energy. To account for the actuality that light nuclei with $N = Z$ are more stable than nuclei where $N > Z$ a symmetry term $\left(a_A (A-2Z)^2 A^{-1}\right)$ is incorporated. This term becomes less significant at large A due to the increase in Coulomb repulsion which necessitates extra neutrons for screening. Finally, a pairing term (δ) is included to account for the tendency of like nucleons to couple in pairs. The term is positive for even-even nuclei $(+a_p A^{-3/4})$, zero for odd-even nuclei and negative for odd-odd nuclei $(-a_p A^{-3/4})$. A particular choice of $a_v = 15.5$ MeV, $a_s = 16.8$ MeV, $a_c = 0.72$ MeV, $a_A = 23$ MeV and $a_p = 34$ MeV reproduce the observed behaviour of binding energy rather well [Kr88].

However, the LDM does stray from experimental evidence. Figure 2.1 illustrates the deviations between the experimental and liquid-drop model values for the binding energies. The pronounced peaks are a confirmation of the magic numbers (Z or N = 2, 8, 20, 28, 50, 82 and $N = 126$) and are a demonstration that nuclei with these values of protons and neutrons are more highly bound than the values generated by the LDM.

2.2 The shell model

The discontinuities observed in Figure 2.1 arise due to a quantum shell structure and this observation supplied the motivation for the formulation of the nuclear shell model. Further experimental evidence includes the anomalously high first-excited 2^+ states of even-even nuclei with Z or N near the magic numbers. This is due to the extra energy required to excite a nucleon from a closed shell compared to the energy required for the rearrangement of nucleons within an unfilled shell. Also, the

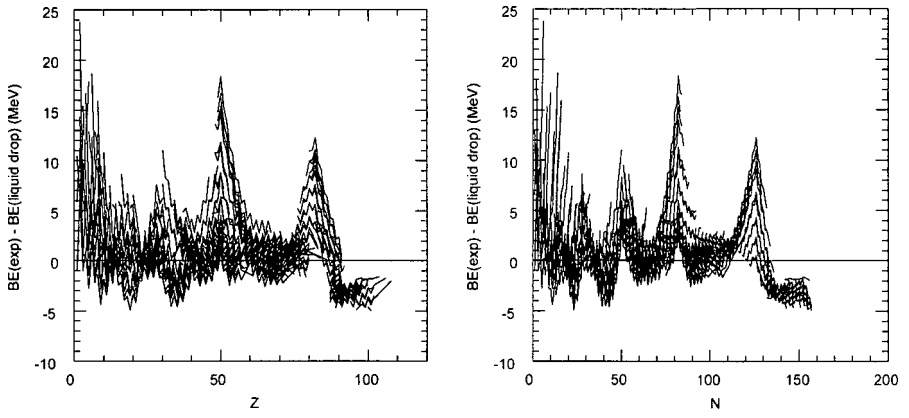

Figure 2.1: Values for the difference between experimental and the liquid drop model binding energies as a function of Z (left) and N (right). One observes distinct peaks for values of Z and N at 28, 50, 82 and additionally $N = 126$, indicating that these nuclei are more bound than average. Figure modified from reference [Br05].

quadrupole moments, proportional to nuclear deformation, are at a minimum for nuclei with magic numbers, indicating a spherical shape.

The assertion is made that the shell structure possessed by the nucleus is analogous to that exhibited by the atomic electrons. The nucleons are fermions and are governed by the Pauli exclusion principle, thus occupying states accordingly. Unlike the atomic case, the constituents are relatively free from collisions, allowing the nucleons to move in almost unperturbed single-particle orbits within the nucleus. Another alteration to the atomic model is that for the nuclear case the motion of a single nucleon is guided by the average potential of all of the nucleons. This creates an average smoothed-out interaction with all of the other particles, defined as the mean field potential.

If we consider the actual short-range interaction potential $v(r_{ij})$ between the nucleons, i and j, then the average potential acting on each particle is

$$V_i(r_i) = \left\langle \sum_j v(r_{ij}) \right\rangle . \tag{2.2}$$

The Hamiltonian is given by

$$H = \sum_i T_i + \sum_{ij} v(r_{ij}) , \tag{2.3}$$

which can be disassembled into a central interaction and residual interaction part

$$H' = \sum_i [T_i + V_i(r_i)] + \left[\sum_{ij} v(r_{ij}) - \sum_i V_i(r_i) \right] . \tag{2.4}$$

The assumption of the shell model is to neglect the last term in Equation 2.4.

The question arises as to the form of the central potential. A number of possible choices are illustrated in Figure 2.2. The Woods-Saxon model represents the most realistic potential but it proves more difficult to solve than the harmonic oscillator potential, which although unrealistic, does reproduce the correct magic numbers with the aid of modifications.

2.2.1 The harmonic-oscillator potential

We may express the harmonic oscillator as

$$V_{HO}(r) = -V + \frac{1}{2} m\omega^2 r^2, \tag{2.5}$$

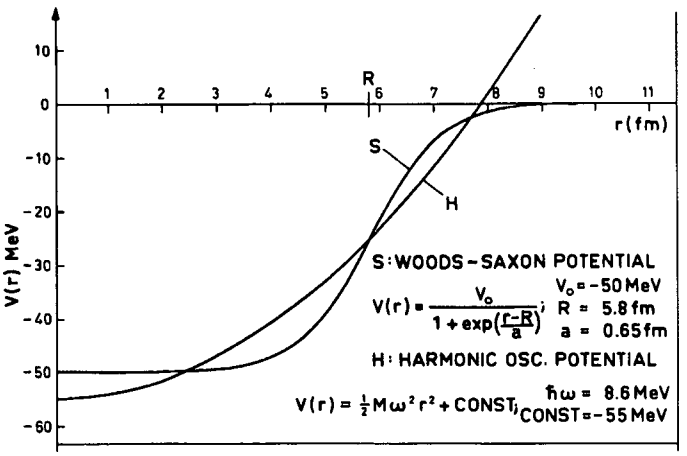

Figure 2.2: A comparison of potential wells which have been used to model the nuclear potential. Figure adapted from reference [Bo98].

where V is the well depth, m is the mass of the nucleon, ω is the frequency of the simple harmonic motion of the nucleon and r is the distance from the origin. Following from the previous discussion, the harmonic oscillator represents an unphysical potential, since the potential tends to infinity for large r. However, this is tolerated because only the exponential tail of the wavefunctions are effected and that an analytical solution is forthcoming. Using the harmonic oscillator to solve the Hamiltonian gives rise to a set of energy levels

$$E_N = \left(N + \frac{3}{2}\right)\hbar\omega, \tag{2.6}$$

where N is the total number of oscillation quanta. For each vales of N there is a degenerate set of levels defined by a value of orbital angular-momentum quantum number l, given by $N = (2n + l)$, where n is the radial quantum number.

Each N oscillator shell is $(N+1)(N+2)$ degenerate and the values of orbital angular momentum permitted are

$$l = N,\ N-2,\ N-4\ldots. \tag{2.7}$$

N	Allowed l	Occupation	Total
0	0	2	2
1	1	6	8
2	2,0	12	20
3	3,1	20	40
4	4,2,0	30	70
5	5,3,1	42	112

Table 2.1: Table showing the derivation of the total cumulative occupations generated by the harmonic-oscillator potential. The total cumulative occupations disagree with the experimentally observed magic numbers.

Each oscillator shell will only contain states of equal parity given by

$$\pi = (-1)^N = (-1)^l . \tag{2.8}$$

This description only reproduces the first three magic numbers, failing to agree with experimentally determined values for higher N shells, presented in Table 2.1.

By introducing an attractive force proportional to l^2 we can produce a potential that is intermediate between that of the harmonic oscillator and the square well. The main purpose of the term is to reduce the harmonic oscillator potential at large radii to correct the deficiency described earlier in this section. This term flattens the effective radial shape of the potential. As the orbital angular momentum of the particle increases so do the effects of the l^2 term. At high angular momentum particles feel a stronger attractive interaction that lowers their energies. This creates a more attractive potential at larger radii due to particles with large angular momentum spending a greater period of time at large radii because of the centrifugal force. Also, as a result, this provides a more constant interior potential.

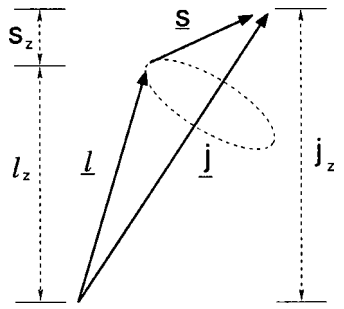

Figure 2.3: The components of spin-orbit coupling. The nucleon orbital angular momentum $\underline{l}$ and intrinsic spin $\underline{s}$ precess about the direction of the total angular momentum $\underline{j}$. Figure modified from reference [Pau03].

2.2.2 Spin-orbit coupling

A spin-orbit term is introduced to the potential in order to reproduce the magic numbers more accurately. The term draws on an analogous interaction observed in atomic physics. There, a spin-orbit interaction stems from the magnetic moment of an electron interacting with the magnetic field generated by its motion about the nucleus. The electromagnetic spin-orbit contribution is actually small in the nucleus and most of it comes from the nuclear forces which have an explicit spin-orbit dependence.

Due to the coupling of the nucleons orbital and intrinsic spin angular momentum a spin-dependent force may be considered. This force is added to the harmonic-oscillator potential and has the form

$$V(r) \rightarrow V(r) + V_{SO}; \quad V_{SO} = f(r)\,\underline{l}.\underline{s}; \quad f(r) = \lambda \frac{1}{r}\frac{d}{dr}V(r) \tag{2.9}$$

where *f(r)* is the strength of the spin-orbit coupling and $\lambda \approx 0.5$ fm^2. The angular momenta precesses around the total angular momentum $\underline{j}$, Figure 2.3, which is equal to the vector sum of the the nucleon orbital angular momentum $\underline{l}$ and intrinsic spin $\underline{s}$. The spin-orbit potential acts to split the degenerate levels with $j = l \pm s$, except for $l = 0$, in which case only $j = \frac{1}{2}$ is allowed. The splitting is proportional to $(2l + 1)$, therefore the magnitude of the splitting increases as l increases. It is observed that $j = l + \frac{1}{2}$ states are lower in energy than $j = l - \frac{1}{2}$, this is due to the attractive nature

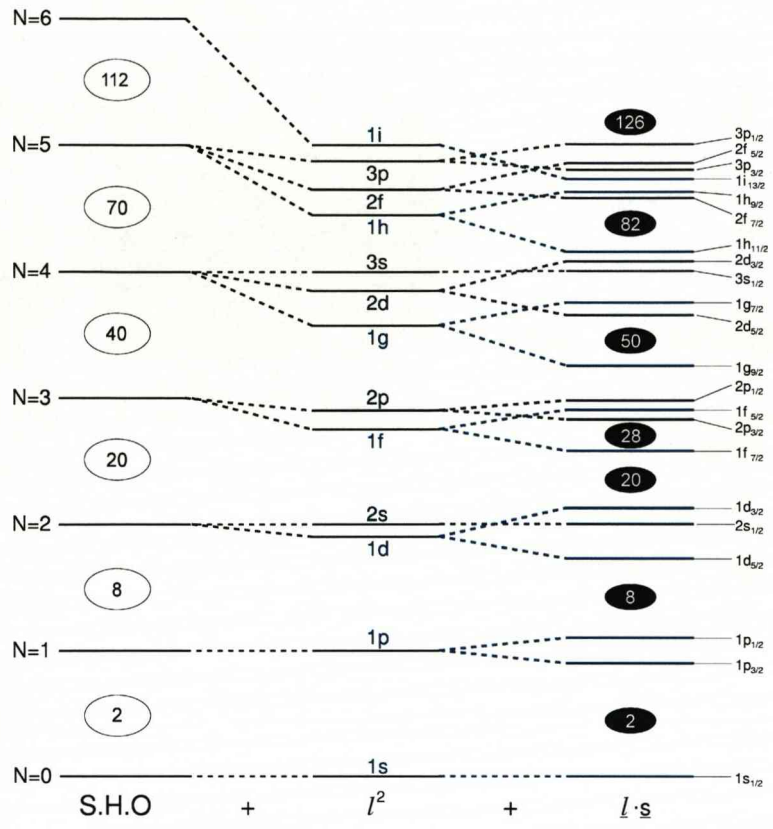

Figure 2.4: Sequences of bound single-particle states near stability. The harmonic-oscillator shells are shown to the left. In the centre, a l^2 term is incorporated to produce a more realistic potential. A spin-orbit term $\underline{l}.\underline{s}$ is added to the right with its strength adjusted to obtain the correct nuclear magic numbers. The final shell model states are labelled nl_j, where the orbital angular momentum $l = 0, 1, 2, 3\ldots$ is denoted by the conventional atomic notation $l =$ s, p, d, f,.... Figure modified from reference [Pau03].

of the interaction. The energy levels can be lowered sufficiently enough to interleave certain states with those of $(N - 1)$. These levels are termed unnatural parity or intruder states. The modifications performed by the inclusion of the l^2 term and the spin-orbit force results in a theoretical reproduction of the experimentally observed magic numbers, Figure 2.4.

2.3 Nuclear properties

The shell model works best for light nuclei. This is because the model is tractable in light nuclei due to smaller model spaces. The model, with a proper treatment of residual interactions, describes nuclei near closed shells and with valence nuclei confined to a single j shell exceptionally well. However, the transfermium nucleus under investigation in this study is far from closed shells, and within this region of the nuclear table the shell-model calculations become intractable due to the rapidly increasing model spaces.

2.3.1 Deformation

As we move away from spherical doubly-magic nuclei in the table of nuclides we approach large areas of deformed nuclei. Evidence for deformation is observed in the form of collective level schemes, resulting from the coherence in the nuclear single-particle motion, and large intrinsic quadrupole moments.

The surface of the nucleus may be described by a radius vector, $R(\theta, \phi)$, expressed as a sum over spherical harmonics $Y_\lambda^\mu(\theta, \phi)$, pointing from the origin to the surface

$$R(\theta, \phi) = C(\alpha_{\lambda\mu}) R_0 \left[1 + \sum_{\lambda=0}^{\infty} \sum_{\mu=-\lambda}^{\lambda} \alpha_{\lambda\mu} Y_\lambda^\mu(\theta, \phi) \right], \tag{2.10}$$

where R_0 is the radius of a sphere having the same volume as the deformed nucleus, the coefficients $\alpha_{\lambda\mu}$ represent distortions from an equilibrium shape and the factor $C(\alpha_{\lambda\mu})$ is introduced to satisfy the condition of conservation of volume. The classification of the deformation multipole is denoted by λ, and μ is an integer signifying the deviation from axial symmetry within the range $-\lambda \leq \mu \leq \lambda$.

The lowest multipole considered, $\lambda = 2$, defines a spheroidal shape with quadrupole deformation ($\lambda = 3$ and 4 describe octupole and hexadecapole shapes). For an axially symmetric deformation (about the z-axis) $\alpha_{\lambda\mu}$ vanishes except when $\mu = 0$, this leads to the deformation parameters $\alpha_{\lambda 0}$ being written as β_λ. If coordinates are used relative to the body-fixed axes then $\alpha_{21} = \alpha_{2-1} = 0$ and $\alpha_{22} = \alpha_{2-2}$. The system may then be defined using the coefficients α_{20} and α_{22} and the three Euler angles.

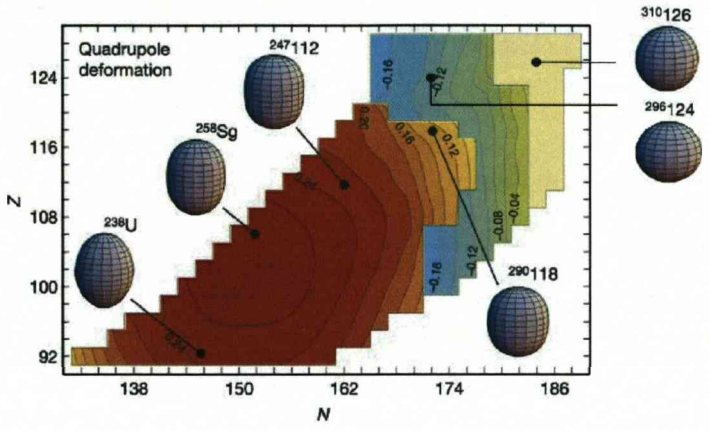

Figure 2.5: Predicted ground state mass quadrupole deformation β_2 for even-even heavy and super-heavy nuclei. The nucleus under investigation in this study, ^{254}No, lies within a region of well-deformed prolate shapes ($\beta_2 > 0$) coloured red-orange. Oblate shapes ($\beta < 0$) are blue-green, and spherical shapes ($\beta_2 = 0$) are light yellow. Figure modified from reference [Ćw05].

We may express the coefficients in terms of a polar-coordinate representation (β and γ) of the nuclear shape. For the quadrupole case:

$$\alpha_{20} = \beta_2 \cos\gamma; \;\; \alpha_{22} = \alpha_{2-2} = \left(1/\sqrt{2}\right) \beta_2 \sin\gamma. \tag{2.11}$$

From which we obtain

$$\beta_2^2 = \sum_{\mu} |\alpha_{2\mu}|^2 , \tag{2.12}$$

where β_2, the quadrupole deformation parameter, is the sum of the coefficients, measuring the amount of deformation of the nucleus. The larger the value of β_2 the greater the distortion of the nucleus. Figure 2.5 illustrates the ground-state shape elongations predicted in the super-heavy region. The parameter γ measures the lengths along the principal axes. A value of $\gamma = 0°$ corresponds to a prolate shape with the z axis as the symmetry axis.

2.3.2 Collective nuclear rotation

Collective rotation of a spherical nucleus about an axis of symmetry is forbidden because states generated by such rotations are indistinguishable from each other. However, in this area of study nuclei exhibit significant deformation, thus permitting a nuclear orientation to be defined and allowing a rotational degree of freedom.

The total angular momentum $\underline{I}$ of an axially symmetric deformed nucleus rotating about an axis perpendicular to the symmetry axis is composed of two parts, a collective angular momentum $\underline{R}$, generated by the rotation of the core of the nucleus, and $\underline{J}$, the sum of the intrinsic angular momenta of the individual valence nucleons,

$$\underline{I} = \underline{R} + \underline{J}, \tag{2.13}$$

$$\text{and } \underline{J} = \sum_{i=1}^{A} \underline{j}_i, \tag{2.14}$$

where i is the number of valence nucleons and $\underline{j}$ is the intrinsic angular momentum. A schematic representation of the angular momentum coupling for a prolate rotating nucleus is given in Figure 2.6. The rotational frequency is represented by the parameter ω and the quantum number K is the projection of the total intrinsic angular momentum onto the symmetry axis, thus $K = \sum_{i=1}^{A} \Omega_i$, where Ω is the projection of the angular momentum of a valence nucleon onto the symmetry axis. For an even-even nucleus the nucleons will couple to give a net spin of zero in the ground state, thus if $\underline{J} = 0$ then the total angular momentum is generated by the coherent rotational motion, $\underline{I} = \underline{R}$.

By considering the energy possessed by a rigid rotating body then one can obtain the energy levels of the collective nuclear rotation, given by

$$E(I) = \frac{\hbar^2}{2\Im^{(0)}} I(I+1), \tag{2.15}$$

where $\Im^{(0)}$ is the static moment of inertia. A sequence of excited nuclear states is formed by increasing the quantum number I, thus forming a rotational band. The ground-state rotational band of an even-even nucleus will only contain a sequence of

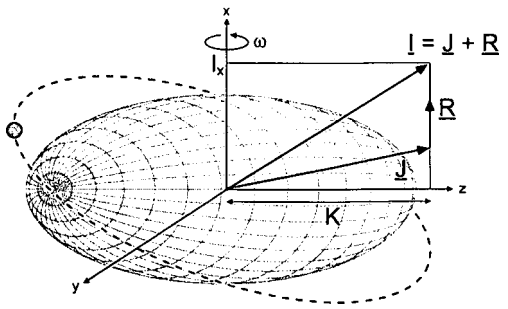

Figure 2.6: Schematic representation of the coupling of the collective angular momentum and the sum of the intrinsic angular momenta of the individual valence nucleons. The rotation and symmetry axes are labelled x and z. Figure adapted from reference [Pau03].

rotational states of even values of I due to the invariance of the nucleus rotating by 180° about the rotation axis.

In a deformed nuclear system the frequency of the coherent rotation of the nucleus about the rotation axis is related to I by

$$\hbar\omega \equiv \frac{dE}{dI_x} \approx \frac{1}{2}\left[E_{I+1} - E_{I-1}\right] \text{ when } I \gg K, \tag{2.16}$$

where the projection of I onto the axis of rotation is given by the aligned angular momentum

$$I_x = \sqrt{I(I+1) - K^2}. \tag{2.17}$$

For an even-even nucleus the ratios of the energy levels of a rotor are $E(4^+)/E(2^+)$ = 3.333 and $E(6^+)/E(2^+) = 7.0$ which can be used as a signature for identification of a rotational band. Table 2.2 lists several examples of even-even nuclei which exhibit good rotational behaviour.

Calculations of a rigid-body moment of inertia for nuclei are greater than the experimentally measured moments of inertia and therefore the nucleus does not behave strictly as a rigid body. Additionally, the nucleus does not behave implicitly as a superfluid since the measured moments of inertia are greater than those calculated

Nuclide	$E(4^+)/E(2^+)$	$E(6^+)/E(2^+)$	Reference
^{172}Yb	3.3052 *1*	6.8573 *1*	[Fi96]
^{178}Hf	2.29061 *5*	6.7845 *1*	[Fi96]
^{254}No	3.32 *2*	6.945 *7*	This data

Table 2.2: Examples of even-even nuclei which exhibit good rotational behaviour.

for an irrotational flow. This behaviour is a consequence of short-range pairing correlations. Consequently, the nucleus under rotation can be considered as a rigid core plus a fluid of valence nucleons.

For the purpose of describing the behaviour of the collective rotation of the deformed nuclear system we introduce two spin-dependent moments of inertia, related to the first- and second-order derivatives of the excitation energy with respect to the aligned angular momentum I_x. The following formulae are obtained under the assumption that the nucleus is at high spin $I \gg K$ and that $I_x \approx I$.

The kinematic moment of inertia is due to the motion of the system (the ratio of angular momentum to angular frequency) and is given by

$$\Im^{(1)} = \left(\frac{dE}{dI_x}\right)^{-1} \hbar^2 = \hbar\frac{I_x}{\omega}, \tag{2.18}$$

which can be related to the transition energies E_γ of a rotating system by

$$E_\gamma = \frac{\hbar^2}{2\Im^{(1)}}\,(I-2)\,. \tag{2.19}$$

The dynamic moment of inertia is the response of the system to a force and is given by

$$\Im^{(2)} = \left(\frac{dE^2}{dI_x^2}\right)^{-1} \hbar^2 = \hbar\frac{dI_x}{d\omega}, \tag{2.20}$$

which is related to the difference in energy between two consecutive transitions in a rotational band

$$\Delta E_\gamma = \frac{4\hbar^2}{\Im^{(2)}}. \tag{2.21}$$

The two moments of inertia are related as follows

$$\Im^{(2)} = \frac{dI_x}{d\omega} = \frac{d}{d\omega}\left(\omega\Im^{(1)}\right) = \Im^{(1)} + \omega\frac{d\Im^{(1)}}{d\omega}, \tag{2.22}$$

where $\Im^{(2)} \approx \Im^{(1)}$ in the limit of rigid rotation.

Particle-rotor coupling

The coupling of the intrinsic angular momentum to the collective angular momentum results in a Coriolis interaction which couples the degrees of freedom of the valence nucleons and the rotor core [Pau03]. Depending on the strength of the Coriolis interaction the coupling lies between two extremes, deformation alignment (DAL) and rotation alignment (RAL), illustrated in Figure 2.7.

For large deformations and low rotational frequencies, DAL occurs in which the angular momentum vectors precess around the deformation axis. At this point the Coriolis force is low and the single-particle orbits cannot be aligned with the rotation axis. For deformation alignment K is a good quantum number and a rotational band

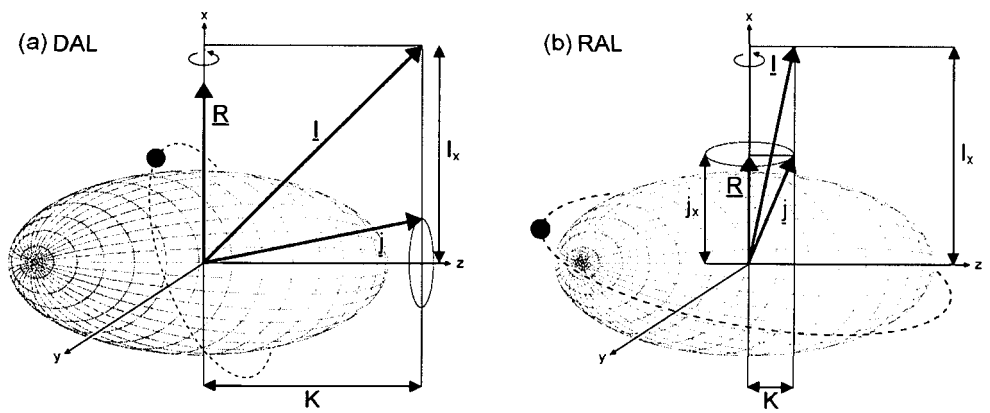

Figure 2.7: Particle rotor coupling schemes. Diagram (a) illustrates the strong-coupling limit or deformation-aligned (DAL) coupling scheme. Diagram (b) illustrates the weak-coupling limit or rotation-aligned (RAL) coupling scheme. The rotation and symmetry axes are labelled x and z. The projection of the total spin on the symmetry axis is labelled K. Figure adapted from reference [Pau03].

with spin $I = K$, K+1, K+2... is observed with energies given by

$$E_{rot} = \frac{\hbar^2}{2\Im^{(0)}} \left[I\left(I+1\right) - K^2 \right]. \tag{2.23}$$

For smaller deformations and rapid rotational frequencies RAL occurs. The Coriolis force is strong enough to align the angular momentum of the valence nucleon to the rotational angular momentum, thus $\underline{j}$ precesses about the rotation axis. In this limit, the rotation has spin $I = j$, j+2, j+4... and the energies are given by

$$E_{rot} = \frac{\hbar^2}{2\Im^{(0)}} \left(I - j_x\right)\left(I - j_x + 1\right). \tag{2.24}$$

2.3.3 Pairing

The pairing interaction is defined to be an attractive interaction acting on two identical nucleons in the same j orbit in total angular momentum $I^\pi = 0^+$ states. At the point of greatest spatial overlap the pairing interaction would be energetically favoured. However, the Pauli exclusion principle forbids the two nucleons from occupying the same orbit, which leads to time-reversal orbits of the nucleons generating the next greatest spatial overlap. Scattering of the pairs of nucleons within time-reversal orbits will occur twice per revolution resulting in occupations of new time reversed orbits of, in general, different energy. Scattering between orbits is dependent upon the availability of free orbitals and therefore this process can only occur near to the Fermi level. This leads to a smearing of the Fermi level if one plots the occupation probability versus the energy of the orbit, Figure 2.8. The energy required to break a pair, the pair-gap parameter, denoted by Δ, confines the smearing within a region of 2Δ.

There exists a number of experimental observables which provide evidence for the concept of pairing [Ca00]. Principally, the ground states of all even-even nuclei have spin $0\hbar$ because the nucleons are coupled pairwise so that their angular momenta cancel. Additionally, even-even nuclei are more bound. Several other features also indicate a requirement for the pairing interaction, including a tendency for deformation

to be inhibited near closed shells where empirically a sequence of spherical nuclei succeeded by a sudden transition region to deformation is observed. Furthermore, the experimentally determined moments of inertia are less than the rigid-body values, suggesting a superfluid behaviour of the nucleus.

With the addition of a two-body monopole pairing interaction the nuclear Hamiltonian H can be expressed as

$$H = H_{sp} + H_{pair} = \sum_{\nu>0} \epsilon_\nu \left[a^\dagger_\nu a_\nu + a^\dagger_{\bar{\nu}} a_{\bar{\nu}}\right] - G \sum_{\nu_1,\nu_2} a^\dagger_{\nu_1} a^\dagger_{\bar{\nu_1}} a_{\bar{\nu_2}} a_{\nu_2}, \tag{2.25}$$

where H_{sp} is the single-particle Hamiltonian, H_{pair} is the pairing Hamiltonian and particle creation and annihilation operators are denoted by $a^\dagger$ and a. The first term on the right-hand side of Equation 2.25 is the sum of the single-particle energies ϵ_ν and refers to the nucleonic motion in the average single-particle field. The pairing term is composed of the pairing interaction that annihilates a pair of particles in the time-reversed states $|\nu_2\rangle$ and $|\bar{\nu_2}\rangle$ and creates a pair of particles in the time-reversed states $|\nu_1\rangle$ and $|\bar{\nu_1}\rangle$ [Pau03].

The strength of the pairing force, G, of the interaction between two nucleons in the same j state, is largest for high j orbitals and since in heavier nuclei the outer

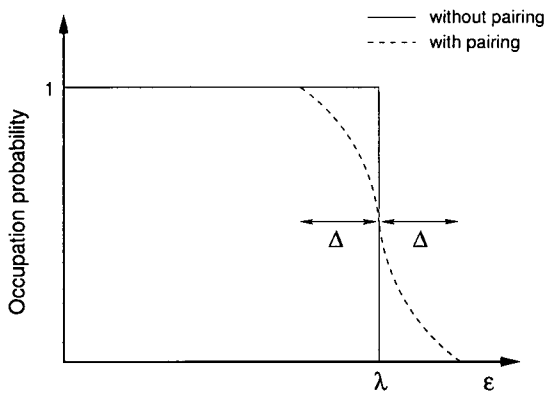

Figure 2.8: A plot of the single-particle occupation probability versus the single-particle energy. The Fermi level is labelled by λ and a smearing is observed due to the pairing interaction. Figure modified from reference [Pau03].

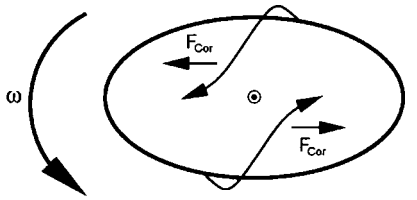

Figure 2.9: An illustration of the Coriolis force, which at high spin, tends to couple pairs from spin zero. The axis of rotation points out of the page [Pau03].

nucleons are further apart the strength will decrease with mass. We should also note that the strength is lower for protons than for neutrons due to Coulomb repulsion. Prescriptions used to define the strength are

$$G_p = \frac{17}{A},\ G_n = \frac{23}{A}\ MeV. \tag{2.26}$$

Pairing may be broken by the action of the Coriolis force which at high spin acts differently upon the time-reversed paired nucleons, decoupling the pairs from $J^\pi = 0^+$. A combination of Coriolis antipairing (a gradual decrease in the pair-gap parameter) and rotational alignment (a pair of valence nucleons are broken by a sufficiently large Coriolis force aligning their angular momenta along the rotation axis) results in the possibility of the nucleus entering an unpaired phase at high spin. Figure 2.9 illustrates the action of the Coriolis force upon pairs of nucleons orbiting a rotating nucleus.

The concept of quasiparticles is introduced replacing the pairwise interacting particles by a gas of noninteracting quasiparticles. The quasiparticle energies are purely additive and the entity may be considered as a mixture of particle and hole states. The probability of occupation of a hole state or a particle state is given by

$$U_i = \frac{1}{\sqrt{2}}\left[1 + \frac{(\epsilon_i - \lambda)}{\sqrt{(\epsilon_i - \lambda)^2 + \Delta^2}}\right]^{\frac{1}{2}},\ V_i = \frac{1}{\sqrt{2}}\left[1 - \frac{(\epsilon_i - \lambda)}{\sqrt{(\epsilon_i - \lambda)^2 + \Delta^2}}\right]^{\frac{1}{2}}, \tag{2.27}$$

$$\text{and } U_i^2 + V_i^2 = 1, \tag{2.28}$$

where ${U_i}^2$ is the probability that the orbit i is occupied by a hole state and ${V_i}^2$ is the probability that the orbit i is occupied by a particle state; the Fermi energy is denoted by λ, ϵ_i is the single-particle energy, and Δ is the earlier defined pair-gap parameter. For states below the Fermi level ($\epsilon_i \ll \lambda$) ${V_i}^2 = 1$ and ${U_i}^2 = 0$, the reverse is true for states far above the Fermi level and the occupation probabilities are mixed near the Fermi level. The quasiparticle energy of a state relative to the ground state is

$$E_i = \sqrt{(\epsilon_i - \lambda)^2 + \Delta^2}, \tag{2.29}$$

and the pair gap parameter may be expressed as

$$\Delta = G \sum_i U_i V_j. \tag{2.30}$$

2.4 Nuclear models

Microscopic models will be discussed in the following subsections which, unlike the the spherical shell model, can describe nuclear systems which deviate from sphericity and which contain large numbers of valence nucleons. The final subsection examines a macroscopic-microscopic approach which lays a foundation for understanding the relative stability of nuclei with $Z \gtrsim 100$.

2.4.1 The Nilsson model

A model is required which uses a deformed nuclear potential in order to describe nuclei with permanent deformation. In 1955, Nilsson [Ni55] proposed that a deformed nuclear potential can be described by an anisotropic harmonic-oscillator potential. The model considers a valence single particle undergoing rapid orbital motion around an axially symmetric deformed core of relative stationary motion. The Nilsson Hamiltonian can be written as follows

$$H_{Nil} = \frac{-\hbar^2}{2m}\nabla^2 + \frac{m}{2}\left(\omega_x^2 x^2 + \omega_y^2 y^2 + \omega_z^2 z^2\right) - \kappa\hbar\omega_0 \left[2\underline{l}.\underline{s} - \mu\left(l^2 - \left\langle l^2 \right\rangle_N\right)\right], \tag{2.31}$$

where the term $(\underline{l}.\underline{s})$ is the spin-orbit force and the term $(l^2 - \langle l^2 \rangle_N)$ was introduced to flatten the radial shape of the potential. The parameters κ and μ determine the strength of the spin-orbit term and the squareness of the potential and are fitted such that the observed levels in deformed nuclei are reproduced. The parameters κ and μ are different for each major shell. The $\omega_{x,y,z}$ terms are the one-dimensional oscillator frequencies in the x,y and z directions and are expressed in terms of the nuclear deformation parameter ϵ, which for normal nuclear deformation is approximately 0.95β. In the axially symmetric case (where the z-axis is taken as the symmetry axis)

$$\omega_x^2 = \omega_y^2 = \omega_0^2 \left(1 + \frac{2}{3}\epsilon\right), \ \omega_z^2 = \omega_0^2 \left(1 - \frac{4}{3}\epsilon\right) \tag{2.32}$$

The term ω_0 is the oscillator frequency ($\hbar\omega_0 = 41A^{-1/3}$ MeV) in the spherical potential with $\epsilon = 0$. A prolate deformation elongates the nucleus in the z direction and thus for $\epsilon > 0$ ω_z will decrease with increasing deformation but ω_x and ω_y will increase. A plot of single-particle energy versus deformation is known as a Nilsson diagram. Examples for protons with $Z \geq 82$ and for neutrons with $N \geq 126$ are shown in Figures 2.11 and 2.12.

The energy levels of the Nilsson diagram are labelled by the asymptotic quantum numbers

$$\Omega^\pi \left[N n_z \Lambda\right], \tag{2.33}$$

where N is the total number of oscillator quanta, n_z is the number of oscillator quanta along the symmetry axis, Λ is the projection of the orbital angular momentum (l) onto the symmetry axis, and Ω, equal to $\Lambda \pm \Sigma$, is the projection of the total angular momentum (j) onto the symmetry axis, where Σ is the projection of the intrinsic spin of the nucleon onto the symmetry axis $\left(= \pm\frac{1}{2}\right)$, thus $\Omega = \Delta \pm \frac{1}{2}$. The parity π is determined by $(-1)^N$. The asymptotic quantum numbers are shown schematically in Figure 2.10.

There are several unique characteristic features of the Nilsson diagram from which one can derive information [Ca00]. At zero deformation ($\epsilon = 0$) the orbitals are $2j+1$ fold degenerate, at non-zero values of ϵ the orbitals split up into $(2j+1)/2$ levels,

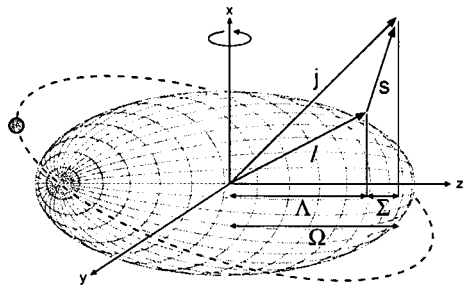

Figure 2.10: Illustration of the labelling of the asymptotic quantum numbers. Figure adapted from reference [Pau03].

each of which still has two fold degeneracy of $\pm\Omega$. Levels with lower Ω are shifted downwards for positive (prolate) deformations and upwards for negative (oblate) deformations. If we consider a valence nucleon orbiting a prolate deformed nucleus then the angle of an orbital plane (between the orbital and the symmetry axis) is expressed as $\theta = \sin^{-1}(K/j)$. A low K value corresponds to equatorial motion, close to the bulk of nuclear matter and hence lower in energy. Further to this, θ changes slowly for low K values and rapidly for high K values. Therefore the difference in energy between K values increases rapidly for higher values of K. The only good quantum numbers of these orbits are Ω and π. Due to the Pauli exclusion principle when two lines of the same Ω and parity approach each other they must repel and thus change their slope. This has the effect of configuration mixing of different j values on the resulting energy variations of the discussed K splitting if two like orbitals become close and repel. In Figure 2.11 we view the $i_{13/2}$ orbit, with $l = 6$. The orbital has positive parity and lies in an area of predominantly negative parity orbits. Having opposite parity it cannot mix with any other orbits and is therefore extremely pure and extends continuously in the same direction without curving for large deformation. This is also the case for high-K orbitals since it is unlikely that there will be orbits of equal K in close proximity.

The total energy of the nucleus can be estimated by summing all of the energies

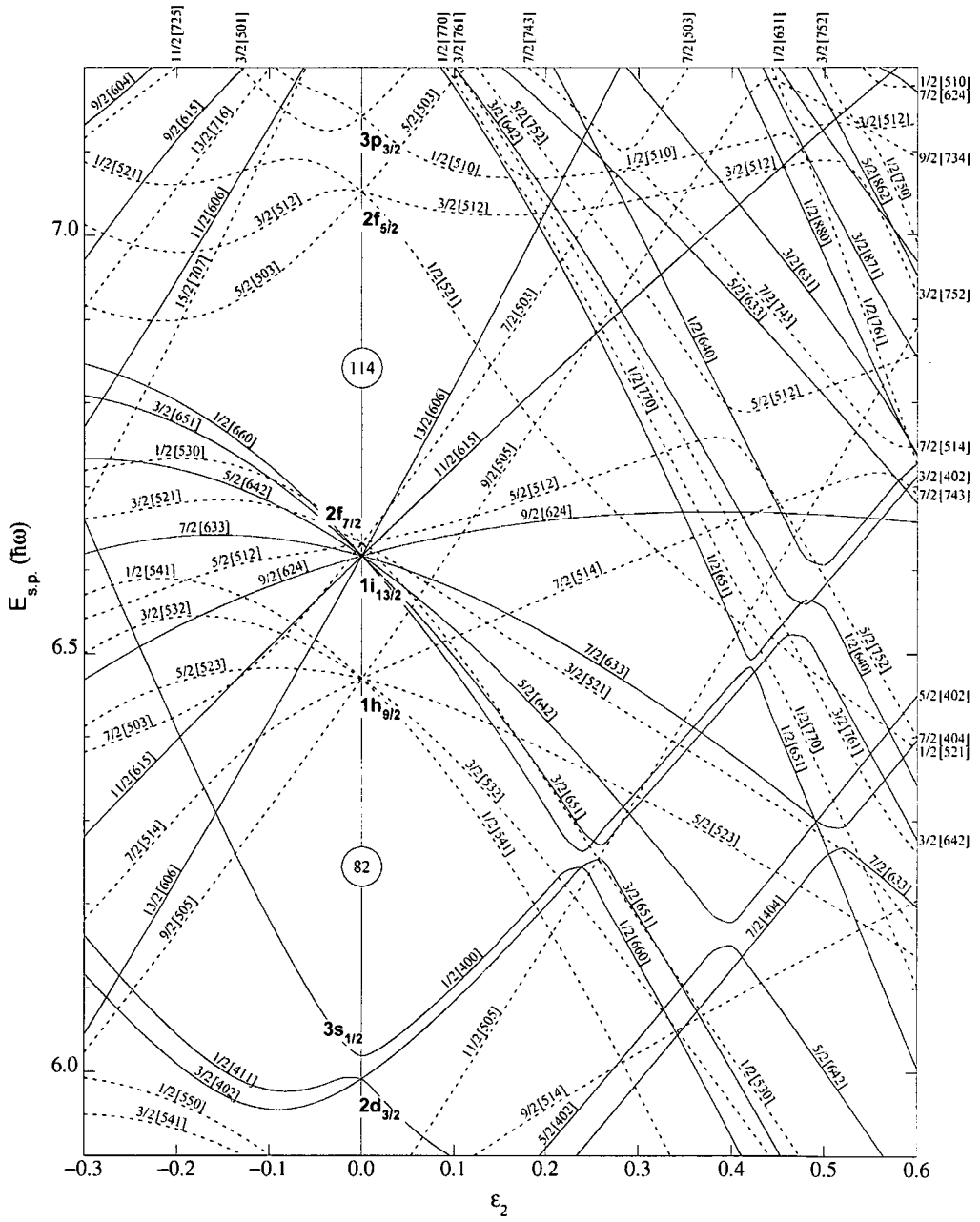

Figure 2.11: The Nilsson states for protons $Z \geq 82$. Figure taken from reference [Fi96].

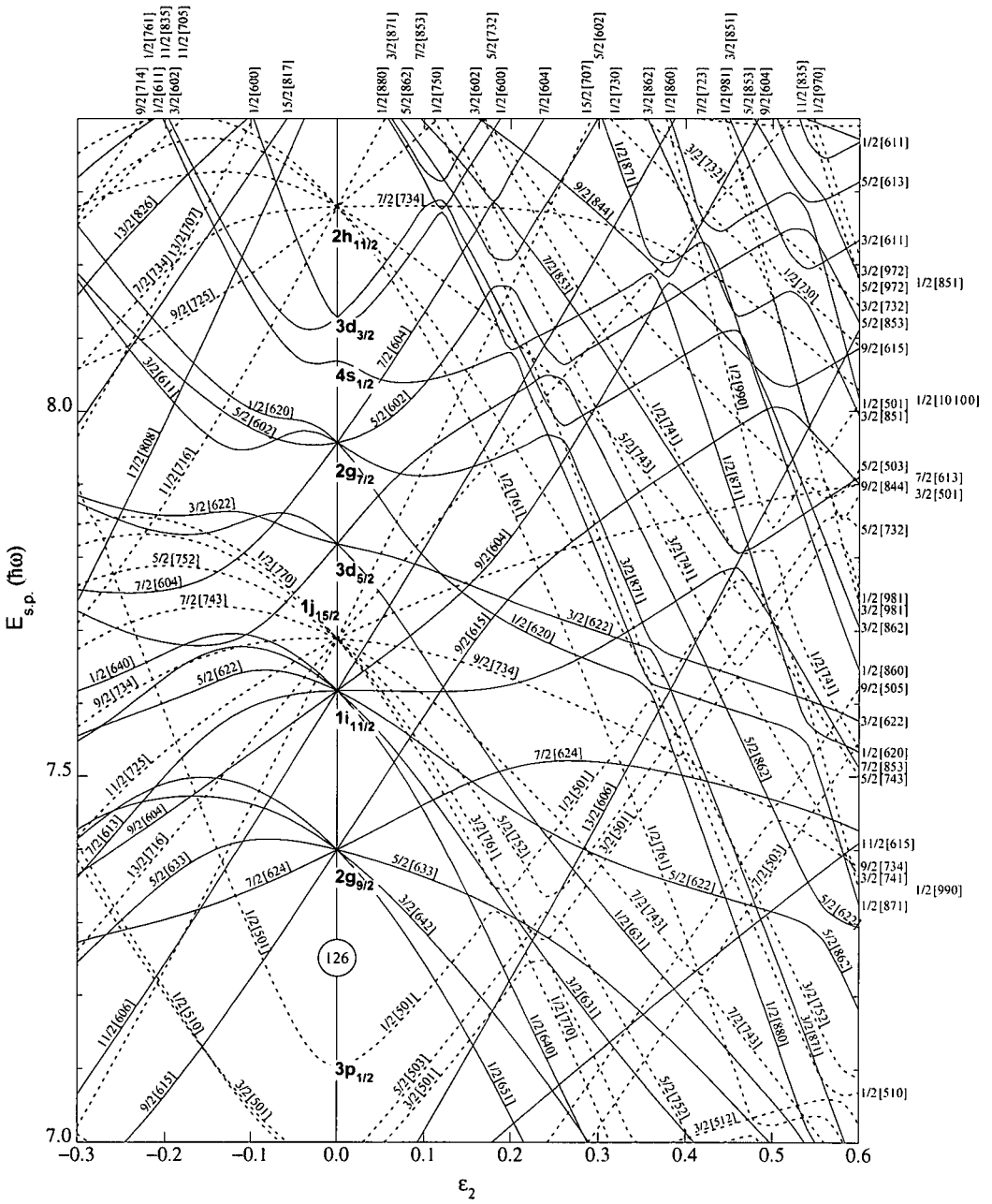

Figure 2.12: The Nilsson states for neutrons $N \geq 126$. Figure taken from reference [Fi96].

of the occupied single particle states. It is clear that a reduction in energy is observed for downsloping orbits with increasing deformation. From this we can deduce that deformed configurations can possess lower energy than in the spherical case.

2.4.2 The cranking model

The cranking model is used to describe the properties of a rotating nucleus, expressing the collective angular momentum as the sum of the single-particle angular momenta. Inglis [In54] provided the first discussion of cranking in 1956 in a semi-classical context. The model considers a collective rotation around an axis (x) perpendicular to the symmetry axis (z) of independent particles moving in an average potential which is rotating with the coordinate frame fixed to that potential. The single-particle cranking Hamiltonian in the rotating frame of the nucleus, rotating with an angular frequency ω around the x axis perpendicular to the symmetry z axis, can be written as

$$h^{\omega} = h - \hbar\omega j_x, \tag{2.34}$$

where h is the intrinsic single particle Hamiltonian (which can be given in the form of a deformed Nilsson or Wood-Saxon potential) and j_x is the total angular momentum projection operator onto the rotation axis. The term -$\hbar\omega j_x$ contains the Coriolis and centrifugal terms which effect the nucleon orbitals. The Coriolis force modifies the single-particle orbits by acting to align the single-particle angular momenta with the rotation axis. Via summation of the individual single particle Hamiltonians one can obtain the total cranking Hamiltonian

$$H^{\omega} = H - \hbar\omega I_x \tag{2.35}$$

where H is the sum of the individual deformed particles and I_x is the projection of the total angular momentum onto the rotational x axis (the aligned angular momentum). The eigenvalues of the Hamiltonian are know as Routhians and a plot of single-particle energy as a function of rotational frequency is known as a Routhian plot.

The presence of the term -$\hbar\omega I_x$ breaks the time-reversal symmetry. The only symmetries which remain are parity and a transformation of 180° defined by the rotation operator. A rotation of 2π, given by $\mathcal{R}_x^2(\pi)$, keeps the wavefunction unchanged for even-A nuclei, but changes sign for odd-A nuclei

$$\mathcal{R}_x^2(\pi)\,\Psi = r^2\Psi = (-1)^A\,\Psi. \tag{2.36}$$

The eigenvalues are $r = \pm 1$ for even-A nuclei and $r = \pm i$ for odd-A nuclei. The signature exponent quantum number α is defined as $r = e^{-i\pi\alpha}$ and the spin sequences are restricted to

$$\begin{aligned}
I = &\quad 0,2,4... && \text{for } \alpha = 0,\ r = +1\\
I = &\quad 1,3,5... && \text{for } \alpha = 1,\ r = \text{-}1\\
I = &\quad \tfrac{1}{2},\tfrac{5}{2},\tfrac{9}{2}... && \text{for } \alpha = \tfrac{1}{2},\ r = \text{-}i\\
I = &\quad \tfrac{3}{2},\tfrac{7}{2},\tfrac{11}{2}... && \text{for } \alpha = \text{-}\tfrac{1}{2},\ r = +i
\end{aligned}$$

which we can simply express as $\alpha = I \bmod 2$. Cranking Routhians are generally labelled by parity and signature (π, α), which are the only good quantum numbers.

Figure 2.13 summarises the corrections made to the spherical shell model which produce a more realsitic nuclear model.

2.4.3 Self-consistent mean-field models

By invoking the variational principle we introduce a tool for the microscopic description of nuclear structure in order to determine a more truthful nuclear potential than that given by the shell model for heavy nuclei. The Hartree-Fock variational approximation (HF) provides self-consistent solutions for calculating the average potential from an effective nucleon interaction.

The single-particle potential is determined by generating self-consistent solutions for which the potential generated by the nucleons, subject to a 2-body interaction, is the same as the potential used to obtain the wavefunctions. There is an underlying

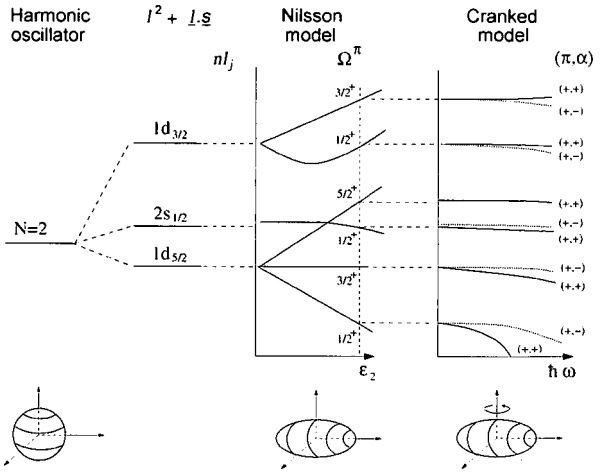

Figure 2.13: Evolution of the energy level spectrum. The single-particle levels are calculated using the shell model for spherical nuclei, the Nilsson model when deformation is introduced and the cranking model when rotation is applied. Figure modified from reference [Pau03].

problem to this procedure, in order to know the single-particle wavefunction, we need to establish the potential that they accommodate but that potential is generated by those actual particle wavefunctions [Ca00]. We are required to solve the procedure by starting from an initial guess for either the wavefunctions or the potential, taking an iterative approach until we reach convergence.

The strength of the effective interaction is determined under a condition that a number of global properties are reproduced. The Skyrme force is used as a phenomenological interaction in HF calculations, replicating binding energies and nuclear radii over the entire nuclear table.

For nuclear properties which are strongly influenced by pairing correlations then the mean-field concept is generalized to include a pairing field, solved by using the Hartree-Fock-Bogoliubov theory. A comprehensive review of self-consistent mean-field models is provided in reference [Be03b] and includes an analysis of several different effective interactions.

2.4.4 The Strutinsky shell correction method

The total energy of the nucleus can be configured by combining a macroscopic and microscopic model. The liquid drop model (LDM) may be used for the calculation of the macroscopic energy contribution, which reproduces the properties of the nucleus that depend in a smooth way on the nucleon number. The microscopic component is formed by the shell model which reproduces the properties in which only the nucleons close to the Fermi surface are involved, but fails to reproduce the bulk properties in which all nucleons contribute.

If we consider a nuclear property, for example binding energy, and we plot the property against the mass number (Figure 2.14) then we observe an oscillatory behaviour which is a reflection of the underlying shell effects. Strutinsky [St67, St68] proposed a method of combining a shell structure with the fundamental bulk properties of the nucleus which can be obtained from the smoothly behaving LDM.

The conception was to begin initially with the smoothly varying LDM element E_{LD} to calculate the nuclear property and then add an oscillatory modification element ΔE_{SH}, caused by the quantum mechanical shell structure, which can be positive or

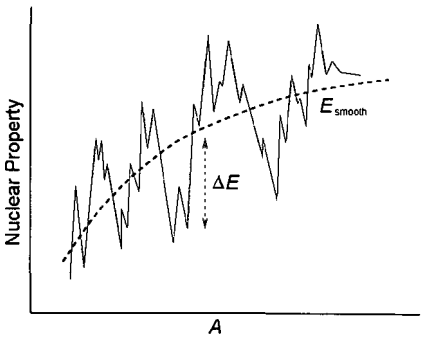

Figure 2.14: A representation of the irregular behaviour of a nuclear property, for example binding energy, as a function of mass. The Strutinsky shell correction terms are indicated. Figure taken from reference [Pau03].

negative,

$$E = E_{LD} + \Delta E_{SH}. \tag{2.37}$$

The shell effects arise in the level density. The LDM generates a constant level density but the shell effects lead to bunching of levels or gaps around the Fermi level. The average level density of which the binding energies corresponding to the shell distribution oscillate around is responsible for the average behaviour of the binding energies and is incorrect in the shell model. Only the fluctuating part ΔE_{SH} of the total energy within the shell model should be considered. It is required to divide up the shell-model energy into an oscillating part ΔE_{SH}, and a smoothly varying part $\tilde{E}_{SH}$,

$$E_{SH} = \sum_{i=1}^{A} \epsilon_{\upsilon_i} = \tilde{E}_{SH} + \Delta E_{SH}, \tag{2.38}$$

where ϵ_{υ_i} represents the nucleon single-particle eigenvalues. Since the fluctuations in the shell-model energy E_{SH} are due to oscillations of the level density then we can calculate the smooth part $\tilde{E}_{SH}$ by introducing a continuous function representing a smooth part of the level density. The total energy of the nucleus may be rewritten

$$E = E_{LD} + \left[E_{SH} - \tilde{E}_{SH}\right] \tag{2.39}$$

where E_{LD} is the macroscopic contribution and $\left[E_{SH} - \tilde{E}_{SH}\right]$ is the macroscopic quantal shell correction term. This model permits the determination of ground state nuclear energies as a function of deformation parameters.

2.5 Nuclear decay modes

In order to investigate the structure of heavy actinides in the region of this study one requires information on the theoretical concepts of the decay mechanisms exhibited, namely α decay, gamma decay and internal conversion. We shall also discuss the experimental determination of the single-particle structure.

2.5.1 Alpha decay

Alpha decay is increasingly evident in the heavy actinide region of this study. The repulsion effect due to the Coulomb force increases with Z^2 whereas the stabilizing effect of the nuclear binding force only increases with A. The emission of an α particle (a ^{4}He nucleus) can be written in the form

$$ {}^{A}_{Z}X_N \rightarrow {}^{A-4}_{Z-2}X'_{N-2} + \alpha. \tag{2.40} $$

By applying conservation of energy and linear momentum to the α emission process, we find that the net energy released in the decay, the Q value, is

$$ Q = (m_X - m_{X'} - m_\alpha) = T_{X'} + T_\alpha. \tag{2.41} $$

By observation of Equation 2.41, we note that Q is also the the total kinetic energy given to the fragments, $T_{X'}$ and T_α, and that the α decay will only occur spontaneously if $Q > 0$. The monoenergetic value of the ground state to ground state α decay aids in the identification of the decaying isotope.

The α particle only carries away orbital angular momentum l_α from an initial nuclear state of angular momentum I_i to a final state I_f within the range $|I_i - I_f| < l_\alpha < I_i + I_f$ and changes parity by $(-1)^{l_\alpha}$.

The α particles emitted can fall into several different decay branches to a number of different states in the daughter nucleus and can therefore posess different decay energies. This is know as fine structure. For even-even nuclei the ground state to ground state decay, i.e. the highest energy, is the most frequent, whereas for non even-even nuclei this is not entirely true. When the initial and final states are of different angular momentum, i.e. the orbital angular momentum of the emitted α particle is non-zero, the decay is hindered by a centrifugal barrier effect.

We assume that the α particle is initially preformed within the parent nucleus prior to a second stage of quantum mechanically tunneling through the Coulomb barrier to complete the decay process. The nuclear structure details of the parent nucleus ground state and the final state within the daughter nucleus dictates the

probability of forming an α particle. The preformation probability may result in a reduction in the α-decay probability. The probability for the formation is related to the reduced α-decay width δ^2 [keV], a measure of the effect that the preformation probability may have on reducing the α-decay probability,

$$\delta^2 = \frac{\lambda h}{P}, \tag{2.42}$$

where λ is the decay constant, h is Planck's constant and P is the barrier penetration factor. The Rasmussen formalism [Ras59] permits the calculation of P.

The decay strengths of the resulting α decay to the ground state or excited states in the daughter nucleus can be compared via a hindrance factor HF, defined by

$$HF = \frac{\delta^2_{g.s}}{\delta^2_{exc.}}, \tag{2.43}$$

where $\delta^2_{g.s.}$ and $\delta^2_{exc.}$ are the reduced α-decay widths of the ground state to ground state and ground state to excited state decays.

2.5.2 Electromagnetic transitions

Gamma decay

When an excited nucleus decays from an initial configuration of spin I_i to a lower energy state or to the ground state of spin I_f, then electromagnetic radiation in the form of a γ ray can be emitted. The energy of the γ ray, E_γ, is characteristic of the energy between the nuclear states, E_γ = E_i - E_f, and is typically within the range of 0.1 to 10 MeV. We neglect the relatively low energy of the nucleus recoil when considering the difference between the two states.

The γ ray is classified according to its electromagnetic character and multipolarity. Electric radiation arises due to an oscillating charge and magnetic radiation arises due to a varying current or magnetic moment. The multipolarity L of the γ ray is the composition of its orbital momentum and its spin, forming the total angular momentum. A set of selection rules for γ-ray transitions between two given nuclear

states arise due to the conservation of angular momentum and parity π, which will determine whether the transition is electric (E) or magnetic (M)

$$|I_i - I_f| \leq L \leq |I_i + I_f| \ \forall \ L \neq 0, \tag{2.44}$$

$$\Delta\pi_{EL} = (-1)^L, \tag{2.45}$$

$$\Delta\pi_{ML} = (-1)^{L+1}. \tag{2.46}$$

From the parity-selection rules we note that even-multipole electric transitions and odd-multipole magnetic transitions have even parity, and odd-multipole electric and even-multipole magnetic transitions have odd parity. If the γ ray carries the maximum difference between the angular momentum of the initial and final states then it is said to be a stretched transition.

We note that a transition in which $L = 0$ cannot occur and that it is possible for a mixed transition of different multipoles to occur.

The total transition probability of the nucleus decay from an initial excited state of spin I_i to a final state I_f may be determined by [Bo98],

$$T_{fi} = \frac{8\pi(L+1)}{\hbar L\left[(2L+1)!!\right]^2}\left(\frac{E_\gamma}{\hbar c}\right)^{2L+1} B(\sigma L, I_i \rightarrow I_f). \tag{2.47}$$

The $B(\sigma L)$ values are the reduced transition probabilities and are given by the reduced matrix elements

$$B(EL, I_i \rightarrow I_f) = \frac{1}{2I_i+1}\left|\left\langle f \left\| \hat{Q} \right\| i \right\rangle\right|^2, \tag{2.48}$$

for the electric case, and

$$B(ML, I_i \rightarrow I_f) = \frac{1}{2I_i+1}\left|\left\langle f \left\| \hat{M} \right\| i \right\rangle\right|^2, \tag{2.49}$$

for the magnetic case, where $\hat{Q}$ and $\hat{M}$ are the electric and magnetic multipole operators.

Weisskopf units (W.u.) can be used to describe lifetimes of nuclear states and they provide an indication of the lifetime range expected for a decay of a fixed multipolarity. The Weisskopf [Wei51] single-particle estimates are based on several assumptions:

Transition probabilities T (s^{-1})	Weisskopf units B_{sp}
T(E1)=1.587·10^{15}·E^3·B(E1)	B_{sp}(E1)=6.446·10^{-2}·$A^{2/3}$
T(E2)=1.223·10^{9}·E^5·B(E2)	B_{sp}(E2)=5.940·10^{-2}·$A^{4/3}$
T(E3)=5.698·10^{2}·E^7·B(E3)	B_{sp}(E3)=5.940·10^{-2}·A^{2}
T(E4)=1.694·10^{-4}·E^9·B(E4)	B_{sp}(E4)=6.285·10^{-2}·$A^{8/3}$
T(M1)=1.779·10^{13}·E^3·B(M1)	B_{sp}(M1)=1.790
T(M2)=1.371·10^{7}·E^5·B(M2)	B_{sp}(M2)=1.650·$A^{2/3}$
T(M3)=6.387·10^{0}·E^7·B(M3)	B_{sp}(M3)=1.650·$A^{4/3}$
T(M4)=1.899·10^{-6}·E^9·B(M4)	B_{sp}(M4)=1.746·A^{2}

Table 2.3: Transition probabilities T (s^{-1}) for single-particle (Weisskopf estimates) transitions expressed by $B(EL)$ ($e^2(\text{fm})^{2L}$) and $B(ML)$ ($\mu_N^2(\text{fm})^{2L-2}$). The energies E are measured in MeV [Ri04].

- the transition of multipolairy L is due to a single proton that changes between two states with total angular momentum $L+\frac{1}{2}$ and $\frac{1}{2}$;
- we take the radial parts of the nuclear wave functions to be constant up to the nuclear radius and zero outside;
- any numerical factors due to angular momentum coupling are set to one.

Table 2.3 provides the expressions for the single-particle estimates for the transition probabilities. The general equations for the single-particle estimates for the reduced probability matrix element are [Ri04]

$$B(EL) = \frac{1.2^{2L}}{4\pi}\left(\frac{3}{L+3}\right)^2 A^{\frac{2L}{3}}\left[e^2(\text{fm})^{2L}\right], \tag{2.50}$$

for the electric transitions and

$$B(ML) = \frac{10}{\pi}(1.2)^{2L-2}\left(\frac{3}{L+3}\right)^2 A^{\frac{2L-2}{3}}\left[\mu_N^2\cdot(\text{fm})^{2L-2}\right], \tag{2.51}$$

for magnetic transitions, where A is the atomic mass number.

Based on the Weisskopf estimates we can draw two conclusions, the lower multipolarities are dominant and that electric radiation is more probable than magnetic radiation.

Internal conversion

Internal conversion is an electromagnetic process that competes with γ emission. The process occurs because the nuclear electromagnetic field may interact with a bound atomic electron giving it sufficient energy to escape the atom. The discrete energy of the ejected electron T_e is equal to the transition energy ΔE, between an excited state and a lower excited state or ground state, minus the electron binding energy B_e,

$$T_e = \Delta E - B_e. \tag{2.52}$$

We witness a set of energies of emitted internal conversion electrons for a given ΔE. The electron binding energy varies with the atomic orbital, a list of these is provided for nobelium in Table 2.4. The electron binding energy in a particular shell sets a threshold energy for the internal conversion process and we may categorize them according to the electron shell from which they originate, i.e. K, L, M, and so forth (corresponding to the principle quantum numbers n = 1, 2, 3,...). From Equation 2.52 we can deduce that the electrons of a particular shell can only be emitted if the transition energy is greater than the binding energy.

The resulting vacancy in one of the electronic shells following the conversion process is filled by electrons from higher shells and, as a consequence of the atomic

K	L_1	L_2	L_3	M_1	M_2	M_3	M_4	M_5
149.2	29.2	28.3	21.9	7.7	7.2	5.7	5.0	4.7

Table 2.4: Atomic electron binding energies B_e for nobelium for the innermost atomic shells (in keV) [Fi96].

arrangement, a characteristic X-ray is emitted. The X-rays observed by the experimentalist allow an identification of the Z of the nucleus under study.

When considering the total decay probability for electromagnetic decay we need to take into account that it is composed of two competing processes, γ-ray emission and internal conversion. We may write this in the form

$$\lambda_t = \lambda_\gamma + \lambda_e \equiv \lambda_\gamma(1 + \alpha), \tag{2.53}$$

where λ_t is the total decay probability, $\lambda_{\gamma,e}$ are the probabilities for γ emission and internal conversion and α is the total internal conversion coefficient, defined as the probability of electron emission relative to γ emission,

$$\alpha = \lambda_e/\lambda_\gamma. \tag{2.54}$$

The coefficient is the sum of all partial conversion coefficients of the different electron orbitals, i.e. $\alpha = \alpha_K + \alpha_{L1} + \alpha_{L2} + \alpha_{L3} + \ldots$. There is an increased probability for internal conversion, and therefore a greater magnitude in the conversion coefficient, for shells close to the nucleus due to the proximity of the nuclear electromagnetic field.

There are a number of features of internal conversion that we can point to and which play an important role in this study. The nucleus under investigation is high Z and we note that conversion coefficients increase as Z^3. The conversion coefficients also decrease with increasing transition energy (we observe a number of low energy transitions in this study). Furthermore, the conversion coefficients increase with the multipole order of the transition and decrease with $1/n^3$ for higher atomic shells [Kr88]. Calculations of conversion coefficients for this study are performed using the software BRICC [ICC].

Comparison of the theoretical values of the conversion coefficient with values obtained from the experimental ratios of conversion electrons and γ-ray emission intensities provide an indication of the multipolarity of the transition.

Magnetic dipole moment

Measurement of the magnetic dipole moment allows one to obtain an experimental distinction between proton and neutron single-particle states. The magnetic dipole moment μ is produced by the orbital motion of the protons and the intrinsic spins of all nucleons. The moment provides a gauge of the current distribution in a nucleus. The magnetic dipole moment operator can be calculated by summing over all the nucleons

$$\underline{\mu} = \mu_N \sum_{1}^{A} \left(g_{l_i} \underline{l_i} + g_{s_i} \underline{s_i} \right), \tag{2.55}$$

where μ_N is the nuclear magneton ($= e\hbar/2m_N$) and g_l and g_s are the orbital and spin angular momentum g-factors for free nucleons:

proton:	$g_l = 1,$	$g_s = 5.5856$
neutron:	$g_l = 0,$	$g_s =$ -3.8262

If we assume that the protons are evenly distributed throughout a rotating nucleus with core angular momentum $\underline{R}$, then we can estimate a core contribution to the magnetic moment via

$$\underline{\mu} = g_R \underline{R} \mu_N \quad \text{with} \quad g_R \approx Z/A, \tag{2.56}$$

where g_R is the rotational g-factor describing the collective rotation. Figure 2.15 displays a reduction of g_R below Z/A for the first excited 2^+ states in even-even nuclei. This is certainly evident for nuclei which exhibit rotational behaviour. Expression 2.56 holds for even-even nuclei with no intrinsic excitation. For $K > 1/2$ we introduce a single-particle g-factor denoted by g_K. The total angular momentum is now $\underline{R} = \underline{I} + \underline{j}$ and the magnitude of the magnetic dipole moment can be expressed as

$$\mu = g_R I + (g_K - g_R) \left[K^2 / (I+1) \right]. \tag{2.57}$$

A deduction of $(g_K - g_R)$ allows for a measurement of the strength of the in-band *B(M1)* decays (the reduced M1 transition rate) which depend on the single-particle

structure of the odd-particle (units $\mu_N{}^2$),

$$B(M1; I \rightarrow I-1) = \frac{3}{4\pi}\left(g_K - g_R\right)^2 K^2 \frac{(I-K)(I+K)}{I(2I+1)}. \tag{2.58}$$

Electric quadrupole moment

The electric quadrupole moment Q_0 is a measure of the deviation of charge distribution from spherical symmetry of the nucleus. The electric quadrupole operator is expressed in terms of the charge density $\rho(r)$,

$$eQ(\underline{r}) = \int \rho(\underline{r})\left(3\cos^2\theta - 1\right) dV, \tag{2.59}$$

where θ is the angle subtended by the radius vector $\underline{r}$. If the nucleus is spherical then the integral over the nuclear volume will be zero. Positive quadrupole moments are characteristic of prolate deformed shapes and may be calculated in terms of the deformation parameter β,

$$Q_0 = \frac{3}{\sqrt{5\pi}} R_{av}^2 Z\beta\left(1 + 0.16\beta\right), \tag{2.60}$$

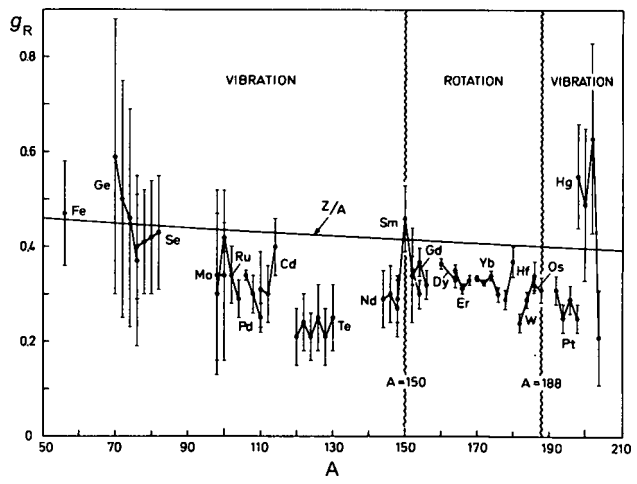

Figure 2.15: Values of the rotational g-factor for the first excited 2^+ states in even-even nuclei. Figure taken from [Bo98].

where Q_0 is known as the intrinsic quadrupole moment and $R_{av} = R_0 A^{1/3}$.

In the rotational model, the measurement of the intrinsic quadrupole moment allows for a calculation of the reduced E2 transition rate (units e^2b^2)

$$B(E2; I \rightarrow I-2) = \frac{5}{16\pi} Q_0^2 \frac{3(I-K)(I-K-1)(I+K)(I+K-1)}{(2I-2)(2I-1)I(2I+1)}, \quad (2.61)$$

and for an unstretched transition

$$B(E2; I \rightarrow I-1) = \frac{5}{16\pi} Q_0^2 \frac{3K^2(I-K)(I+K)}{(I-1)I(2I+1)(I+1)}. \quad (2.62)$$

Further to this, the experimental $\frac{B(M1)}{B(E2)}$ ratio, in units of $[\mu_N^2/e^2b^2]$ can now be calculated using the expression

$$\frac{B(M1; I \rightarrow I-1)}{B(E2; I \rightarrow I-2)} = \frac{8}{5} \frac{[g_K - g_R]^2 K^2}{Q_0^2} \frac{(2I-1)(I-1)}{(I-1+K)(I-1-K)}. \quad (2.63)$$

By comparing the experimentally observed $\frac{B(M1)}{B(E2)}$ values with those produced theoretically, a specific assignment of a multi-quasiparticle state can be made.

Branching ratios and *g*-factors

Experimentally it is difficult to obtain absolute *B(M1)* and *B(E2)* values through measurements of the mean lifetimes of nuclear states. The intrinsic structure of a rotational band can be inferred by measuring the intensity of the $\Delta I = 1$ and $\Delta I = 2$ branches and their energies [Rag95]

$$\frac{\delta^2}{1+\delta^2} = \frac{2K^2(2I-1)}{(I+1)(I-1+K)(I-1-K)} \left(\frac{E_1}{E_2}\right)^5 \frac{I_\gamma(\Delta I = 2)}{I_\gamma(\Delta I = 1)} \quad (2.64)$$

where δ is the E2/M1 mixing ratio, E_1 and E_2 are the dipole and quadrupole transition energies and I_γ are the relative γ-ray intensities.

The g_K value can be approximated using the expression

$$\frac{|g_K - g_R|}{Q_0} = \frac{0.93 E_1}{\delta\sqrt{I^2-1}}. \quad (2.65)$$

But we note that Equation 2.65 only gives the magnitude of the value g_K - g_R. Therefore, two different branching ratios will be consistent with the experimentally measured values making it difficult to distinguish between different configurations.

An effective g-factor of two unlike particles (g_1, j_1) and (g_2, j_2) can be obtained by combining the individual g-factors

$$g_J = \frac{g_1 + g_2}{2} + \frac{g_1 - g_2}{2}\left[\frac{j_1(j_1+1) - j_2(j_2+1)}{J(J+1)}\right], \tag{2.66}$$

where $J = j_1 + j_2$.

2.6 High-K states and isomers

Isomers are nuclei in highly excited metastable states with inhibited electromagnetic decay which have a lifetime longer than states which decay promptly, approximately 1 ns, although there is no set criterion for classification. Isomer half-lives can be remarkably long since isomer de-excitation depends on spontaneous emission. In addition, excitation energies of the isomeric states may reach several MeV. For example the spin state $16\hbar$ in ^{178}Hf has a half-life of 31 years and an excitation energy of 2.4 MeV.

Isomeric states arise due to a secondary energy minimum for nuclear variables of shape elongation, spin or the projection of the total spin along the symmetry axis of the nucleus. Figure 2.16 illustrates the different ways in which isomers are formed [Wa99].

Shape isomers originate in a secondary energy minimum at a point of large elongation of the nucleus, where the initial energy minimum corresponds to the ground state. Decay modes include both fission and γ-ray emission.

Spin-trap isomers arise when the decay to a lower energy state requires a large change in spin. Hence the emission of radiation with high multipolarity is necessary to meet the demand in change in spin. Equations 2.50 and 2.51 indicate that transitions with high multipolarity are less probable and this leads to the extended lifetimes of these states.

The K-trap isomer is a variation of the spin trap isomer, where the orientation of the spin vector, and not exclusively the magnitude, acts to produce the isomeric state. The value of K is not a directly measured quantity, but it is widely assumed to

be equal to the total angular momentum of the isomer. We expect to find K isomers in regions where high-K orbitals are at the Fermi surface, the orbitals couple together to give energetically favoured states with high K.

For the analysis detailed in this study we are concerned with the latter isomer K traps, which arise only in axially symmetric, deformed nuclei well away from the closed shells that favour spherical shapes.

The K-selection rule for γ emission is that for K to remain a good quantum number

$$L \geq |\Delta K|\,, \tag{2.67}$$

where ΔK is the change in K between the initial and final states and L is the multpolarity of the transition.

Empirical observations show that K-forbidden transitions are permitted, and a measure of their forbiddenness ν is derived via

$$\nu = |\Delta K| - L. \tag{2.68}$$

For example, there is a $K = 8$ isomer in ^{180}Hf at 1.1 MeV which decays via a $\lambda = 1$ transition to a $K = 0$ state, so that $\Delta K = 8$. These transitions are hindered, rather than forbidden. A reduced hindrance factor can be calculated using

$$f_\nu = F_W^{1/\nu} = [(T_{1/2})_{exp}/(T_{1/2})_{WU}]^{1/\nu}, \tag{2.69}$$

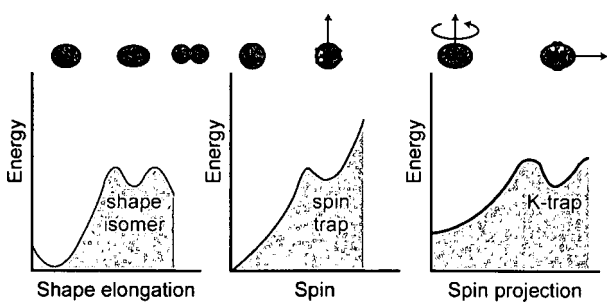

Figure 2.16: An illustration of the secondary energy minima observed for several nuclear variables responsible for the different isomers. Figure taken from [Wa99].

where F_W is the Weisskopf hindrance factor, $(T_{1/2})_{exp}$ is the partial γ-ray half-life and $(T_{1/2})_{WU}$ is a theoretical single-particle Weisskopf estimate. The reduced-hindrance value is used for a systematic comparison of isomeric states. General behaviour noted by Löbner [Lö68] pointed at the Weisskopf hindrance factor decreasing approximately by a factor of one hundred per degree of K-forbiddenness. This was in agreement with a rule proposed by Rusinov [Ru61],

$$\log F_W = 2\left(|\Delta K| - L\right). \tag{2.70}$$

However, it was found experimentally that values of F_W are larger than those provided by Rusinov's rule for most multipole transitions.

Chapter 3

Experimental Techniques

This chapter details the process of fusion evaporation reactions used in the production of transfermium elements. The beam of ions used as the projectiles in the reaction are produced via an electron cyclotron resonance (ECR) ion source and their acceleration is performed by the K130 cyclotron at the Accelerator Laboratory of the University of Jyväskylä (JYFL). The experimental setup at JYFL will be discussed and a brief overview will be given of the experimental setup utilised at the Gesellschaft für Schwerionenforschung (GSI), namely the separator and detectors, from which extra statistics have been exploited in order to further our study.

3.1 Production of heavy elements

The production of elements in the region of $Z \approx 102$ is challenging as one has to overcome the strong competition from fission and also the drawbacks of low reaction cross sections. Production via heavy ion induced fusion evaporation reactions is the preferred method of production of transfermium elements and in the $Z \approx 102$ region reactions have been performed with moderate cross sections, producing nuclei with a high degree of angular momentum and excitation energy.

3.1.1 Heavy-ion fusion evaporation reactions and the decay of the compound nucleus

The nuclei produced in this study were created via heavy-ion fusion evaporation reactions. This form of reaction constitutes a projectile nucleus (a beam of ions) which is incident on a stationary target nucleus. This process and subsequent decay can be written in the form

$$(A_p, Z_p) + (A_t, Z_t) \rightarrow (A_c, Z_c)^* \rightarrow (A_{er}, Z_{er}) + EP + \gamma\text{-rays}, \tag{3.1}$$

where the subscripts p, t, c and er on the mass number, A, and proton number, Z, of the nucleus denote the projectile, target, compound nucleus, and evaporation residue. We shall discuss the formation of the compound nucleus and also its decay to the ground state, where evaporation particles, EP, and γ-rays are emitted.

Fusion of the projectile and target to form a compound nucleus depends upon two conditions being satisfied. The first condition is that the incident projectile must possess enough energy to overcome the Coulomb barrier between the projectile and the target nucleus. The Coulomb barrier, assuming spherical nuclei, can be written in the form [Ho78]

$$E_{CB} \approx \frac{Z_p Z_t e^2}{A_p^{1/3} + A_t^{1/3}} [\text{MeV}]. \tag{3.2}$$

The excitation energy, E^*, of the compound nucleus can be expressed in terms of a centre-of-mass bombarding energy, E_{CM} and a Q-value for the compound nucleus formation

$$E^* = E_{CM} + Q. \tag{3.3}$$

This shows that the compound nucleus formation represents the limit of a completely inelastic process, where all of the relative kinetic energy in the incident channel is absorbed [Ba80].

The second condition which must be met regards the impact parameter of the reaction. If the centrifugal forces, caused by the rapid rotation of the compound

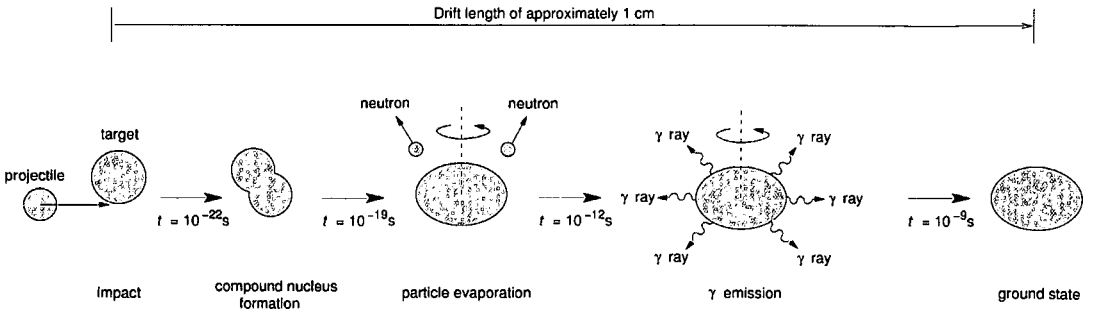

Figure 3.1: Illustration depicting the formation of the compound nucleus and the subsequent decay to the ground state. Figure modified from reference [Pa05].

nucleus, are not to overcome the attraction of the nuclear force than the compound nucleus must be formed with adequately low angular momentum [Ho78].

Fission dominates for heavy nuclei but if the above mentioned criteria are met and the compound nucleus is formed then the decay to a quiescent state is executed through several processes [Ba80, Ca00, Ho78], illustrated in Figures 3.1 and 3.2. Initially, at the point of formation, we can think of the compound nucleus in terms of an analogy with the evaporation of molecules from a liquid. The kinetic energy shared amongst the constituent nucleons in the newly formed compound nucleus is not enough for them to break free from the nucleus. However, collisions between the nucleons may occassionally converge enough energy to a single neutron or proton allowing it to escape. In this study, these evaporation particles are predominantly neutrons since the decay of charged particles is suppressed due to the high Coulomb barrier of the high-Z compound nucleus. At each point of neutron evaporation, approximately 6-8 MeV of excitation energy is removed from the compound nucleus as it decays from a highly excited state at an initial energy of approximately 40 MeV. The angular momentum removed from the system in this region of de-excitation is low due to the small mass of the neutron.

Neutron emission is strongly inhibited when the excitation energy above the yrast

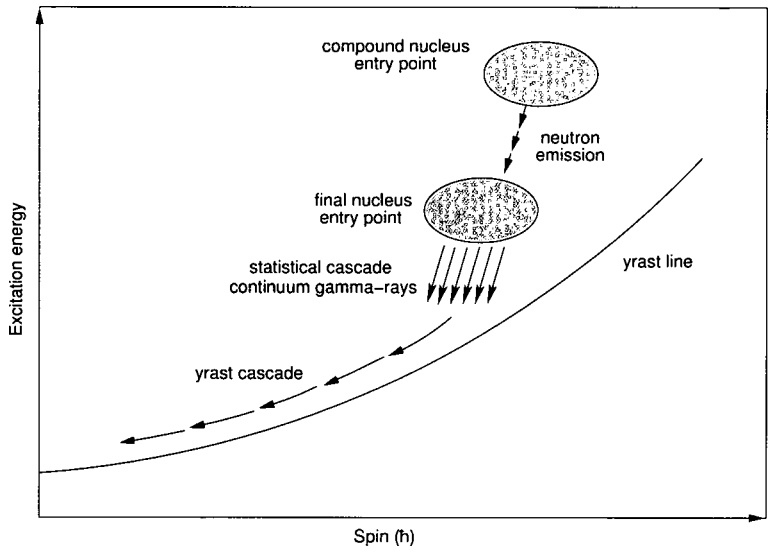

Figure 3.2: Schematic representation of the de-excitation mechanisms in heavy-ion reactions [Ca00].

line is approximately equal to or less than the neutron separation energy, at this point gamma emission is adopted. De-excitation by a cascade of statistical dipole (E1) γ-rays removes large amounts of energy but little angular momentum. These γ-rays cannot be resolved because of the high level density.

Within 2-3 MeV of the yrast line the nucleus reaches its final stage of cooling which is completed by the emission of E2 γ-ray transitions. The discrete transitions decrease the rotation of the nucleus, removing large amounts of angular momentum. Spectroscopic studies are conducted on these transitions which reveal properties of the structure of the nucleus.

The projectile, ^{48}Ca, and target, ^{208}Pb, used in this study are both doubly magic. This leads to a favourable reaction Q-value. Hence the compound nucleus can be formed with lower excitation energy and therefore decreasing the probability of fission.

Figure 3.3 shows the production cross sections recorded for the $1n$, $2n$ and $3n$ channels for the ^{48}Ca + ^{208}Pb reaction. Two characteristics hold for the total evaporation channel cross section. The decreasing Coulomb barrier penetrability terminates the

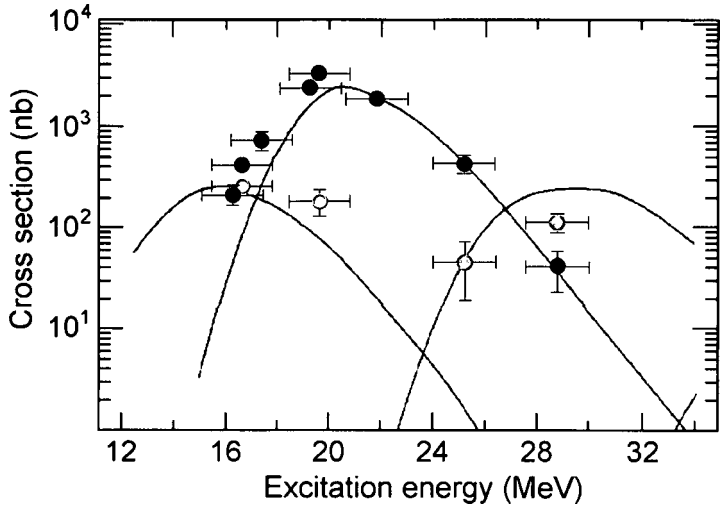

Figure 3.3: Evaporation residue cross-sections for the $1n$ (white circles), $2n$ (black circles) and $3n$ (grey circles) channels for the reaction ^{48}Ca + ^{208}Pb. The solid lines show a prediction made by the evaporation code HIVAP. Figure modified from reference [Gä89].

excitation function at low energy and the probability of fission causes the excitation function to diminish gradually at higher energy.

3.2 Geometry of setup at JYFL

Figure 3.4 shows a schematic representation of the experimental setup at JYFL. Following the formation and acceleration of the beam, the bombardment of the target occurs at the central position of the JUROGAM array. The subsequent recoils are preferentially selected from the primary beam-like products following the fusion evaporation reaction using the RITU gas-filled separator. After which the implanted recoils and emitted radiation are detected at the focal plane via GREAT. All of the individual components are discussed in detail in the following sections.

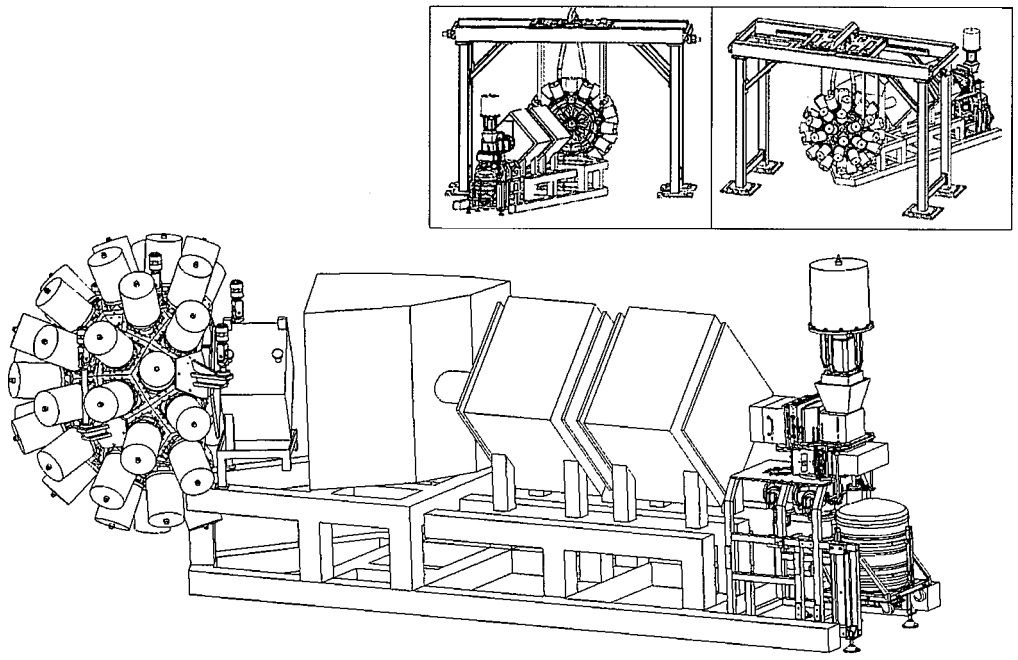

Figure 3.4: Schematic drawing of the experimental setup at JYFL. From left to right, the JUROGAM array, the RITU gas-filled recoil separator and the GREAT focal plane spectrometer. The $K130$ cyclotron beam line arrives from the left-hand side. The insets show the implantation detectors at the front (right) and the target position at the front (left) with the supporting structure of JUROGAM illustrated [Se07].

3.3 The JUROGAM array

Large germanium detector arrays were constructed to study nuclear structure at high angular momentum. The high energy resolution and efficiency within a wide energy range presented by the arrays improved measurements of the γ ray cascades produced in the decay of high spin states.

The details of the operation of semiconductor germanium detectors and the interactions of γ rays within such devices are not discussed in this work, but are explained in detail in reference [Kn00]. However, it is important to note that a major problem occurs within the energy range of this study. Multiple Compton scattering of the incident radiation will lead to a large background component. Compton suppression is one of the main principles required for γ-ray detection in the energy range 100 keV - 1.5 MeV. To overcome this problem a bismuth-germanate Compton-suppression shield surrounding the germanium detector suppresses the background arising from Compton-scattered events [No94].

The JUROGAM detector array, commissioned in 2003, is used to detect prompt γ rays at the target area in in-beam spectroscopy experiments. The array consists of 43 EUROGAM Phase-I type Compton-suppressed germanium detectors, provided from the GAMMAPOOL of resources from the former EUROBALL, and includes detectors from the UK-France Loan Pool. Each detector module, consisting of a high purity Ge detector and a Compton-suppression shield is mounted in a honeycomb geometry in an attempt to provide the best solid-angle coverage. Twelve regular pentagons form a dodecahedron shell around the target position of which each is divided into six sections to hold a detector into position. Unfortunately, the recoil separator RITU restricts full use of the accommodation made available in the surrounding framework. The framework can be split into two hemispheres, perpendicular to the beam axis, thus removing JUROGAM from the experiment, to allow the use of high intensity beams for decay spectroscopy measurements at the focal plane. The angular specifications of the array are given in Table 3.1.

The JUROGAM array has a recorded absolute total photopeak efficiency of 4 %

Array position	$\theta°$	$\phi°$
1 - 5	157.6	0, 72, 144, 216, 288
6 - 15	133.57	18, 54, 90, 126, 162, 198, 234, 270, 306, 342
16 - 25	107.94	13.6, 58.6, 85.6, 130.4, 157.6, 202.4, 229.4, 274.4, 304, 344
26 - 30	94.16	36, 108, 180, 252, 324
31 - 35	85.84	0, 72, 144, 216, 288
36 - 39, 42 - 45	72.05	22.4, 49.9, 94.4, 121.6, 238.1, 265.6, 310.4, 337.6

Table 3.1: Table showing the JUROGAM array specification. Angles $\theta°$ are defined with respect to the beam direction, $\phi = 0°$ is defined as vertically upwards, ϕ increases in a clockwise direction when the array is viewed from a position upstream [JYU].

at 1.3 MeV for γ-rays [JYU]. An absolute efficiency curve for the array, measured during an experiment conducted in April 2006, from which data is used in this study, is shown in Figure 3.5. The eficiency data was compiled using sources of ^{152}Eu and ^{133}Ba which were placed at the target position and data was collected for a known period of time. Using this data the absolute efficiency of the JUROGAM array is measured to be 3.66 % at 1.3 MeV. The difference between the aforementioned 4 % value and the calculated value is due to detectors being switched off during the experimental run. For the experiment conducted in May 2007, from which data is also analysed in this study, the absolute efficiency of the JUROGAM array is measured to be 3.76 % at 1.3 MeV. The curve was fitted to the data using the formula [Rad95]

$$eff = F \exp\left[(A + Bx)^{-E} + (C + Dx)^{-E}\right]^{\frac{-1}{E}}, \tag{3.4}$$

where $x = \ln(E_\gamma)$ and the γ-ray energy is in keV. The coefficients and their errors used for experiments April 2006 and May 2007 are presented in Tables 3.2 and 3.3.

A = -2.97 *800*	B = 1.71 *20*	C = 8.55 *800*
D = -0.543 *20*	E = 11.01 *1600*	F = 0.00035 *300*

Table 3.2: Table showing the coefficients used for the JUROGAM absolute efficiency calculation for the April 2006 experiment. The errors on the coefficients were applied to the correction of recorded transition intensities.

A = -9.51 *700*	B = 3.18 *150*	C = 8.86 *100*
D = -0.607 *60*	E = 4.24 *650*	F = 0.00042 *400*

Table 3.3: Table showing the coefficients used for the JUROGAM absolute efficiency calculation for the May 2007 experiment. The errors on the coefficients were applied to the correction of recorded transition intensities.

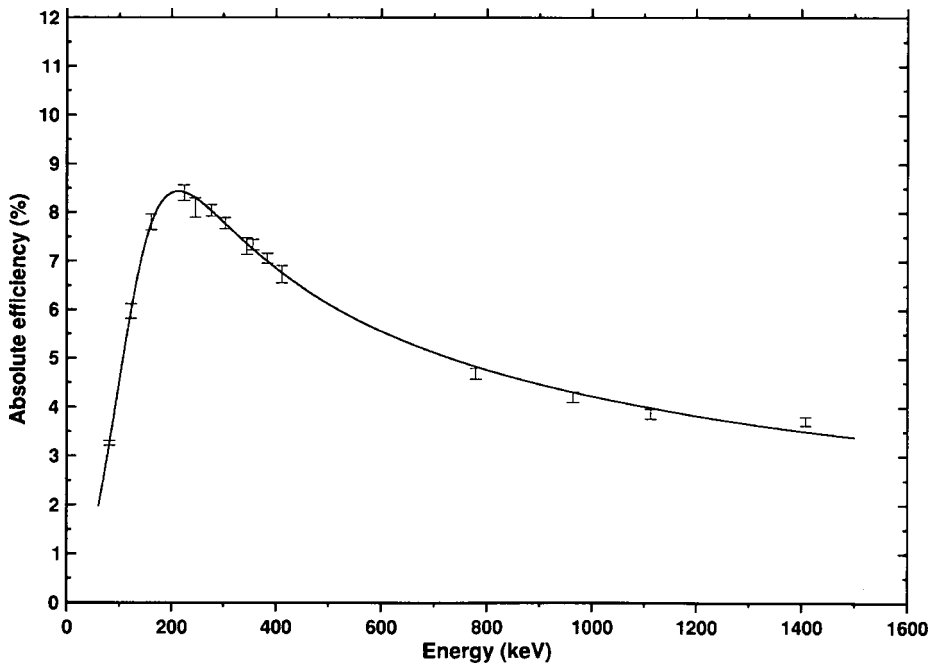

Figure 3.5: The absolute photopeak efficiency of the JUROGAM array for the April 2006 experiment.

3.4 Recoil separator

Recoil separators are used to separate in-flight evaporation residues in heavy-ion induced fusion reactions. Production cross-sections can be low and so therefore effective separation is crucial. We may arrive at the separation of charged particles by a variety of means, including mass, charge, momentum and energy, or any combination thereof, with electric and magnetic fields. There is a variety of recoil separators in operation which perform according to different properties. The Recoil Ion Transport Unit (RITU) at JYFL and the Separator for Heavy Ion reaction Products (SHIP) at GSI were used in the acquisition of data presented here and will be discussed.

Let us consider how the applied fields act to separate the evaporation residues. The Lorentz force is the force acting on moving charged particles in the presence of a magnetic field B and an electric field E. In the case of an applied magnetic field, the Lorentz force can be written as

$$\underline{F}_{mag} = q \cdot (\underline{v} \times \underline{B}) . \tag{3.5}$$

To calculate the distance the radius of curvature we note that $F_{mag} = F_{centr}$ and that the Lorentz force provides the centripetal acceleration necessary to maintain the circular orbit. Thus

$$R = \frac{mv}{qB} = \frac{p}{qB}, \tag{3.6}$$

implying that a magnetic field separates the evaporation residues according to their momentum-to-charge ratio.

A combination of a magnetic and electric fields can be used to focus the evaporation residues. The electric force acting on a charged particle in an electric field is given by

$$\underline{F}_{elec} = q \cdot \underline{E}. \tag{3.7}$$

If we consider Figure 3.6 then the relationship between the velocity in the x and y directions is

$$\tan \vartheta = v_y / v_x. \tag{3.8}$$

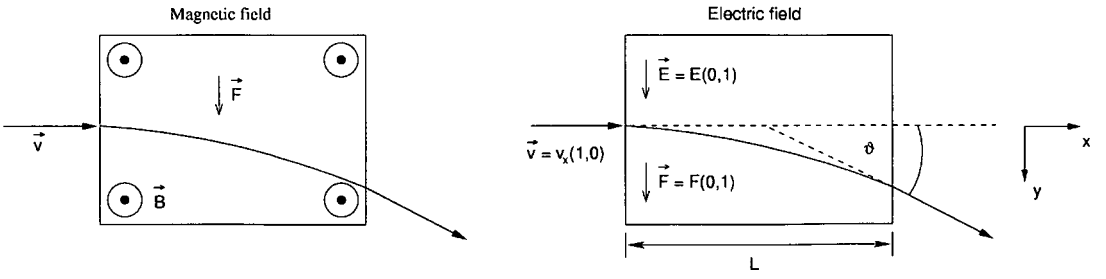

Figure 3.6: Figures showing how the applied magnetic and electric fields within a recoil separator act to separate the evaporation residues. Figure modified from reference [He07].

The velocity in the y frame can be calculated using the second law of motion

$$v_y = a_y t = qE/m \cdot L/v_x, \tag{3.9}$$

and therefore

$$\tan\vartheta = \frac{qEL}{mv_x^2}, \tag{3.10}$$

implying that the electric field separates the evaporation residues according to their energy-to-charge ratio.

When we combine the two fields

$$\underline{F}_{tot} = q\left(\underline{E} + \underline{v} \times \underline{B}\right), \tag{3.11}$$

and fulfill the relationship $E = -v_0 B$, we conclude that

$$F_{tot} = 0 \text{ for } v = v_0 \text{ and } F_{tot} \neq 0 \text{ for } v \neq v_0, \tag{3.12}$$

indicating an independence of q and a filtration according to velocity, which is the fundamental principle of the velocity filter, SHIP [Mü79].

For highly asymmetric reactions gas-filled separators work well. The concept of a gas-filled separator was proposed by Cohen and Fulmer [Co58]. As the heavy ions pass through a dilute gas, collisions occur with the gas molecules leading to charge exchanges and a continuous change of the electronic charge state of the ion.

If we consider 1 metre of travel of a moderately energetic heavy ion in a gas of low pressure (1 mbar) then its electronic charge state is changed 100-1000 times in atomic collisions [Le97]. The resulting average charge state, q_{ave}, then defines the trajectory at which the ions follow in a magnetic field [Gh88]:

$$B\rho = \frac{p}{q_{ave}} = \frac{p}{(v/v_B)\,eZ^{1/3}} = \frac{0.0227A}{Z^{1/3}}Tm, \tag{3.13}$$

where $B\rho$ is the magnetic rigidity of the ions, composed of B, the magnetic flux density and ρ, the radius of curvature, and p is the momentum of the ion. The average charge state of the gas can be expressed in terms of the Thomas-Fermi model of the atom, $q_{ave} = (v/v_B)\,eZ^{1/3}$, since we use the assumption that all orbital electrons whose velocities are less than the ion's velocities are stripped. The Bohr velocity is given by $v_B = (1/137)c$ ms^{-1} and Z and A are the atomic number and mass of the recoiling ion [Bo40, Lam40]. From Equation 3.13 we draw the conclusion that the magnetic rigidity is independent of the initial charge-state and velocity distribution of the ions and that a gas-filled separator essentially act as a mass separator [Le95]. In principle, all charge states and velocity distributions are collected leading to a high transmission efficiency (this concept is illustrated in Figure 3.7). However, the efficiency is hindered by the scattering of the recoils within the gas which reduces the mass resolving power [Gh88]. Gas pressures of the order of 1 mbar are desirable to focus the recoils on the focal-plane detector.

3.4.1 The RITU gas-filled recoil separator

We have shown that according to equation 3.13 that RITU is essentially a mass separator. The ion optical configuration of RITU is of the form ($Q_vDQ_hQ_v$) where the initial vertically focusing quadrupole magnet (Q_v) was introduced to improve accordance with the acceptance of the dipole magnet (D). This configuration has a 30% higher angular acceptance than that of the basic separator type of (DQQ) design. The dipole magnet is the dispersive element of the setup and the latter quadrupole douplet (Q_hQ_v) acts to focus the fusion products into the focal plane detectors [Le97].

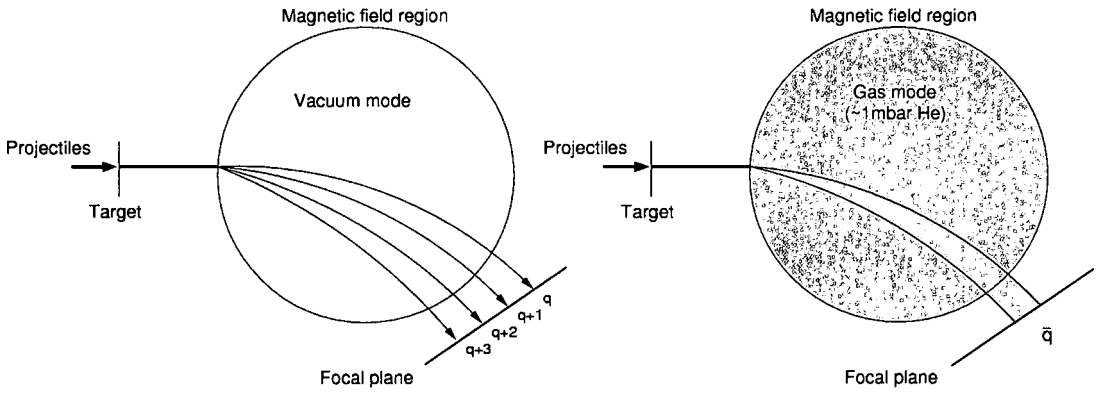

Figure 3.7: An illustration of the contrast of the separation of recoils in a magnetic separator in vacuum mode (left) and gas-filled mode (right). The radial dispersion in the vacuum mode is greater as the individual charge states following their own trajectory before arriving at the focal plane.

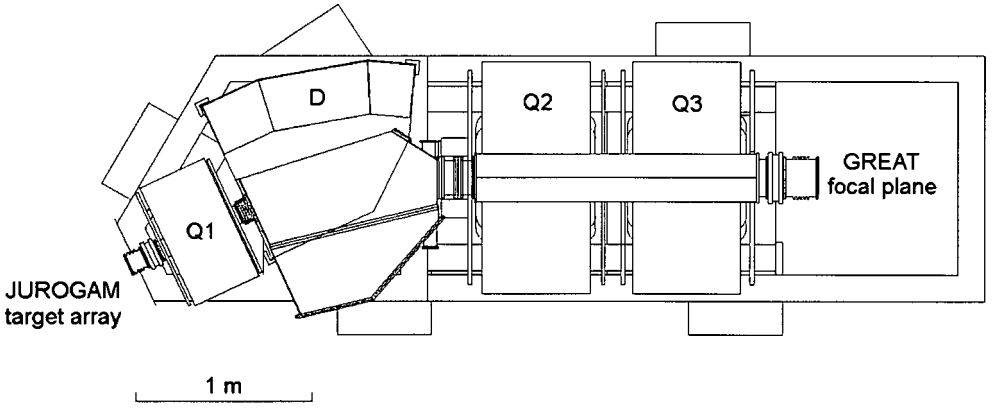

Figure 3.8: Schematic diagram of the RITU separator. Modifications to the dipole chamber where a beam dump acts to collect unreacted and scattered primary beam particles are shown [Gr04].

The separator RITU is shown shematically in Figure 3.8.

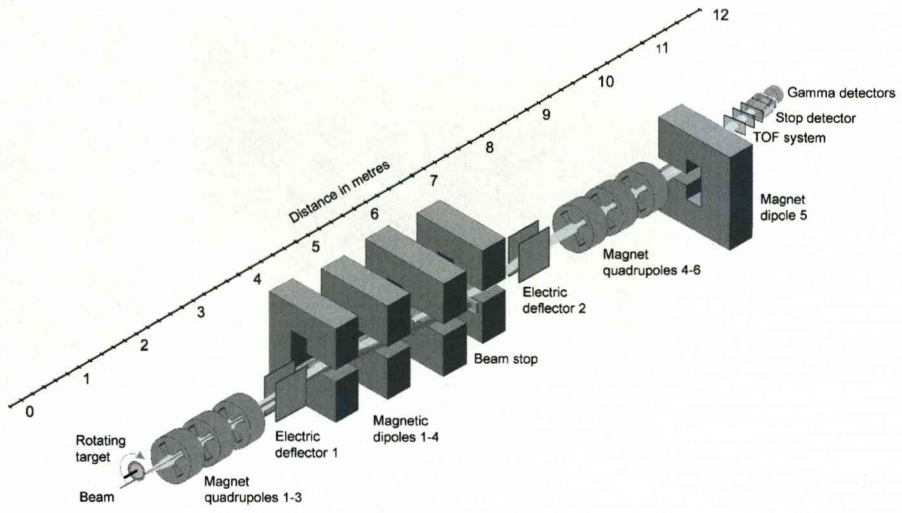

Figure 3.9: Schematic diagram of the SHIP velocity filter. Focal plane detectors at the top right-hand side of the diagram are labelled.

3.4.2 The SHIP velocity filter

The SHIP velocity filter at GSI follows the principle of Statement 3.12 and filters according to the specific kinematics properties of the fusion products. SHIP has separated electric field and magnetic fields, unlike the standard Wien-filters, and a configuration of the the form (QQQEDDDDEQQQ) where (E) is an electric deflector. An additional 7.5° deflection magnet is positioned behind SHIP to produce a significant reduction to the background [Ho00]. The separator SHIP is shown schematically in Figure 3.9.

3.5 The GREAT focal plane spectrometer

The Gamma Recoil Electron Alpha Tagging (GREAT) spectrometer is positioned at the focal plane of the RITU separator where the evaporation residues are implanted

and the subsequent delayed radiation is detected. The GREAT spectrometer was commissioned in 2002 and is a collection of silicon, germanium and gas detectors used for decay measurements at the focal plane or for use as a tagging spectrometer for measuring prompt decays at the target position. The individual components are discussed in detail in reference [Pa03]. Figures 3.10 and 3.11 present the constituent elements of the spectrometer, outlined in the following pages, which are used to detect protons, α particles, β particles, γ rays or conversion electrons with high efficiency.

3.5.1 The multi-wire proportional counter

The Multi-Wire Proportional Counter (MWPC) acts as an active recoil discriminator at the entrance of GREAT. Mylar foils partition the isobutane gas within the MWPC from the helium gas within RITU at the entrance window and from the vacuum of GREAT at the exit window. The MWPC has two functions to perform, the first entails a coincidence/anticoincidence technique whereby the recoils which pass through the counter generate a signal before they arrive at the implantation detector. The subsequent radioactive decay within the implantation detector from the recoiling ion will not generate a signal within the counter and thus we are able to discriminate between the two. Secondly, the energy-loss and timing signals obtained from the counter allow the experimentalist to differentiate between the fusion reaction products and the scattered beam particles.

3.5.2 The double-sided silicon strip detector

Energies of the implanted recoiling ions are measured in two adjacent Double-Sided Silicon Strip Detectors (DSSSD). The characteristics of the DSSSD ensure excellent position sensitivity to measure the decay particles of the implanted recoiling ions. A single Si strip detector measures 60 mm $\times$ 40 mm with a strip pitch of 1 mm in both the x and y directions, thus constructing 4800 pixels. The recoil-detection efficiency is estimated at approximately 85 %. The DSSSD has a thickness of 300 μm, easily accommodating typical recoil implantation products at a depth of approximately 1 -

10 μm, but it is possible for a percentage of the α-particles to escape the detector.

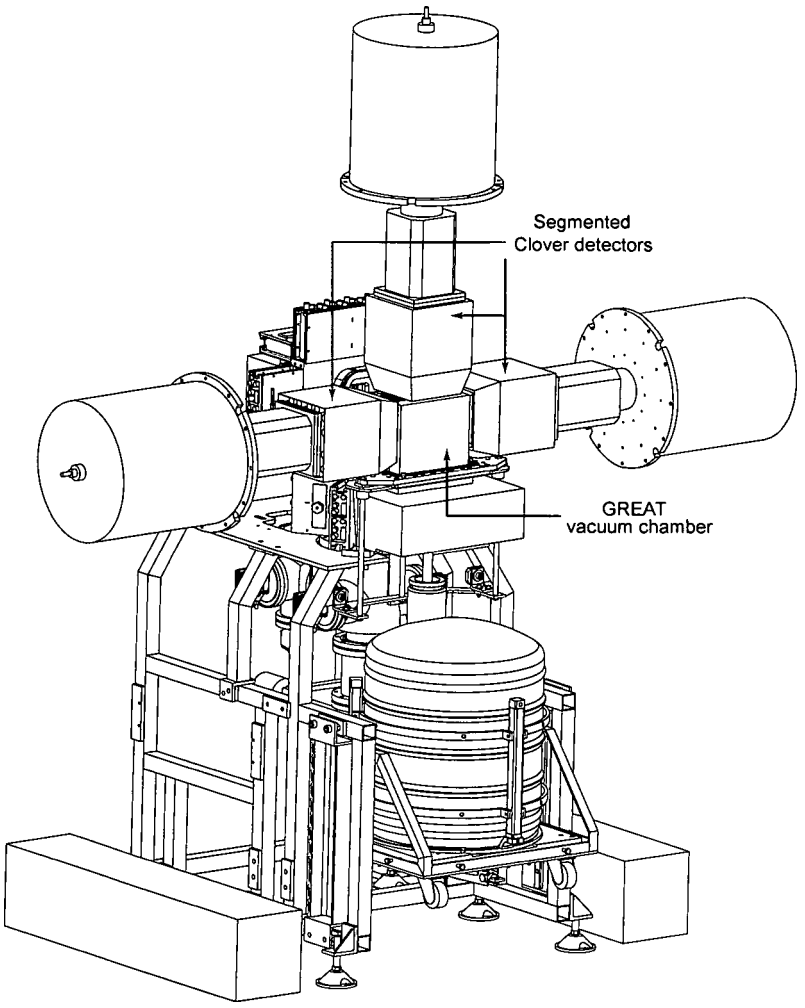

Figure 3.10: Diagram of the GREAT focal plane spectrometer [Se07]. Three segmented clover detectors surround the vacuum chamber in which a box of 28 silicon PIN photodiode detectors, 2 double-sided Si strip detectors and a planar germanium detector are installed. The recoils enter from the left.

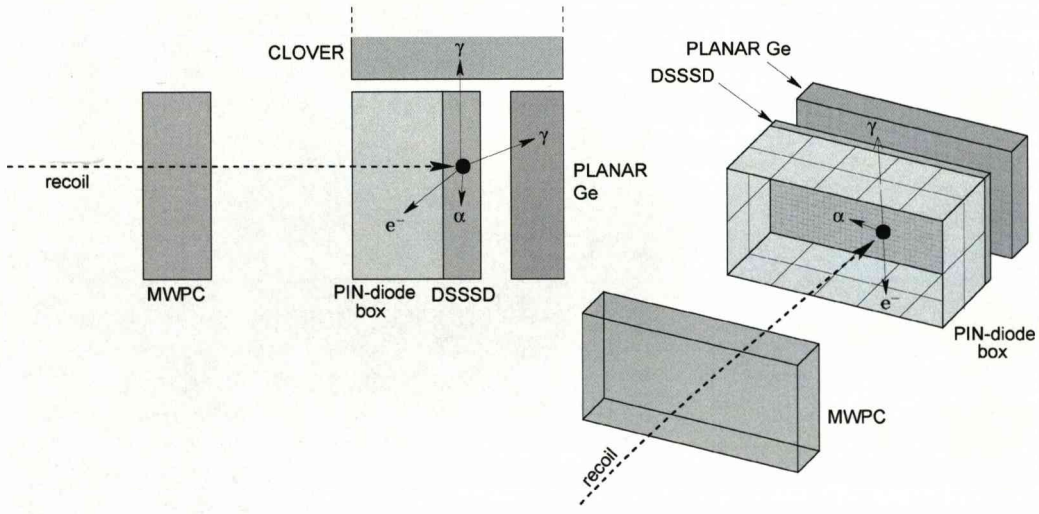

Figure 3.11: A schematic drawing of the GREAT spectrometer modified from reference [Pa05]. Recoils are implanted in the DSSSD after passing through the MWPC. Subsequent decay radiation is measured in the surrounding silicon and germanium detectors.

3.5.3 Silicon PIN photodiode detectors

Twenty eight PIN diodes are arranged in a box formation around the DSSSD to measure conversion electrons emitted by the reaction products with an active area of 28 mm × 28 mm and a thickness of 500 μm. GEANT Monte Carlo simulations [An04] have shown that for a single PIN diode the full energy electron detection peaks at 23 % for 300 keV electrons.

3.5.4 Segmented Planar germanium detector

Mounted directly behind the DSSSD, a planar germanium strip detector (PLANAR) is used to measure X rays, low energy γ rays and β particles. The PLANAR detector has orthogonal strips on both faces with a pitch of 5 mm on an active area of 120 mm × 60 mm. The detector is electrically segmented by 24 × 12 strips on the front and rear faces. Absolute photo-peak γ-ray efficiency for the PLANAR detector is calculated using GEANT Monte Carlo simulations and is displayed in Figure 3.12 [An04]. A cut-

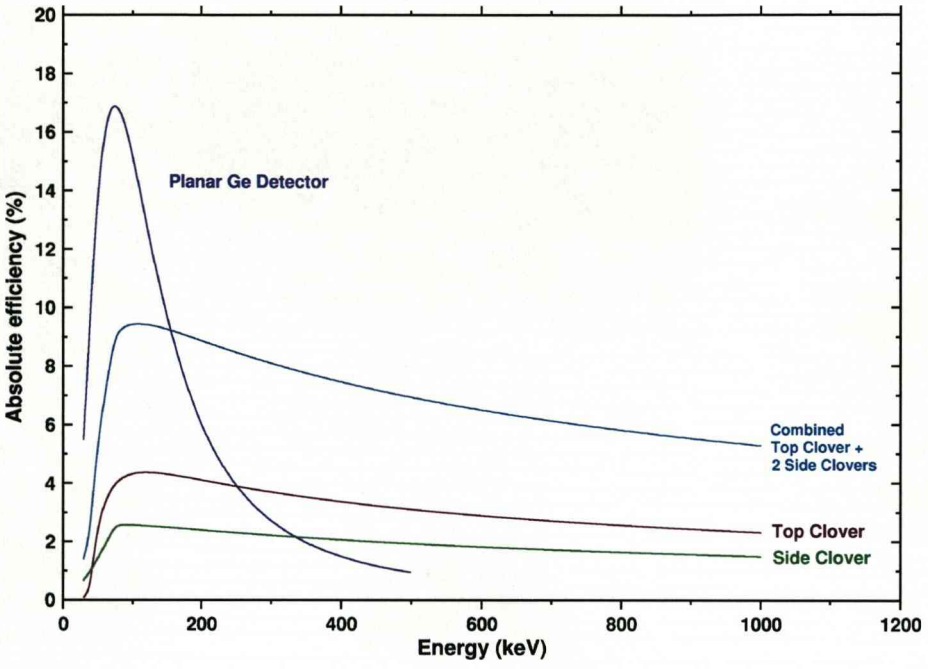

Figure 3.12: Absolute photo-peak γ-ray efficiencies calculated using GEANT Monte Carlo simulations for a series of detectors/combinations at the focal plane of RITU [An04]

off is observed at 500 keV since the high energy cut-off of this detector was set at approximately 400 keV during this study.

3.5.5 Segmented Clover detector

The CLOVER detector is mounted outside the vacuum chamber of GREAT and is used to measure higher energy γ rays. Two further detectors were positioned at the focal plane in 2006/07 to greatly enhance the detection of high energy γ-rays, their arrangement is shown in Figure 3.10. Each CLOVER has four crystals each with a diameter of 70 mm and a length of 105 mm. The crystals are tapered at 15° for the

first 30 mm of length. A bismuth-germanate Compton-suppression shield surrounds the CLOVER detector. Figure 3.12 shows the absolute photo-peak γ-ray efficiency for a top CLOVER (positioned above the vacuum chamber of GREAT) and a side CLOVER and the combination thereof calculated using GEANT Monte Carlo simulations in reference [An04].

Figure 3.13 shows the total efficiency for the configurations of Ge detectors used in experiments conducted for this study. The results are compiled from the simulated

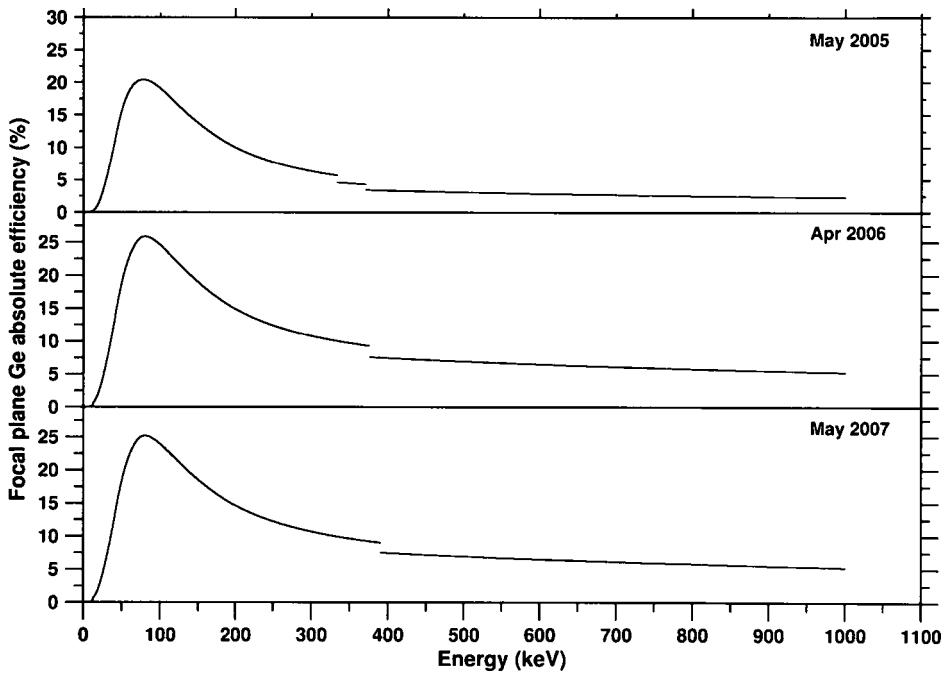

Figure 3.13: The total efficiency of the combined germanium detectors at the focal plane for each experiment performed at JYFL in this study using simulated data from reference [An04]. The reduction in efficiency at approximately 400 keV for each experiment is due to the high energy cut-off applied to the PLANAR detector. The April 2006 and May 2007 incorporated two side CLOVER detectors and hence the greater efficiency at higher energy. Other variations in efficiency arise from individual strips in the PLANAR detector being inactive during an experiment.

data used in Figure 3.12.

With regard to the JYFL PLANAR and CLOVER detectors, Reference [An04] states that the statistical errors on the reported efficiency values are small. These errors are small compared to the statistical uncertainty of the counts themselves and hence have not been used.

3.6 GSI - Experimental setup

The focal plane of SHIP consists of three time-of-flight (TOF) detectors, seven identical 16-strip position-sensitive silicon detectors and a CLOVER germanium detector, illustrated in the top right-hand side of Figure 3.9.

The three carbon foil TOF detectors are mounted 150 mm apart in front of the silicon detectors. When a heavy ion passes through the foils secondary electrons are emitted which are accelerated and transported by applied electric and magnetic fields onto a microchannel plate for multiplication. From the time-of-flight and energy information it is possible to identify different mass regions. Time resolution is measured at $\approx$ 700 ps for the detectors and each detector has an efficiency of 99.8 %, permitting good anticoincidence/coincidence measurements of recoils and decays in the implantation detector [Sa96].

The implantation or stop detector is one of the seven 16-strip silicon detectors. The detector has an active area of 80 mm $\times$ 35 mm and a thickness of 300 μm with approximately 200 effective pixels. Upstream of the stop detector are six identical silicon detectors arranged in a 2π configuration of 80 % coverage. These are used to detect those fission fragments or α-particles which escape the stop detector.

Behind the stop detector is the SHIP-CLOVER detector comprising of four crystals used for measuring γ rays. Each crystal has a length of 70 mm and a diameter of 54 mm [Ho00]. The results of a ^{152}Eu and ^{133}Ba efficiency measurement for the detector is shown in Figure 3.14 and the coefficients used to apply the fit using Equation 3.4 are presented in Table 3.4 [Su07].

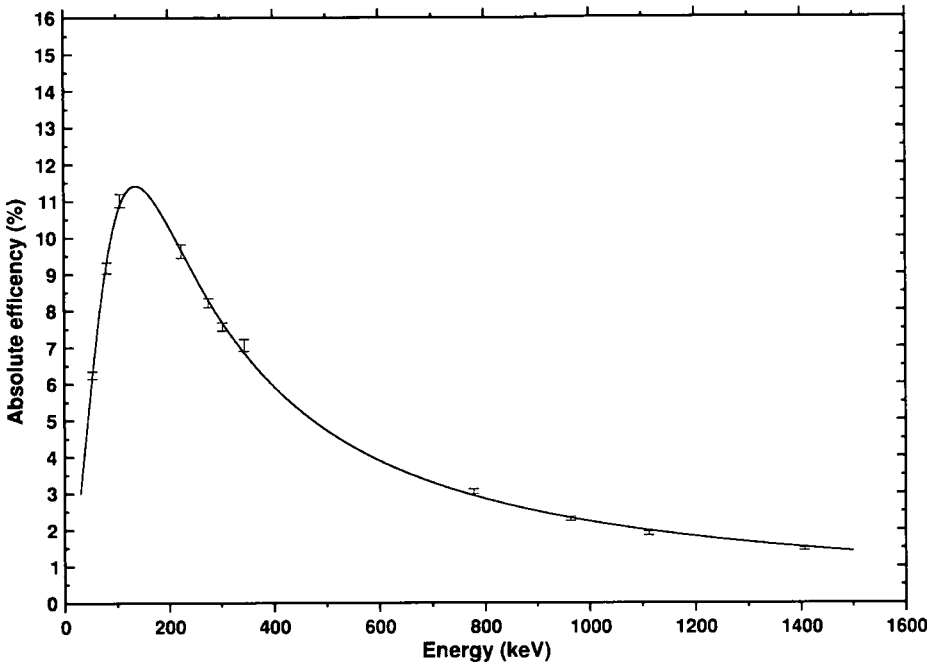

Figure 3.14: Plot of the absolute efficiency of the SHIP-CLOVER detector against γ-ray energy. The fit was applied using Equation 3.4 and data points were obtained from reference [Su07].

A = -1.29 *3000*	B = 1.40 *20*	C = 10.94 *3000*
D = -1.12 *4*	E = 5.06 *3000*	F = 0.00093 *2500*

Table 3.4: Table showing the coefficients used for the SHIP-CLOVER detector absolute efficiency calculation. The errors on the coefficients were applied to the correction of recorded transition intensities.

3.7 Data acquisition

3.7.1 Total data readout analysis

Nuclear-structure studies where isomeric states are under examination have met serious drawbacks due to the dead time arising in conventional recoil decay tagging techniques because of the necessity for long correlation gates. Total Data Readout (TDR) was developed to escape the flaws presented by hardware trigger systems where a common dead time data acquisition system was previously used. TDR allows each detector channel to be ran independently where each data word is associated with a 100 MHz clock allowing the channels to be associated in software for event reconstruction. Spatial and temporal constraints decided by the experiment specifics define the correlation of events in the software.

Let us consider an example of a recoil which is implanted at the focal plane into a Si strip detector. Using the recoil-tagging technique we set a window on the time of flight and select those γ rays associated at the target position with the recoil. Also, delayed emissions from the recoil in the strip detector are recorded (or possibly in the other surrounding detectors of GREAT). We record their x, y position and correlate to the original recoil.

When an event occurs within any detector signals are sent to the ADCs (Analog-to-Digital Converters) from linear amplifiers and via CFDs (Constant-Fraction Discriminators) by timing amplifiers. The purpose of the CFD at this point is to generate a gate and so therefore a single input can start a group of inputs. The pulse at the ADC is time stamped via the 100 MHz clock distribution from a Metronome module. The module also ensures that the ADCs remain synchronized. Patterns in the data stream are obtained using a hit-pattern module. The outputs from the ADCs and the hit pattern module, the timestamped data, are given an identity to determine from which signal they are from and which detector they were recorded in. These outputs are sent in chronological order from the buffer over a gigabit Ethernet to the event builder. Each data stream is sent to storage and to an online device for

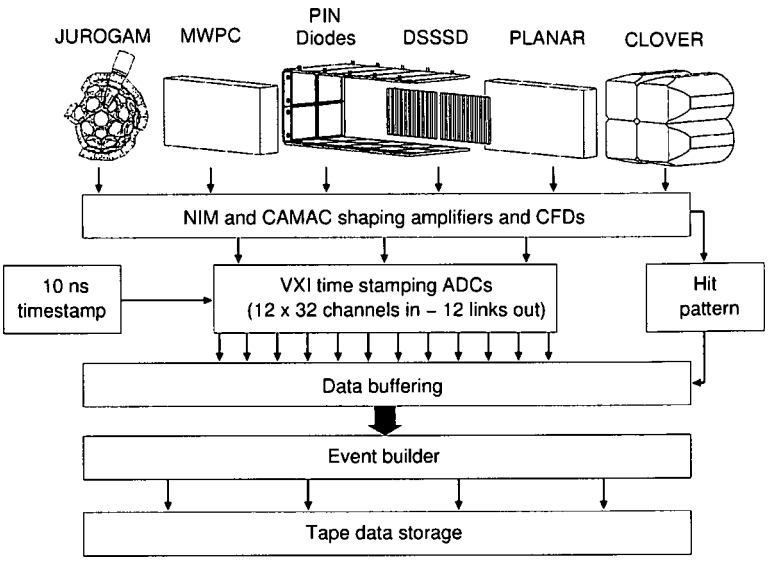

Figure 3.15: Schematic diagram of the GREAT TDR system's electronics and data acquisition [La01].

analysis [La01].

3.7.2 GRAIN analysis package

In order to analyse TDR data the GRAIN data analysis framework is used. The post-processing of the data stream is completed entirely by the Java written software GRAIN, where event building and analysis is performed by making temporal and spatial correlations to form events and the removal of irrelevant data.

The analysis is initialised using two methods. Stream filtering acts to eliminate undesired data (vetoed and pile-up) prior to building events. Secondly, event parsing acts to construct events. Any signal from the implantation detector can be used as a trigger in decay spectroscopy and tagging experiments to construct events, and the multiplicity of hits in a detector array will act as a trigger for events in in-beam experiments. Iterations on a ring buffer which holds the data objects provide access to data preceding and following a data item.

The GRAIN graphical user interface acts as the control thread for data sorting of a multithread data processing framework. The framework consists of sub-tasks including the sort engine and correlation framework which are controlled by the user whereby they write their own routines to reduce data or to implement RDT for the purpose of correlating events.

The spectra shown in the following chapters were created using the GRAIN analysis package, where one- and two-dimensional time and energy gates can be applied to produce one- and two-dimensional spectra [Rah07].

Chapter 4

Experimental Details and Analysis Techniques

4.1 Reaction specifications

The ^{254}No nuclei were produced by the ^{208}Pb(^{48}Ca,2n)^{254}No fusion evaporation reaction at a cross section of the order of 3 μb and were then separated from the primary beam-like products in the gas-filled recoil separator RITU before being detected at the focal plane.

The ^{48}Ca beam was generated in the ECR ion source, from where $^{48}Ca^{10+}$ highly charged ions were transported to the cyclotron and accelerated to an energy of 219 MeV. The targets used in this study were of a thickness of 446 μg/cm^2 on a carbon backing support. Unlike other studies in the $Z \approx 102$ region, there is no requirement to place degraders in front of the targets to reduce the beam energy to an optimum value.

Our collaborators at GSI-SHIP also made a measurement and we have been granted access to the data. It has been analysed in a PhD thesis of B. Sulignano [Sul07] and we have been able to re-analyse part of it in collaboration with GSI . In what will be outlined in Chapter 6, experimental values for the γ-ray intensity ratios between stretched E2 and mixed E2/M1 transitions for a $K^\pi = 8^-$ band could not be deter-

Experiment	JYFL May 2005	JYFL April 2006	JYFL May 2007	GSI
Beam time (hours)	148	158	61.7	55.5
Average beam intensity (pnA)	70	18	28	4300
Number of α decays recorded	$4.2{\cdot}10^4$	$1.4{\cdot}10^4$	$7.4{\cdot}10^3$	$1.6{\cdot}10^5$
$N_{slow\ isomer}$ electrons	31000	9000	3500	26000
$N_{fast\ isomer}$ electrons	4000	1700	500	3400
$Ge_{focal\ plane}$ efficiency at 134 keV (%)	15.3	20.6	20.1	11.4
JUROGAM array present	No	Yes	Yes	N/A

Table 4.1: Experimental details of the four experiments completed at two different laboratories from which data has been used in this study. Where $N_{slow\ isomer}$ is the number of electrons recorded for the slow isomer, $N_{fast\ isomer}$ is the number of electrons recorded for the fast isomer and $Ge_{focal\ plane}$ is the combined germanium detector setup, including PLANAR and all CLOVER detectors.

mined from the JYFL data. The GSI SHIP data permits this measurement allowing one to further the investigation.

The first JYFL experiment, May 2005, was carried out without JUROGAM in operation and one will also notice a lower efficiency of focal plane Ge detection for this experiment compared to the experiments performed in 2006 and 2007 at JYFL in Table 4.1. The JUROGAM array was present for the April 2006 and May 2007 experiments, which not only allowed for an in-beam γ-ray spectroscopic study of the ground state band, but also permitted the recoil-isomer tagging technique to be employed, allowing the structure built upon isomeric states to be studied. Two additional large-volume segmented Clover germanium detectors surround the focal detector chamber in experiments April 2006 and May 2007 accounting for the increase in efficiency. The beam intensities varied considerably between the experiments and are listed for completeness in Table 4.1. The omission of JUROGAM in the May 2005 experiment is due to the relatively high beam intensity. A beam of 70 pnA results in a germanium count rate approaching 1 MHz, which is too high for the current acquisition system to prevent pile-up from occurring.

Figure 4.1 shows the total number of ^{254}No α decays observed in the DSSSD for

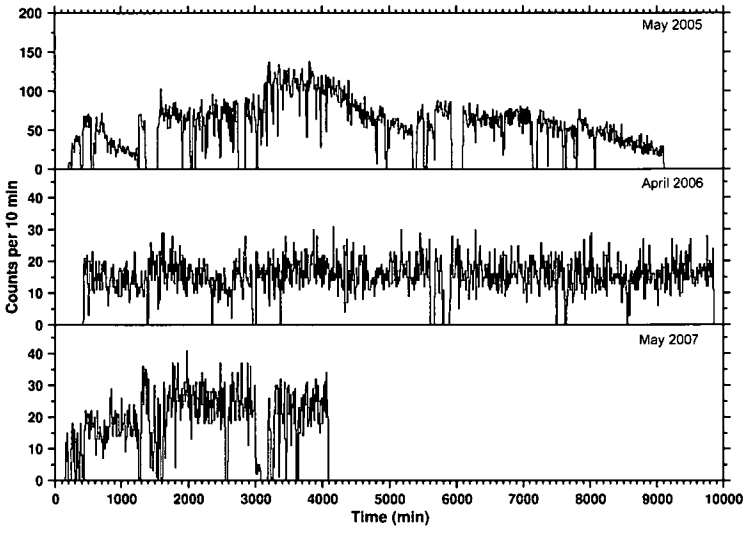

Figure 4.1: The total number of ^{254}No α decays observed in the DSSSD for each JYFL experiment as a function of time.

each JYFL experiment as a function of time. Figure 4.2 shows the events observed under a correlated alpha gating condition in the DSSSD (described in Section 4.4.1).

Data obtained at GSI SHIP is purely a decay spectroscopic study. Here the evaporation residues were implanted into a silicon stop detector, which is surrounded by six further silicon detectors. The SHIP-CLOVER detector is used to measure X rays and γ rays from implanted nuclei and decay products.

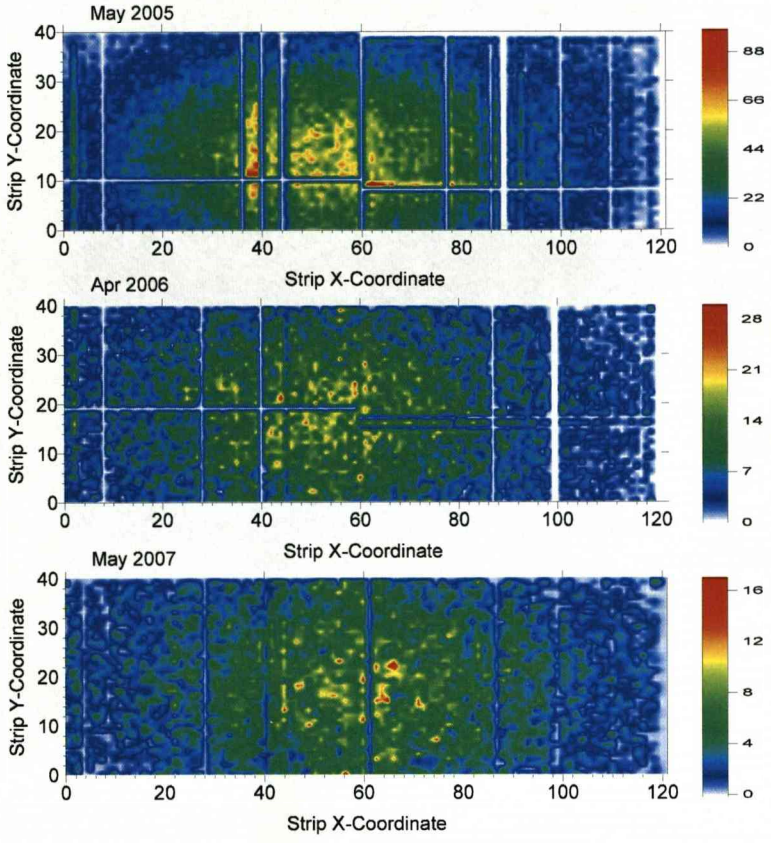

Figure 4.2: Events observed under a correlated alpha gating condition in the DSSSD (described in Section 4.4.1). The actual ^{254}No correlated α decays constitute approximately 40 % of the total events observed in each matrix. One can observe a greater intensity of events in the May 2005 experiment matrix where a beam of much greater intensity was used. The Gaussian implant distribution is also visible.

4.2 JUROGAM calibration

Energy calibration of the 43 JUROGAM detectors is performed using the known γ-ray energies from ^{152}Eu and ^{133}Ba sources (taken from reference [Tr90]) which are placed at the target position during assigned periods of calibration, both before and after

experimental runs. An energy range of 81 keV - 1408 keV is chosen for calibration which covers the region of interest for this study. A non-linear response of the ADCs is observed at low energy, illustrated in Figure 4.3. A damped sine function is subtracted from an initial cubic calibration in order to correct for this,

$$E = (a \cdot x^3 + b \cdot x^2 + c \cdot x + d) - [e \cdot exp(-f \cdot x) \cdot sin(g \cdot x + h)], \tag{4.1}$$

where E is the resulting calibrated energy and x is the channel number.

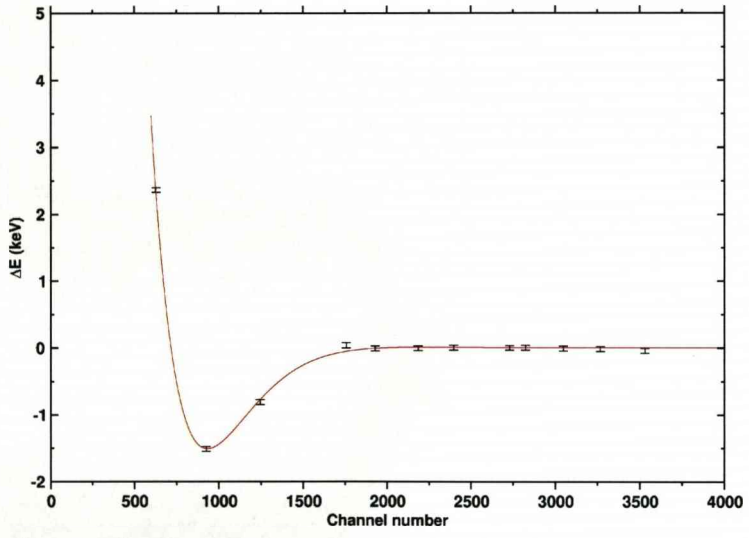

Figure 4.3: An illustration of the non-linear behaviour of an ADC for a single germanium detector. The difference between calibrated energy (performed with a cubic fit) and actual energy obtained from reference [Tr90] is plotted as a function of channel number. The data points are γ-ray transitions of ^{152}Eu and ^{133}Ba recorded during a calibration run. The red line is a fit using an exponentially damped sine function. The non-linearity observed below channel 1500 is corrected by subtracting the exponentially damped sine function from the original cubic fit. Figure modified from reference [Mn08].

4.2.1 Doppler-shift correction

The γ rays detected by the individual detector modules of the JUROGAM array are emitted by recoiling nuclei moving at a relatively high velocity. Therefore, the energy of the detected γ rays will be Doppler shifted. The observed change in the γ-ray energy E_γ is proportional to the recoil velocity υ according to

$$E_\gamma = E_0 \left(1 + \frac{\upsilon}{c} \cos\theta\right), \tag{4.2}$$

where E_0 is the γ-ray energy from a stationary frame of reference, c is the speed of light, and θ is the angle of the detector with respect to the velocity vector of the recoil.

The detector modules in each ring set are at the same angle with respect to the beam direction (Table 3.1) and therefore all detector modules have the same Doppler shift. Transitions observed in different ring sets vary in energy due to the angular dependence of the detected energy. To correct for this we measure energies of three of the strongest peaks observed in the calibration runs for each ring set and plot the energies recorded against $\cos\theta$ to obtain a value of υ/c. A υ/c value of 0.0169 was found in this study.

4.3 GREAT calibration and setup

The DSSSD is setup to measure and detect recoils and their subsequent α decays on the Y-side of the detector and conversion electrons on the X-side of the detector. The Y-side is initially gain matched to be sensitive in the energy range of 0 MeV up to $\sim$ 15 MeV. Calibration is performed using the known α energies of ^{239}Pu, ^{241}Am and ^{244}Cm which give rise to a spectrum with three dominant α peaks at 5157, 5486 and 5804 keV [Fi96]. This triple α source is positioned within the framework of GREAT and can be inserted and removed using an electromechanical system. One notable point is that the α particles from the calibration sources lose energy as they pass through the dead layer of the detector. However, this energy loss is approximately

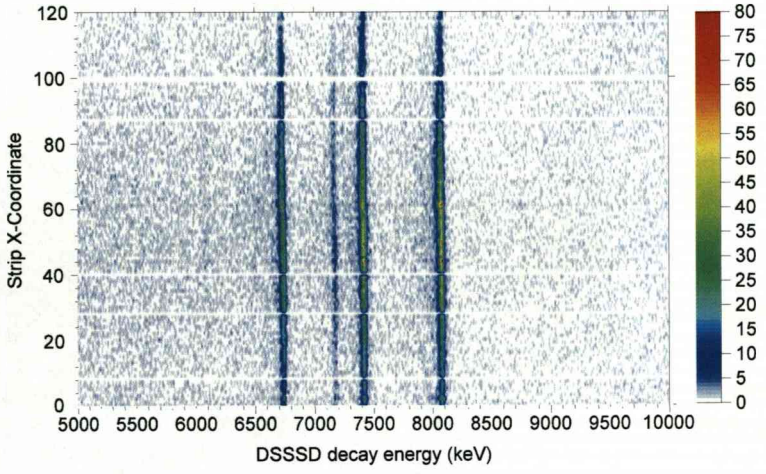

Figure 4.4: The result of the DSSSD Y-side calibration. The well defined α-decay energy of the ^{254}No α-decay chain is visible.

constant and amounts to a decrease of 40 - 50 keV for α energies within the range of 5 - 8 MeV. The purpose of this study is not to accurately measure the α-decay energies, the α-decay energy of ^{254}No is already established to a greater degree of accuracy than what is measurable with the GREAT DSSSD, but to use the recoils and subsequent α decays as events upon which to tag. Thus, the three-α source is used to align the strips, while energy calibration is taken from the ^{254}No, ^{250}Fm and ^{246}Cf α peaks.

The X-side of the DSSSD acts as a conversion electron calorimeter [Jo02], detecting conversion electrons emitted by evaporation residues populated in an isomeric state which have been implanted into the DSSSD. The energy range of the X-side is set at 0 - 1 MeV and calibration is performed using conversion electrons emitted from a ^{133}Ba source [Tr90] contained within the same electromechanical system as the triple α source.

The silicon PIN photodiode detectors are also setup to measure conversion electrons. An energy range of 0 - 600 keV is set and calibration is performed using an external ^{133}Ba source placed outside the aluminium can.

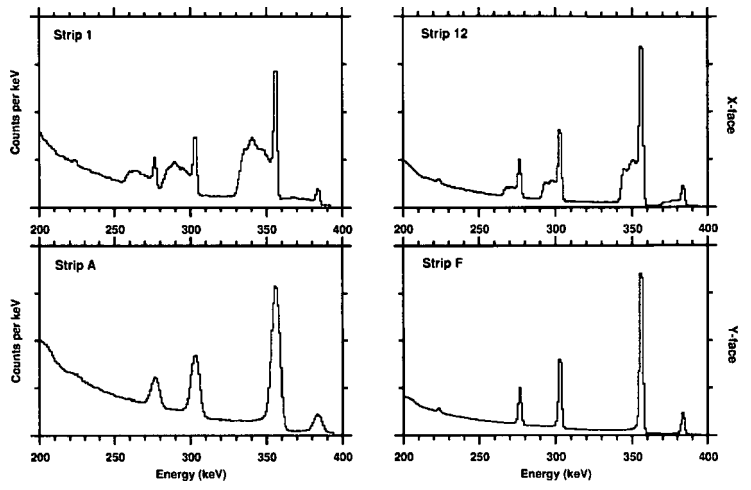

Figure 4.5: Calibration spectra of the PLANAR detector. Gamma-ray transitions from a ^{133}Ba source were used to calibrate the detector. The different behaviour of the X- and Y-faces is visible.

The PLANAR detector has an optimum efficiency up to an energy of approximately 320 keV. The detector is initially gain matched to a full energy range of up to a maximum of approximately 400 keV and we note that energies less than approximately 24 keV are not in the linear response region of the ADC cards, thus making measurements of nobelium L X-rays unreliable. Calibration is performed using γ-ray energies emitted from the external ^{133}Ba source and calibration spectra are shown in Figure 4.5. It is important to state that the GREAT PLANAR detector was a prototype. Low-energy humps on the transitions recorded in the X-face (front) of the detector have been observed and also a lower number of counts for a transition are recorded in the Y-face than the X-face.

The CLOVER detectors were configured to measure higher energy γ rays up to 2.5 MeV. Calibration was performed using a combination of external ^{152}Eu and ^{133}Ba sources within the energy range 81 keV - 1408 keV (where energies were taken from reference [Tr90]). Signals less than 150 keV do not fall within the linear response region of the ADCs so a damped sine function was subtracted from a cubic calibration,

identical to the method outlined in Section 4.2, in order to reduce this. The CLOVER detectors were operated in a single-crystal mode and we therefore calibrate via the four resulting spectra.

4.4 Nuclear spectroscopy at RITU

Two different spectroscopic techniques are used in this study, taking advantage of JUROGAM and GREAT . In-beam γ-ray spectroscopic studies using JUROGAM permit the experimentalist to determine information on the excited structure of the evaporation residue, from which information on the rotational properties of the nucleus under investigation can be gained. Isomer-decay spectroscopy is also utilised where transitions which depopulate the isomer can be measured in GREAT, and from which a half-life can be determined, and transitions which feed the isomer can be studied prompt in JUROGAM . This form of spectroscopy allows information on single-particle configurations to be ascertained via the analysis of high-K isomeric states.

4.4.1 Alpha gating

In order to distinguish between α decays and recoil events in the implantation DSSSD we engineer an alpha gate. The gate takes advantage of an anticoincidence condition one can construct between the MWPC and the DSSSD. Recoils implanted in the DSSSD would have passed through the MWPC, generating a signal prior to implantation. However, the subsequent α particle emitted from the recoil would not have passed through the MWPC, therefore allowing one to differentiate between the two. The correlation of the recoil and the ^{254}No α decay is required to meet two criteria; foremost, only α decays detected in the same pixel as the implanted recoil are registered; and of these α decays only those which are detected within a time interval of three ^{254}No α-decay half-lives are recorded (this value was set at 180 s). Figure 4.6 illustrates the different gating conditions. The green spectrum shows all of the events recorded in the Y-side of the DSSSD , consequently we observe a high level

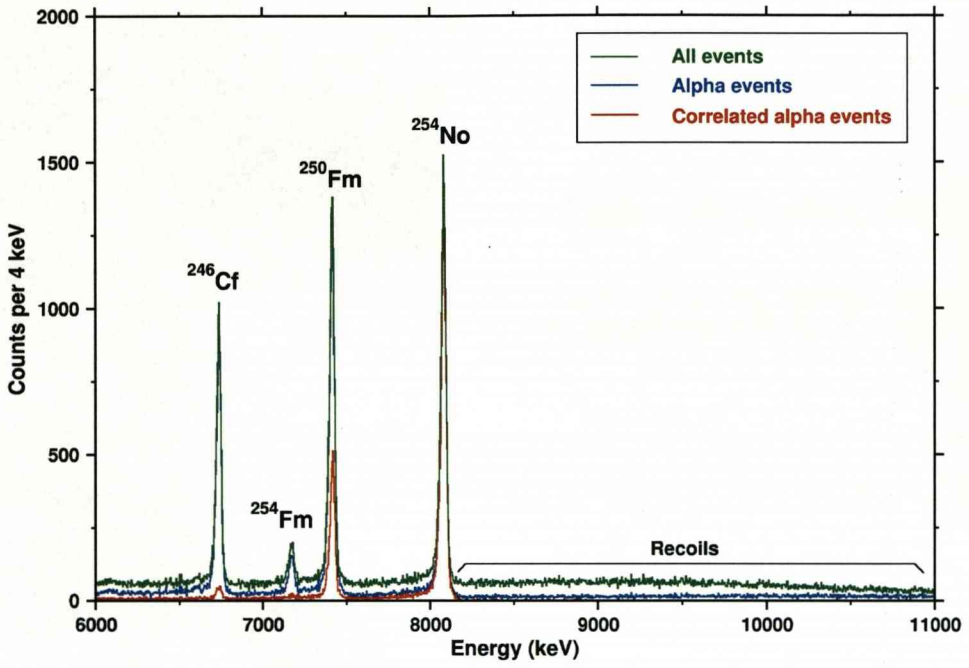

Figure 4.6: Spectrum showing the α-decay chain of ^{254}No. The green spectrum shows all events recorded in the Y-side of the DSSSD . The blue spectrum shows the events which fall under an alpha-gating condition and therefore we note a reduction in the number of recoils recorded. The red spectrum shows correlated α events where gating conditions are applied to remove non-^{254}No α-decay events.

of recoils but also the α decays in the ^{254}No α-decay chain. The blue spectrum shows those events which have met the anticoincidence condition between the MWPC and the DSSSD, thus omitting the recoil events. The red spectrum shows the correlated α events which have met both the space and time criteria, thus we observe principally the ^{254}No α decay and a decrease in the ^{250}Fm, ^{246}Cf and ^{254}Fm α decays.

4.4.2 Recoil gating

Recoil gating is implemented to identify recoils of interest from the unwanted implanted events. In order to do this two 2D histograms are incremented, one of DSSSD energy versus time-of-flight (TOF), and one of TOF versus energy loss in the MWPC, where the TOF is recorded between the MWPC and the DSSSD. The GRAIN analysis package allows the experimentalist to construct 2D gates, drawn on these matrices, thus allowing one to select only the desired recoil events. The ^{254}No recoils will have a certain TOF, DSSSD implantation energy and energy loss in the MWPC and it is this signature upon which we apply the 2D gates. Both Figures 4.7 and 4.8 show the matrices incremented by recoil events passing through the MWPC and implanted into

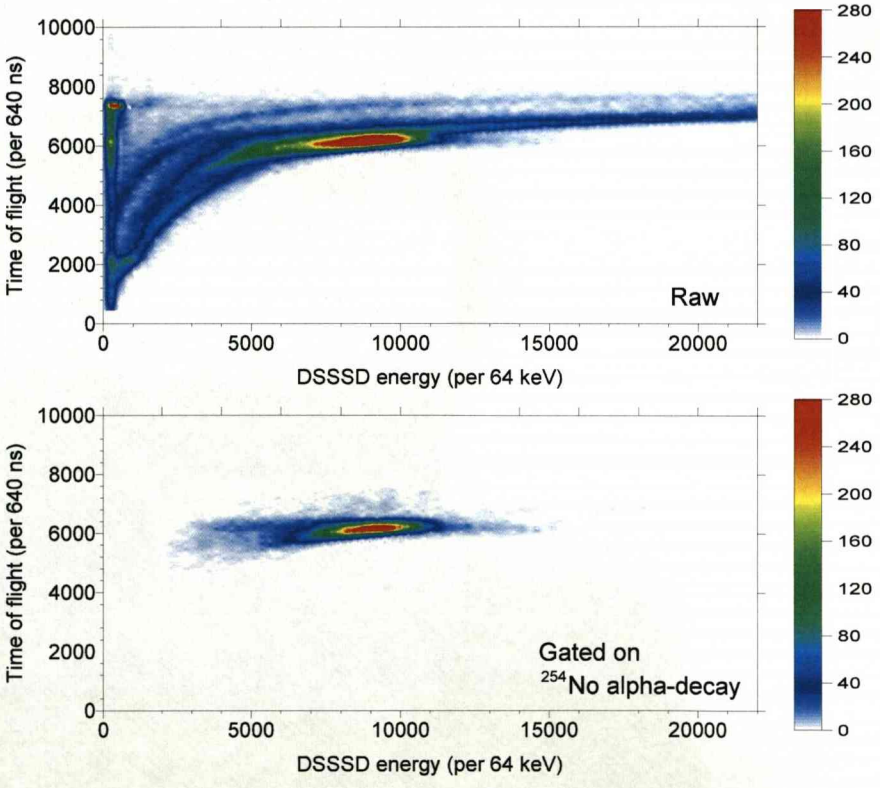

Figure 4.7: Matrices showing the DSSSD recorded energy versus time of flight, the bottom panel shows events which have complied with an alpha-correlation gating condition.

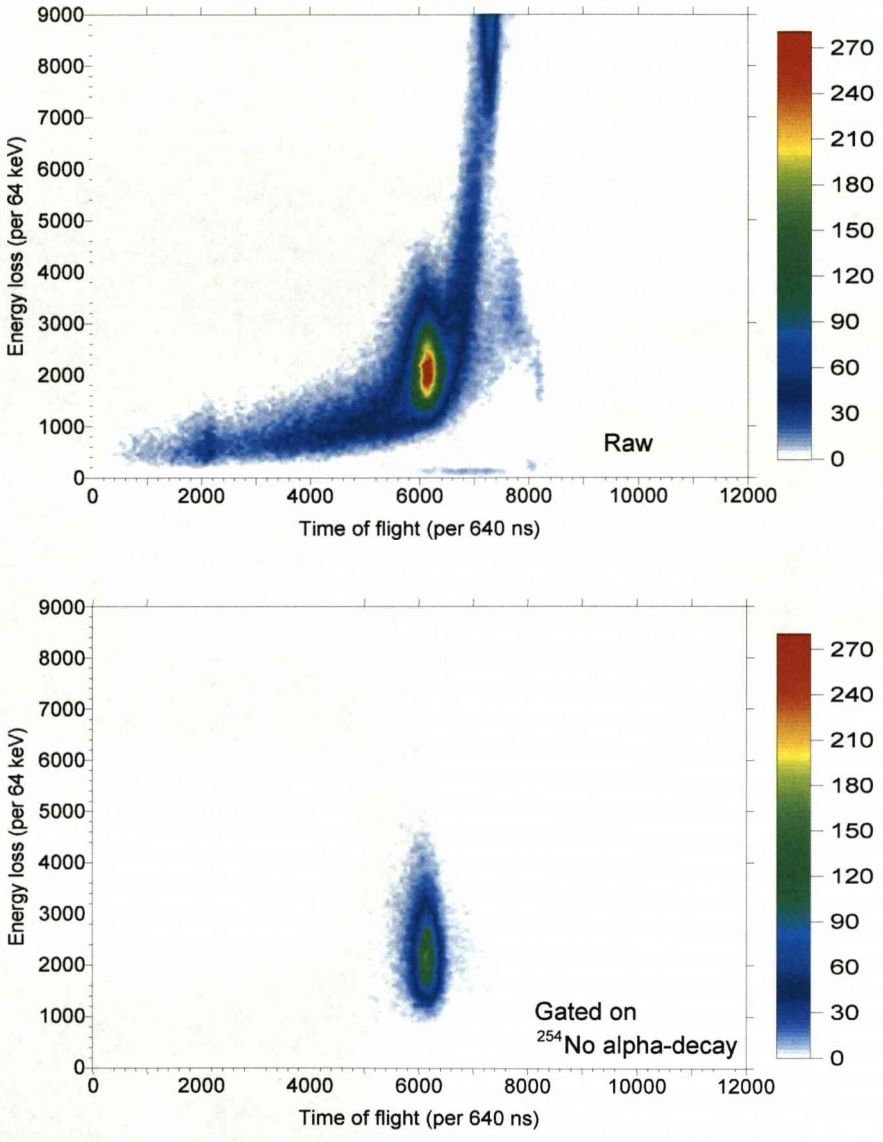

Figure 4.8: Matrices showing the time of flight versus energy loss in the MWPC, the bottom panel shows events which have complied with an alpha-correlation gating condition.

the DSSSD in order to construct the recoil gates. A guide to the drawing of the 2D gates was formulated by the matrices shown in the lower panel of each figure. These show the correlated recoil events which are followed by a ^{254}No α decay (both lower panels display an equal number of events).

The majority of the results presented in this study are obtained using the recoil tagging techniques in order to extract prompt γ rays of interest. The technique of recoil-decay tagging, correlated recoil events which are followed by a ^{254}No α decay (which satisfy the criteria outlined in Section 4.4.1), decreases the efficiency of detecting desired events, and is not utilised so as not to hinder what is already a low production cross-section study.

4.4.3 Recoil-gamma timing

Gates can also be constructed to select prompt γ rays detected at the target position by JUROGAM associated with the recoils implanted into the DSSSD at the focal plane. Recoils have a time of flight through the separator of approximately 1 μs. Using a coincidence technique we define 1-dimensional gates on the time difference between the implanted recoil and the detection of the prompt γ-ray to further remove unwanted background events.

Figure 4.9 displays examples of two JUROGAM detectors of the gates applied to the time difference. Each detector has a slightly different recoil-gamma time spectrum and so therefore the gates are applied individually for each detector module.

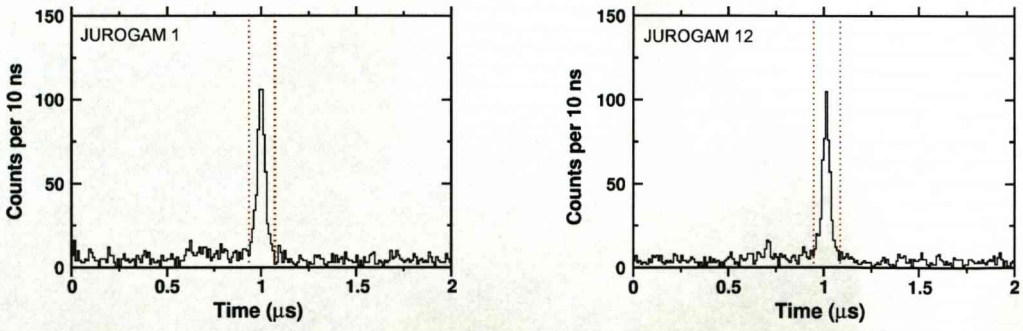

Figure 4.9: Examples of the one-dimensional gates (red lines) applied to the time difference between implanted recoils in the DSSSD and associated γ rays observed in JUROGAM.

4.4.4 Isomer-decay spectroscopy and recoil-isomer tagging

For long-lived isomers, where $T_{1/2}$ is greater then several microseconds, Jones [Jo02] proposed a method of their detection in super-heavy elements. This method is applied in this study by using the X-side of the DSSSD as an electron calorimeter.

First we shall consider a recoiling nucleus in an isomeric state which is implanted into the DSSSD, and meets the gating conditions outlined in Section 4.4.2. For the recoil to be implanted in an isomeric state then the half-life must be greater than the flight time through the recoil separator RITU, i.e. approximately 1 μs. Once the super-heavy nucleus has been implanted it will decay via a pulse of internal conversion electrons in the same pixel of the position-sensitive detector. This decay is complemented by X-rays and both low- and high-energy γ rays which are detected in the surrounding Ge detectors of GREAT.

The unique α decay of the recoil, once emitted, will allow the isomeric cascade to be tagged and thus the isomeric decay is position correlated and sandwiched in time between the implantation of the recoil and the decay of the α particle.

This concept formulates isomer-decay spectroscopy and is used to determine the transitions depopulating the isomers outlined in Sections 6.4 and 6.5, and to also determine the half-lives of the isomeric states.

In addition, recoil-isomer tagging operates by selecting the prompt transitions observed in the JUROGAM array which are associated with the recoils implanted into the DSSSD which have decayed via an isomeric transition. This permits one to identify the transitions which feed the isomeric state. Results showing transitions identified as being built on top of the isomeric state are presented in Section 6.5. Figure 4.10 outlines the principles of gating and tagging techniques used in this study.

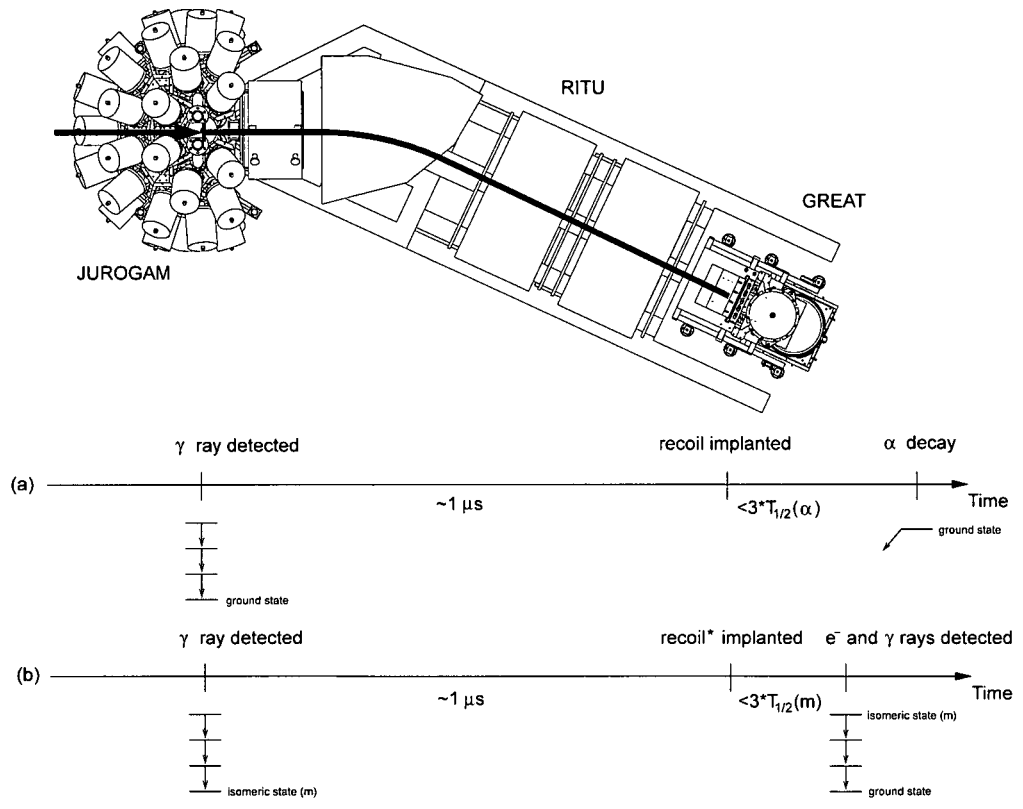

Figure 4.10: Schematic representation of the gating and tagging techniques used in this study. Panel (a) depicts recoil-gating and recoil-decay tagging and panel (b) depicts isomer decay spectroscopy and recoil-isomer tagging. Figure modified from references [Ee06, Mn08] and the line drawing of the experimental setup was supplied by reference [Se07].

Chapter 5

Previous Knowledge and Motivation

In this chapter we will outline the underlying problems associated with the positioning of the spin-orbit partners which affect the location of potential shell gaps and how experimental results in the transfermium region, namely the study of isomeric states, can pave the way to a greater understanding.

5.1 An overview

To probe the super-heavy region it has proved advantageous to study the well-deformed prolate nucleus ^{254}No. The nobelium isotope has a sufficient cross-section, 3μb via the heavy ion fusion evaporation reaction ^{208}Pb(^{48}Ca, 2n)^{254}No, to allow for analysis compared to its relatively heavier counterparts in the super-heavy region. In Figure 5.1 one can see the decrease in production cross sections as we move to heavier masses via the $1n$ channel and the inset shows the increase in cross-section for the $2n$ channel for the ^{48}Ca induced fusion reaction of the compound nucleus $Z = 102$.

The excited states that have previously been observed in ^{254}No [He06, Ta06] are highly significant, their location is sensitive to single-particle levels above the gap in shell energies predicted at $Z = 114$. The single-particle orbitals split according

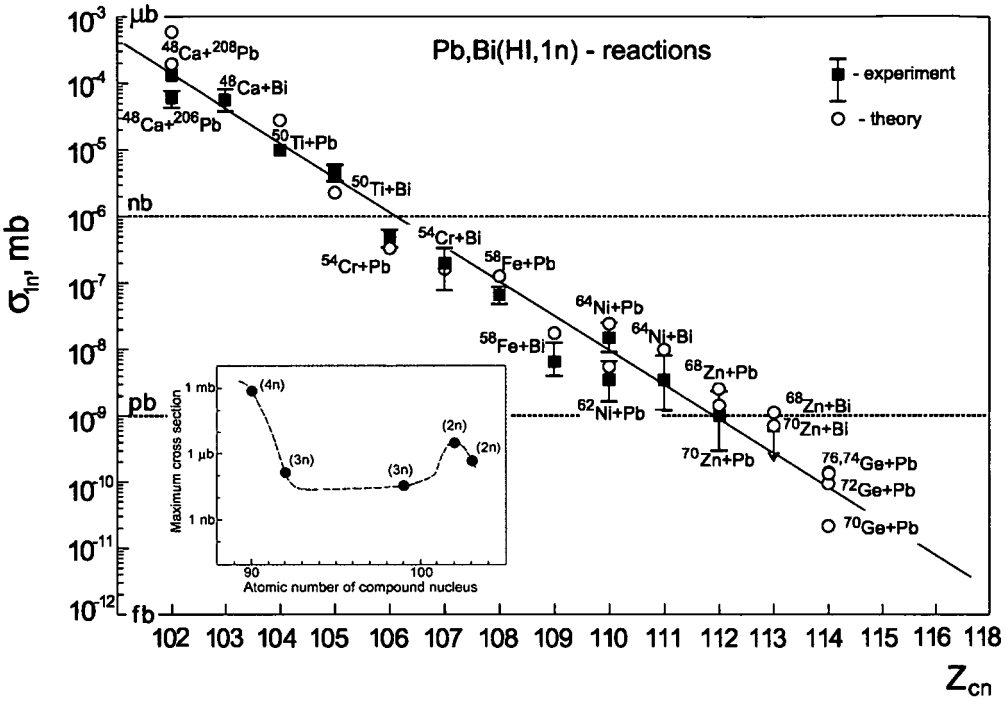

Figure 5.1: Main: Experimental data (black squares) and theoretical calculations (open circles) for synthesis of elements from 102 to 114 in cold fusion reactions (HI,1n), figure modified from Reference [Ch04]. Inset: Maximum cross sections for the main xn channels from ^{48}Ca-induced fusion reactions, modified from Reference [Gä89].

to the projection of the angular momentum onto the symmetry axis, K, which can hold a considerably large value. The γ-ray transitions from high-K to low-K bands are strongly hindered and thus lead to the formation of long-lived high-K isomers [Wa99]. Using the branching ratios of the transitions within these high-K bands we can measure an intrinsic g-factor, g_K, the contribution to the magnetic dipole moment from a valence or excited nucleon, to assist in the definition of the components of the single-particle structure.

5.2 Rotational structure

A large body of data on rotational bands in the $Z \approx 102$ region exists, providing experimental confirmation of large quadrupole deformations [He08]. In 1999 ^{254}No was the first transfermium nucleus whose rotational structure was established. Reiter *et al.* [Re99] conducted an in-beam experiment at the Argonne National Laboratory (ANL) using the reaction ^{208}Pb(^{48}Ca, $2n$)^{254}No, where γ-rays were identified by GAMMASPHERE using the recoil decay tagging technique. The ground state band was identified up to spin $14\hbar$, where the energies of the two lowest transitions, $2^+ \rightarrow 0^+$ and $4^+ \rightarrow 2^+$, were deduced by extrapolation. The ground-state band transitions were shown to exhibit rotational characteristics and a quadrupole deformation parameter of $\beta = 0.27 \pm 0.02$ was deduced. More recently the ground-state band was extended up to spin $24\hbar$ [Ee05].

There are a number of ground-state rotational bands of even-even nuclei in the heavy actinide region which have been identified. Notable systematics of known excited states in the curium isotopes ($Z = 96$) include ^{242}Cm, where the ground-state band has been extended up to spin $24\hbar$ from observations using the GAMMASPHERE array and the isotope ^{248}Cm is well examined up to a spin of $30\hbar$ [Ab04]. The ground state band of ^{246}Cm is tentatively extended from spin $8\hbar$ up to $26\hbar$ by the observation of transitions in a measurement of ^{248}Cm yrast band transitions where the two lowest transitions had the same known energies (within 0.5 keV) as the $8^+ \rightarrow 6^+ \rightarrow 4^+$ cascade in ^{246}Cm [Ha98].

Information on the ground-state rotational bands of californium isotopes ($Z = 98$) is far less extensive than that of the curium isotopes. The isotopes ^{248}Cf and ^{250}Cf are both known up to spin $6\hbar$, where studies were conducted through the α decay of ^{252}Fm and ^{254}Fm, and in the case of ^{250}Cf additionally by the electron capture decay of ^{250}Es [Ah84, Rei79, Fr77].

Of the fermium isotopes ($Z = 100$), ^{250}Fm has been studied the most comprehensively. Several in-beam experiments have been conducted utilising the JUROGAM array at JYFL establishing the ground state band up to spin $22\hbar$ [Gr08]. The SACRED

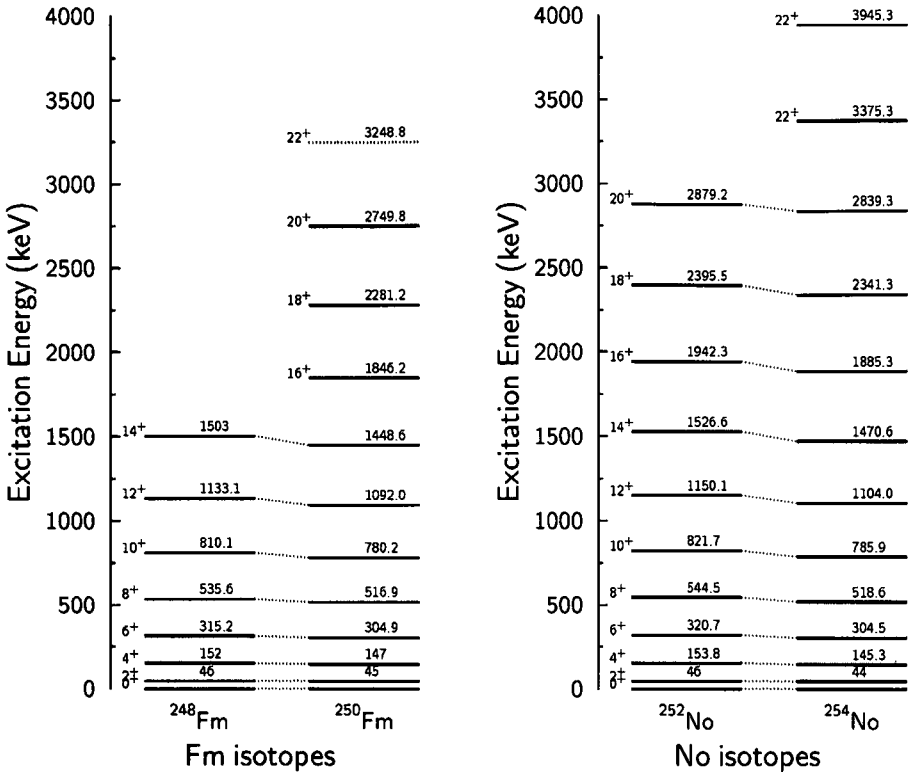

Figure 5.2: Known systematics of the ground-state rotational bands in selected fermium and nobelium isotopes. Figure modified from reference [He08].

spectrometer at JYFL, used to measure the internal conversion electrons emitted in the decay of ^{250}Fm, allowed the energy of the $4^+ \rightarrow 2^+$ transition to be determined [Ba06].

The only other isotope of nobelium ($Z = 102$) for which the ground-state structure has been investigated is ^{252}No. Evaporated particles were used as a tag for prompt γ-rays to establish the ground state band up to spin $20\hbar$ [He01]. Figure 5.2 shows several ground-state rotational bands of selected fermium and nobelium isotopes.

Properties of these rotational structures are believed to provide information on a number of high j-orbitals which arise from the spherical subshells in the area of the

predicted shell closures.

5.3 Motivation given by theoretical predictions

One of the main driving forces for spectroscopy in this area is that as we move towards the super-heavy region then the traditional picture of shells, closed shells especially, starts to dissolve. At the known magic numbers the results of various parameterisations of the Skyrme-Hartree-Fock (SHF) and the Relativistic-Mean-Field (RMF) approaches within the self-consistent mean-field model lead to distinctly defined regions of enhanced shell energy. However, when the SHF and RMF approaches are applied to the super-heavy region wide areas of enhanced shell correction energy are observed. This wide area of shell stabilisation invalidates the concept of magic numbers and the familiar pattern of separated shells disappears [Be01].

Within this area we observe regions of lower level density around the Fermi surface which results in an overall stabilization of the nuclei, providing rather large regions of additional shell stabilization and therefore leading to an island of super-heavy stabilized nuclei. If we want to study and probe the single-particle structure in the super-heavy region then we need to examine deformed nuclei where the orbitals loose their degeneracy and split up according to their quantum number. The $Z = 114$ gap is at the heart of the debate as to where the next spherical magic gap is positioned. It is created by opening up the spin-orbit interaction between the proton $2f_{5/2}$ and $2f_{7/2}$ spin-orbit partners. The $2f_{5/2}$ low Ω component from above $Z = 114$ is driven down by deformation to lie close to the Fermi surface in the fermium and nobelium region, Figure 5.3.

The choice of Nilsson diagram and the position of the spherical states is one of the key problems for theorists in this region. For example, in Figure 5.4, which is a relatively new calculation compared to that of Figure 5.3, we observe that the $1i_{13/2}$ state, with its large degeneracy, has moved into the $Z = 114$ gap, with the $2f_{5/2}$ and $2f_{7/2}$ either side. The size of these gaps are fundamental to the nucleus structure and

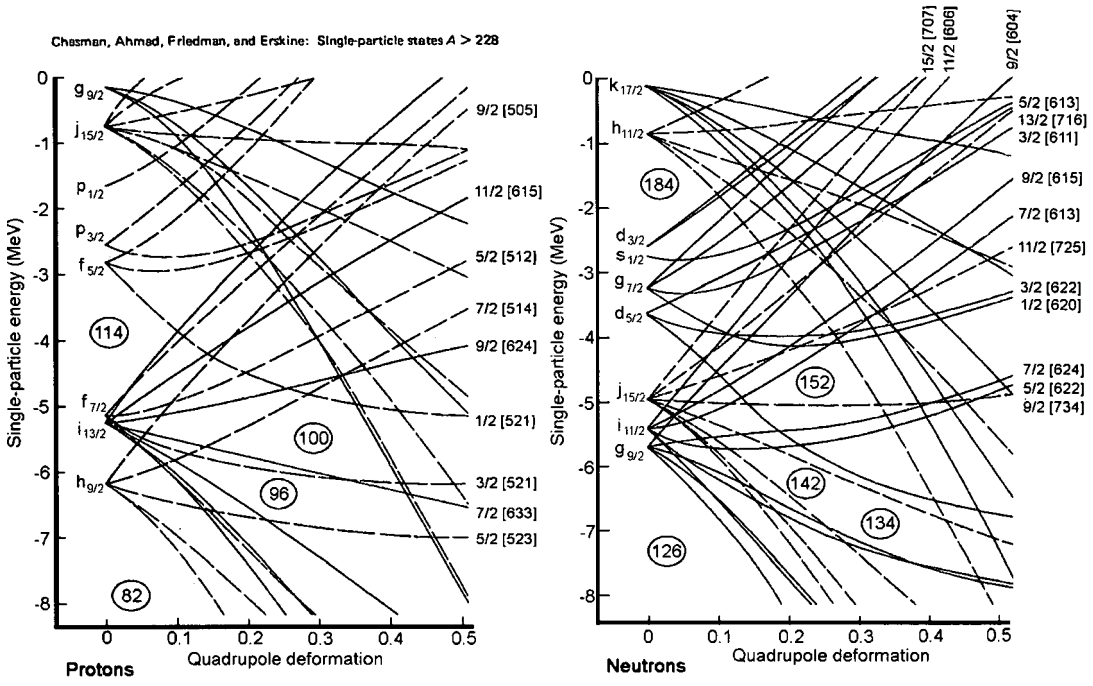

Figure 5.3: Plots of single-particle levels obtained from a momentum dependent Woods-Saxon potential as a function of quadrupole deformation. These calculations were made in 1977, more recent calculations place the proton $1i_{13/2}$ within the Z=114 gap. This proton single-particle level plot clearly illustrates the Z=114 gap created by opening up the spin-orbit interaction between the $2f_{5/2}$ and $2f_{7/2}$ spin-orbit partners. On the right hand side the neutron single-particle levels are shown with a deformed shell gap at N=152, enclosed by the $1/2^+[620]$ and $9/2^-[734]$ single-particle states. Figure modified from reference [Ch77].

creates a huge challenge. If we analyse most of these calculations then we find at the heart of most of the discrepancies are the positions of the high-j orbitals for both protons and neutrons.

To reiterate, if we draw our attention to Figure 5.5, where we have taken another set of calculations with predictions made by Bender [Be99] for shell positions for $^{298}114$, we see that the Fermi surface and the orbitals close to it are consistent. The order and spacing of individual single particles away from the Fermi surface is difficult

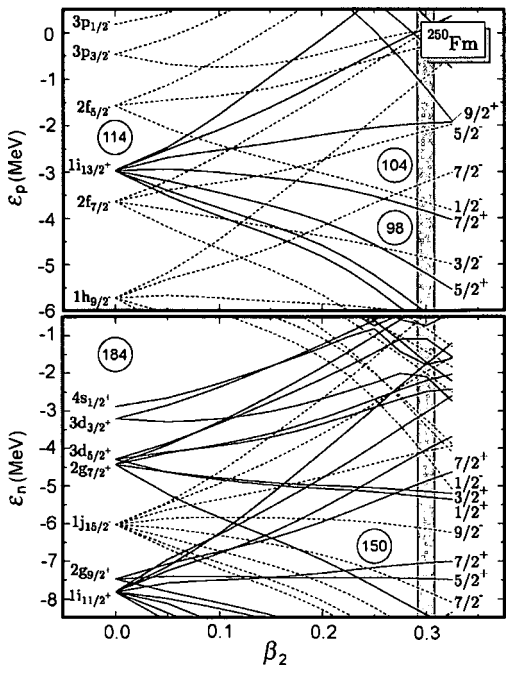

Figure 5.4: Single-particle spectra of ^{250}Fm obtained with the SLy4 interaction for protons (top) and neutrons (bottom). Figure modified from reference [Cha06].

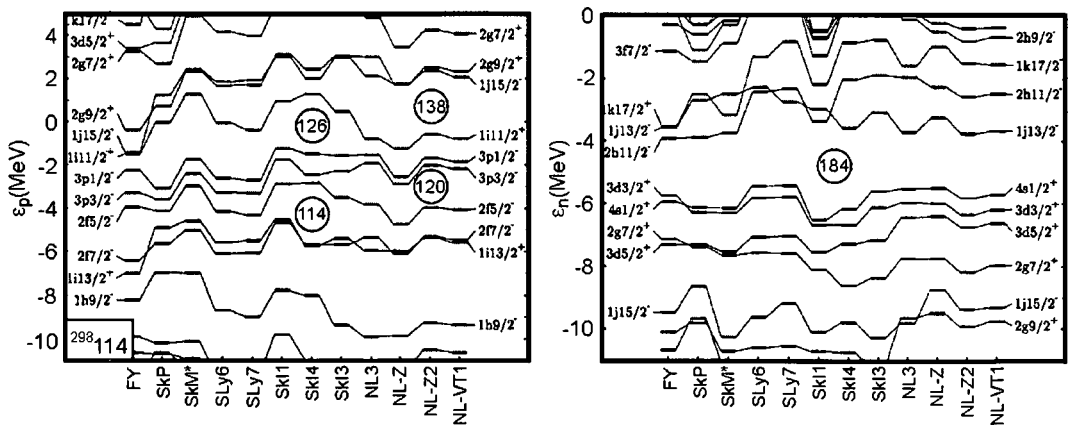

Figure 5.5: Shell positions for ^{298}114. Protons (left) and neutrons (right) at spherical shape for a range of mean-field forces. Figure modified from reference [Be99].

to produce consistently. One of the main reasons for these uncertainties is the spin-orbit term itself which is related to the nuclear density. If one looks into the region of super-heavy nuclei then we observe many populated high j orbitals close to the surface leaving a smaller density inside the nucleus which effects the positioning of the spin-orbit partners.

5.4 Isomers

One key ingredient that we have at our disposal to solve the underlying problems associated with the location of the potential shell gaps is that of isomeric states. Isomers provide a very clean signal allowing one to obtain unobstructed information which can play an important role in pinning down the position of these single particle states.

5.4.1 Isomeric states at the extremities of the Segré chart

Nuclear isomers play an important role at the extremities of the nuclear landscape. One point of significant interest is the nucleus ^{270}Ds, which was synthesized using the reaction ^{64}Ni + ^{207}Pb at GSI, where decay data for a high-spin isomer was obtained [Ho01]. Another isotope of darmstadtium has been shown to possess an isomeric state. Experiments performed by Hoffman at GSI [Ho95, Ho98, Ho03] and independently by Morita at the Institute of Physical and Chemical Research (RIKEN) have provided evidence for an isomeric state in ^{271}Ds [Mo04]. Enhanced stability against both fission and α decay is an advantage of studying long-lived excited states rather than the ground state in super-heavy nuclei [Xu04], for example Figure 5.6.

5.4.2 Isomeric states observed in ^{254}No

Ghiorso *et al.* were the first to report on an isomeric state in ^{254}No and ^{250}Fm [Gh73]. An indication of a short-lived component of ^{254}No arose during a study of the properties of ^{257}Rf. Via a bombardment of ^{249}Cf with ^{12}C ions, supplied by the Berkeley

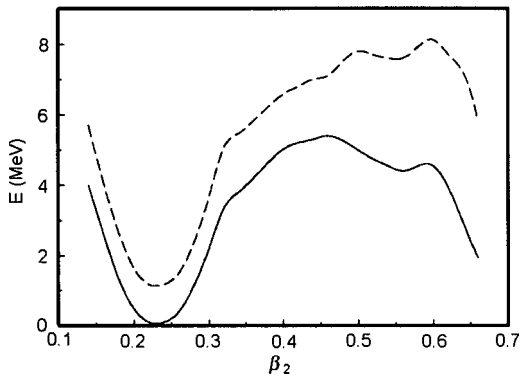

Figure 5.6: Calculated potential energies versus β_2 deformation in ^{256}Fm. The fission barrier for the ground state is represented by a solid line and the fission barrier for the $7/2^+[633]_\pi \otimes 7/2^-[514]_\pi$ isomer is represented by a dashed line. Here the stability against fission is greatly enhanced within the isomeric state. Figure modified from reference [Xu04].

heavy-ion linear accelerator, evidence for the existence of a 0.28±0.04 s isomeric state in ^{254}No was derived from the α-particle spectrum. The isomeric ratio σ_m/σ_g was reported to be 0.2 when ^{12}C ions of energy 73 and 81 MeV bombarded ^{249}Cf. In 2002, conversion electron cascades in ^{254}No were presented by Butler *et al.* [Bu02]. In an experiment conducted at JYFL employing the electron spectrometer SACRED, a conclusion was reached that the observed $M1$ cascades arose partially from the population of quasi-particle excitations with high-K values. Lower ground-state band transitions, notably the $4^+ \rightarrow 2^+$ transition, were identified from the L- and M- conversion electrons, but the additional intensity observed in the spectrum was attributed to be from low-energy transitions in high-K bands (Figure 5.7). Further progress has been made in the characterisation of the high-K bands in ^{254}No over the last few years. Independently, teams from ANL [Ta06] and JYFL [He06] have both observed high energy γ-rays at 842 and 943 keV which are due to the decay of a $K^\pi = 3^+$ band-head state. Theoretical studies have predicted a two quasi-particle $K^\pi = 8^-$ isomeric state to lie at approximately 1.5 MeV and this was confirmed experimentally. A short-lived isomer was also unambiguously identified with a half-life of 184 μs, which feeds the K^π

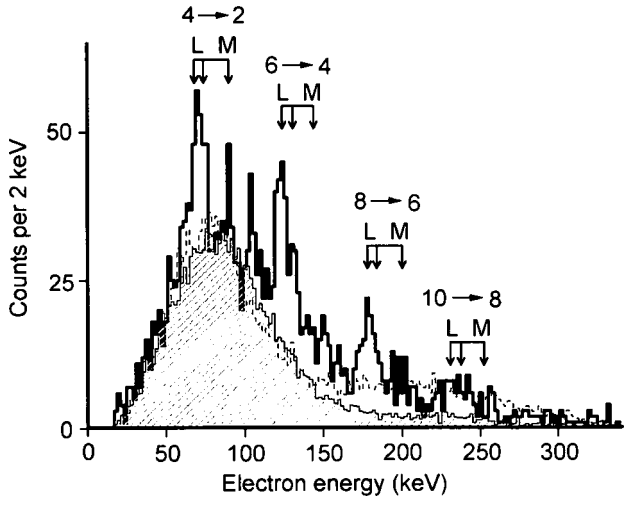

Figure 5.7: A recoil-gated conversion electron spectrum for ^{254}No measured using the SACRED spectrometer coupled to RITU . The shaded area corresponds to simulated spectra for $g_K = 0$ and g_K - $g_R = 0$. Figure modified from reference [Bu02]

$= 8^-$ band. Current understanding and theoretical predictions regarding the high-K states in ^{254}No are summarised in Figure 5.8. Figure 5.9 illustrates the level scheme of ^{254}No compiled from previous work [He06] preceding this study.

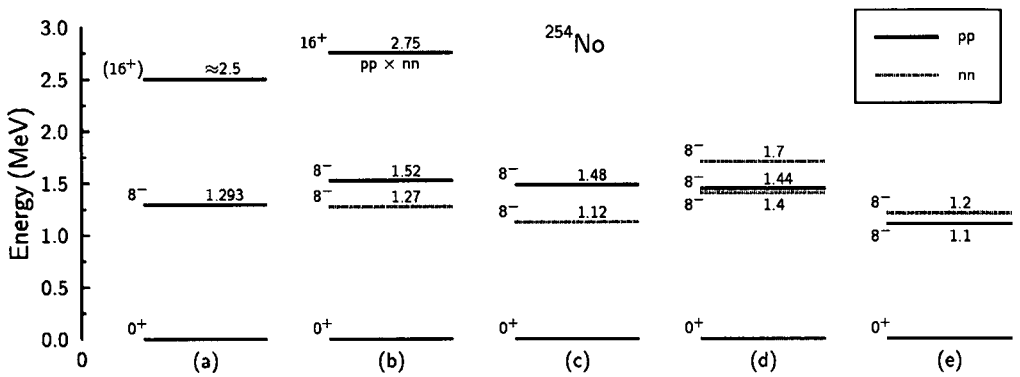

Figure 5.8: Previously derived experimental and suggested configurations of the high-K isomeric states in ^{254}No. Column (a) depicts the experimental findings given in Reference [He06]. Columns (b)-(e) show suggested configurations where the two quasi-proton configuration, $\{7/2^-[514]_\pi \otimes 9/2^+[624]_\pi\}^{(8-)}$, is given throughout. A two neutron-configuration, $\{7/2^+[613]_\upsilon \otimes 9/2^-[734]_\upsilon\}^{(8-)}$, is also given, (b)-(e), and a higher-lying two quasi-neutron configuration, $\{7/2^+[624]_\upsilon \otimes 9/2^-[734]_\upsilon\}^{(8-)}$, at 1.7 MeV is provided in Column (d). (b) reference [He06]; (c) reference [Xu04]; (d) reference [So91]; (e) reference [Laz89]. Figure modified from reference [He06].

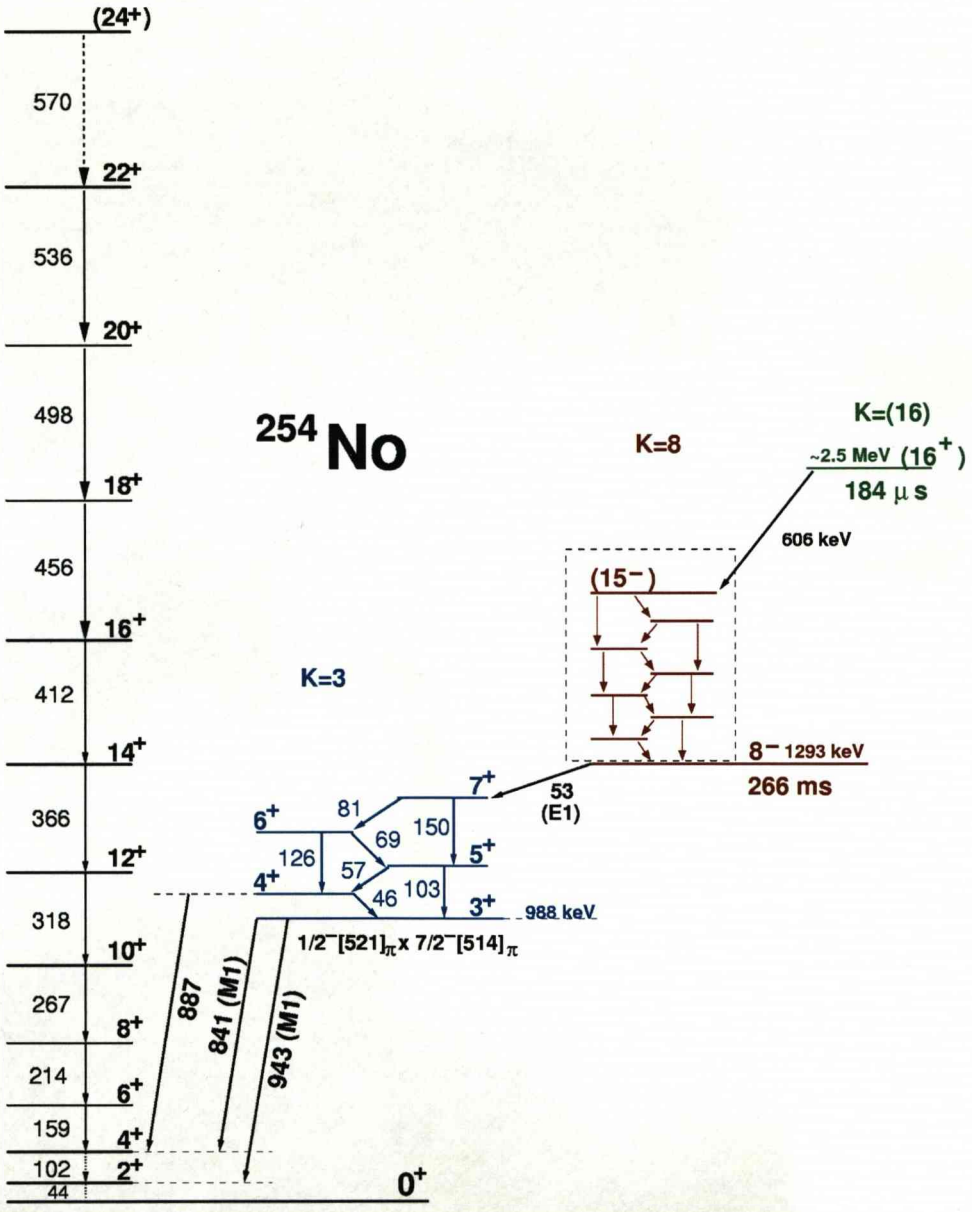

Figure 5.9: Level scheme of ^{254}No compiled from previous work [He06]. The reader is directed to the level scheme displayed in Figure 7.8 to deduce what has been added by this study.

Chapter 6

Experimental Results

6.1 A brief synopsis of the experimental details

This chapter presents the results obtained. Unless otherwise stated the results shown are a compilation of three different experiments conducted at JYFL to determine the structure of high-spin states of the transfermium nucleus ^{254}No. Table 4.1 outlines the experimental details of these three. Results from all three are independently efficiency corrected and then combined. In-beam and decay spectroscopy results are presented, utilizing the detector configuration at JYFL.

Figure 6.1 displays the α-decay chain of ^{254}No from the April 2006 experiment. The results have met the anticoincidence condition between the MWPC and the DSSSD, outlined in Section 4.4.1, thus removing recoil events from the spectrum. The ground state of ^{254}No α-decays to the daughter ^{250}Fm. The α-decay granddaughter, ^{246}Cf, and the electron-capture daughter, ^{254}Fm, are also recorded.

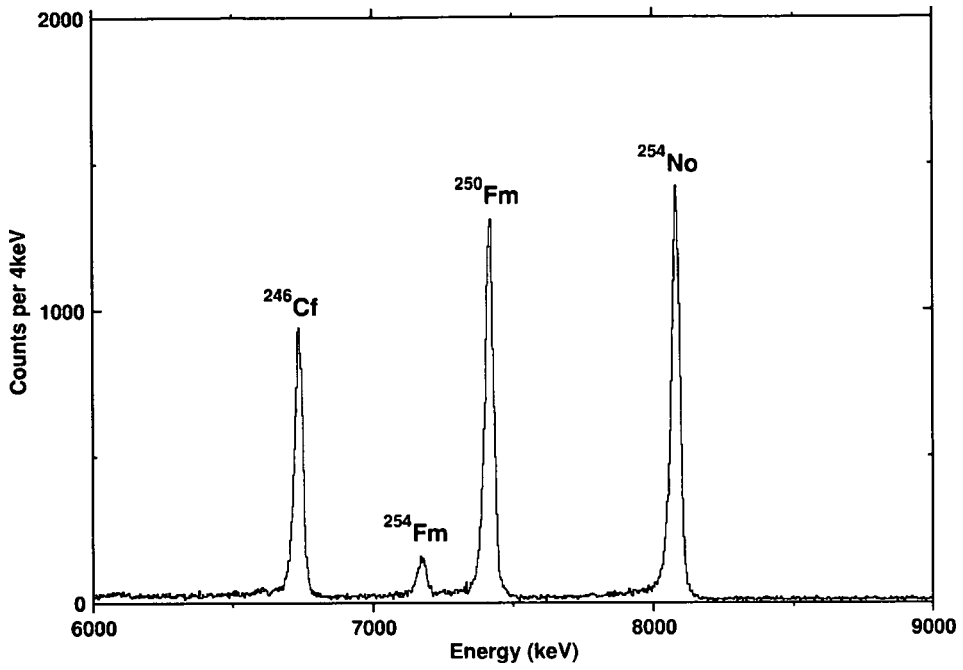

Figure 6.1: Alpha-decay spectrum (vetoed with the MWPC) of ^{254}No obtained in the JYFL April 2006 experiment.

6.2 Half-life measurement

Via the implementation of the RDT technique one can calculate the half-life of the ^{254}No α decay. Upon identification of a recoil implantation and subsequent α decay in the same pixel of the DSSSD, we measure the correlation time difference between the two. This period of time is fixed to approximately 20 half-lives to ensure that the α events from ^{254}No have decayed. A problem of random correlation arises due to the possibility of a second recoil implanting into the same pixel of the DSSSD before the first recoil has α decayed. To overcome this discrepancy a double exponential curve is fitted to the decay curve with two components, τ_{short} and τ_{random}, which are related

to the true lifetime by

$$\tau_{true}^{-1} = \tau_{short}^{-1} - \tau_{random}^{-1}. \tag{6.1}$$

The double exponential used to fit the data was of the form

$$N(t) = A \cdot exp\left(-\lambda_{random} t\right) + B \cdot exp\left(-\lambda_{short} t\right). \tag{6.2}$$

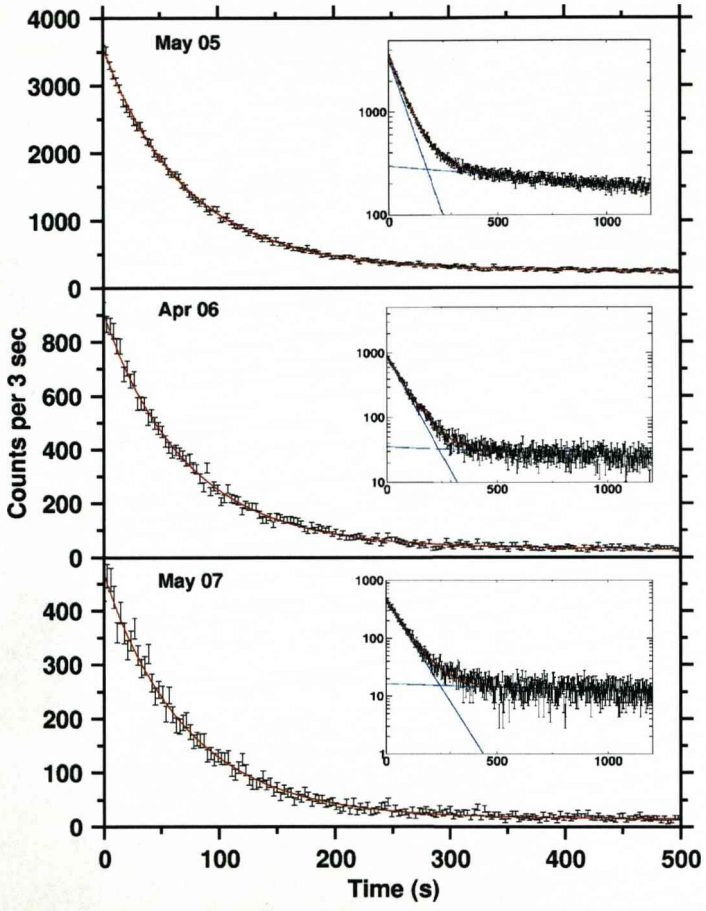

Figure 6.2: Decay curves for the ground state of ^{254}No. A maximum correlation time of 20 minutes was used to allow for an accurate estimate of the random background. Blue lines overlaid on top of the plots represent the random and short contributions.

Experiment	τ_{short} (s)	τ_{random} (s)	τ_{true} (s)	$T_{1/2}$ (s)
May 2005	71.7 *5*	2465 *100*	73.9 *6*	51.2 *4*
Apr 2006	71.4 *9*	2900 *400*	73.2 *9*	50.7 *6*
May 2007	71.7 *12*	3300 *750*	73.3 *13*	50.8 *9*

Table 6.1: Measurements of half-lives for each of the three JYFL experiments. Random and short components of the decay curve were measured to generate a true lifetime.

Calculations of the half-life from the three JYFL data sets have been performed separately because the random contribution is different in all three. If we were to sum the data sets and then perform the calculation then the random contribution would be dominated by that of the May 2005 experiment. For the May 2005 experiment a calculation of the two components resulted in $\tau_{short}^{May05} = (71.7\pm0.5)$ s and $\tau_{random}^{May05} = (2465\pm100)$ s. Using equation 6.1 the true lifetime was determined to be $\tau_{true}^{May05} = (73.9\pm0.6)$ s and thus the half-life was found to be $T_{1/2}^{May05}=(51.2\pm0.4)$ s. Table 6.1 summarises the half-life results for all three experiments.

We combine the three results using the following equations,

$$T_{1/2} = \frac{\sum(T_{1/2i}/\Delta T_{1/2_i}^2)}{\sum(1/\Delta T_{1/2_i}^2)}, \tag{6.3}$$

$$\Delta T_{1/2} = \sqrt{\frac{1}{\sum(1/\Delta T_{1/2_i}^2)}}, \tag{6.4}$$

to obtain a best estimate and accuracy of $T_{1/2}=(51.0\pm0.3)$ s. The value is consistent with the most recent data evaluation in the ENSDF data base (June 2008) of (48 ± 3) s [Le99].

6.3 In-beam γ-ray spectroscopy of the ground-state band

6.3.1 Recoil-decay tagged spectra

A clearly defined rotational band structure, characterised by a regular sequence of γ-ray transitions, built upon the ground state is shown in Figure 6.3. It is assumed that these γ-rays are stretched E2 transitions but due to the low level of statistics no angular correlations can be performed to categorize the multipolarity of the transitions. All transitions labelled in the recoil tagged spectrum are observed in the recoil-decay tagged spectrum confirming their assignment to ^{254}No. A correlation time of 180 s was used (approximately three ^{254}No α-decay half-lives. These transitions have been previously assigned to the ground-state band [Re99, Le99, Re00, Ee05] and for which we provide confirmation. Prominent nobelium K X-rays are labelled and prompt transitions at 842 and 943.5 keV are noted at higher energy. Table 6.2 presents the intensities of the ground-state band transitions recorded corrected for the efficiency of JUROGAM and internal conversion using the relation

$$I_{tot} = \frac{I_{meas}}{\epsilon}\left(1 + \alpha_{tot}\right), \tag{6.5}$$

where I_{meas} is the measured area of the transition, ϵ is the efficiency of JUROGAM and α_{tot} is the internal conversion coefficient.

Tentative observations of ground-state band transitions with energy greater than 500 keV have been made. With this current set of data, identification of these transitions is difficult to make, a more thorough analysis, and confirmation of ground-state band members, can be made by gamma-gamma coincidence analysis.

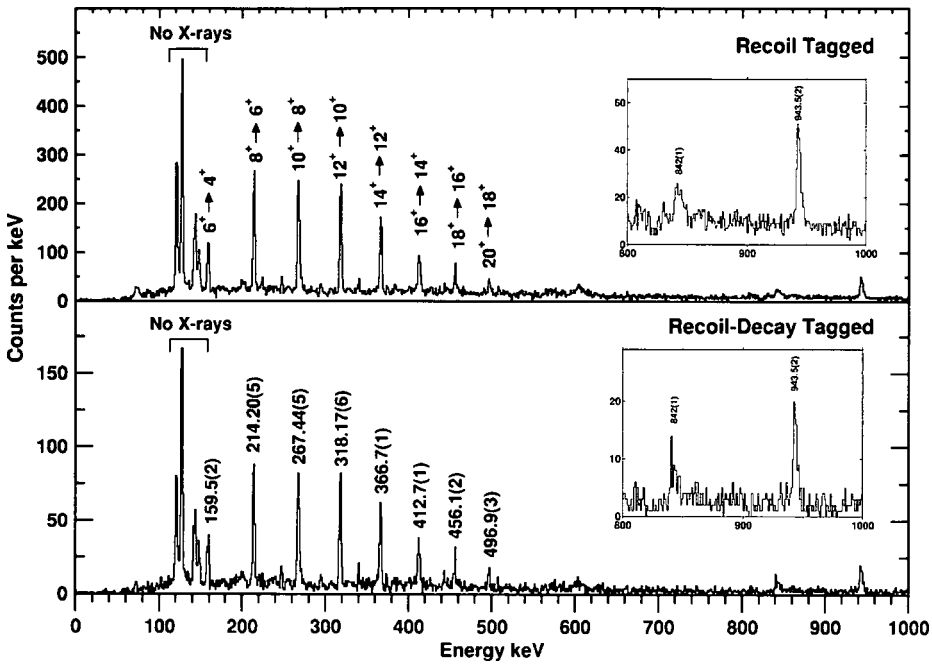

Figure 6.3: Recoil and Recoil-Decay Tagged γ-ray spectra. The ground-state band transitions are labelled with spin and parity in the upper panel and with transition energies in the lower panel.

Transition	E_γ (keV)	I_γ	ICC $E2_{tot}$	$I^\dagger$
$6^+ \rightarrow 4^+$	159.5 *2*	43 *3*	3.94 *6*	138 *10*
$8^+ \rightarrow 6^+$	214.20 *5*	86 *4*	1.202 *17*	123 *5*
$10^+ \rightarrow 8^+$	267.44 *5*	100 *4*	0.534 *8*	100 *4*
$12^+ \rightarrow 10^+$	318.17 *6*	93 *4*	0.300 *5*	79 *3*
$14^+ \rightarrow 12^+$	366.7 *1*	71 *4*	0.195 *3*	56 *3*
$16^+ \rightarrow 14^+$	412.7 *1*	48 *4*	0.1397 *20*	36 *3*
$18^+ \rightarrow 16^+$	456.1 *2*	26 *3*	0.1072 *15*	19 *2*
$20^+ \rightarrow 18^+$	496.9 *3*	23 *3*	0.0865 *13*	17 *2*

Table 6.2: Observed recoil-tagged ground-state band transitions. The intensities I_γ are corrected for the energy dependence of the detection efficiency. The intensities $I^\dagger$ are corrected for the probability of internal conversion using the total E2 ICC taken from reference [ICC]. All intensities are normalised to 100 for the $10^+ \rightarrow 8^+$ transition.

6.3.2 Gamma-gamma coincidence measurements

A gamma-gamma coincidence measurement is used to place transitions in a level scheme. A symmetric gamma-gamma energy matrix is incremented by events detected by JUROGAM which correspond to two or more γ rays in coincidence (Section 4.4.3 details time gate conditions) with a recoil implantation. Figure 6.4 is produced by gating on each member of the ground-state band within the recoil gated gamma-gamma matrix and shows those transitions which are in coincidence with each individual ground state band transition. The spectra are relatively clean with gates of 2-3 keV set encompassing the transition energy. The red lines indicate the positions of the gates and the blue circles represent the transition which is being gated on. The panels also show coincidences for the transitions $22^+ \rightarrow 20^+$ and $24^+ \rightarrow 22^+$. A projection of the sum of the γ-ray spectra from the gamma-gamma coincidence measurement confirms ground-state band transitions at 536 and 570 keV. There is also a suggestion

of a peak at approximately 600 keV, although it is difficult to separate any possible transition from random coincidences in this region.

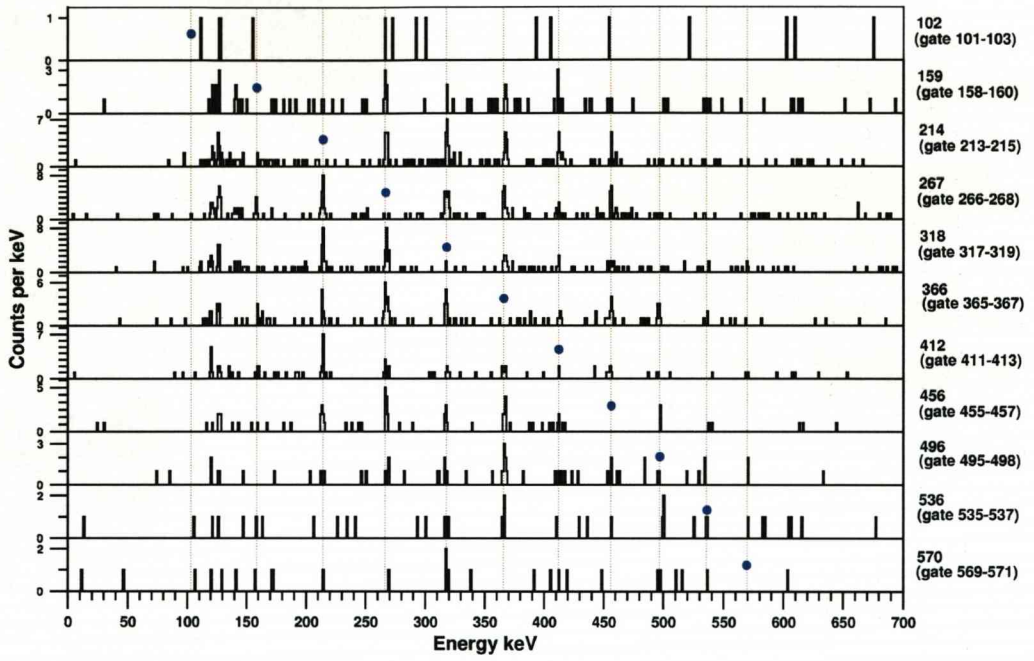

Figure 6.4: Gamma-gamma coincidence measurement. Spectra produced by gating on the ground state band transitions.

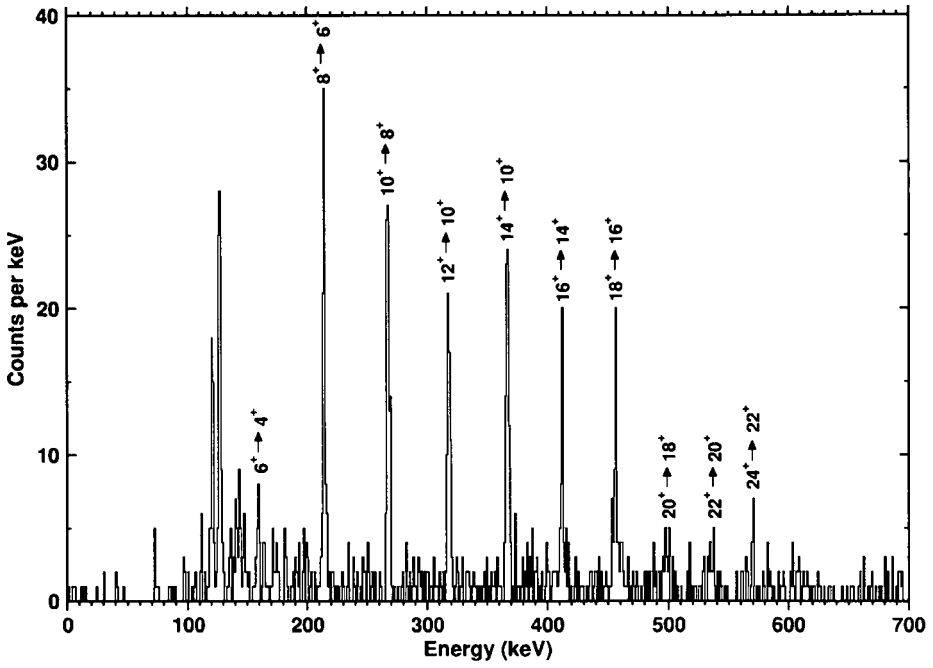

Figure 6.5: Sum of γ-ray spectra projected from the recoil gated gamma-gamma coincidence matrix. The spectrum is composed of spectra gated on ground-state band transitions from the 6^+ state up to the 24^+ state. The transitions $22^+ \rightarrow 20^+$ and $24^+ \rightarrow 22^+$ are identified.

6.3.3 Previously unidentified transitions

A number of low-intensity peaks are ascertained via the recoil-tagged spectrum and a magnification of this spectrum over the area of interest is displayed in Figure 6.6. Marked with energy are a number of peaks which form a regular sequence and due to energy-sum calculations are not believed to be part of the ground-state band. Table 6.3 provides the intensities of these transitions, which we tentatively ascribe to a rotational band, and from these statistics we conclude that the intensity is kept within the band. The ordering of the transitions is on the basis of energies and intensities assuming a rotational band. We also draw from the data that very little intensity is channeled between the band partners as our argument that these are stretched E2 transitions leaves no candidates in our experimental data for M1 transitions.

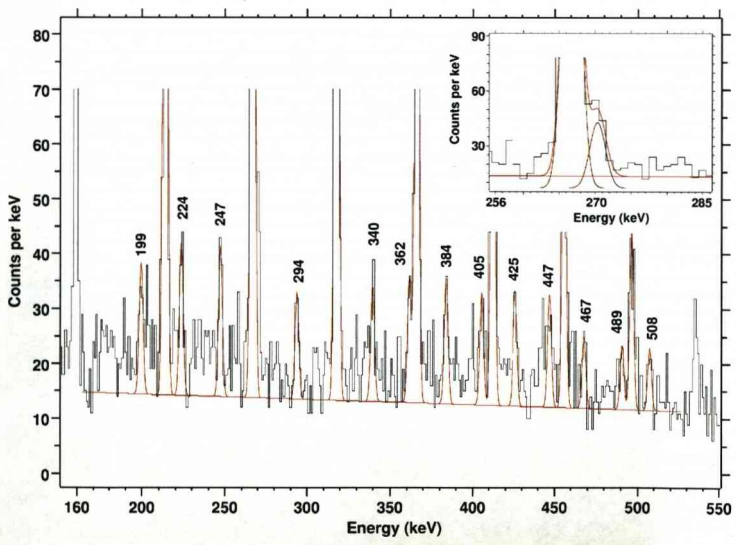

Figure 6.6: Currently unidentified recoil-tagged transitions. The red line shows the fit of peaks and the background is also clarified. The inset shows a possible 270 keV transition concealed within the right-hand tail of the ground state band 267 keV transition, the brown line shows the decomposition of the fit.

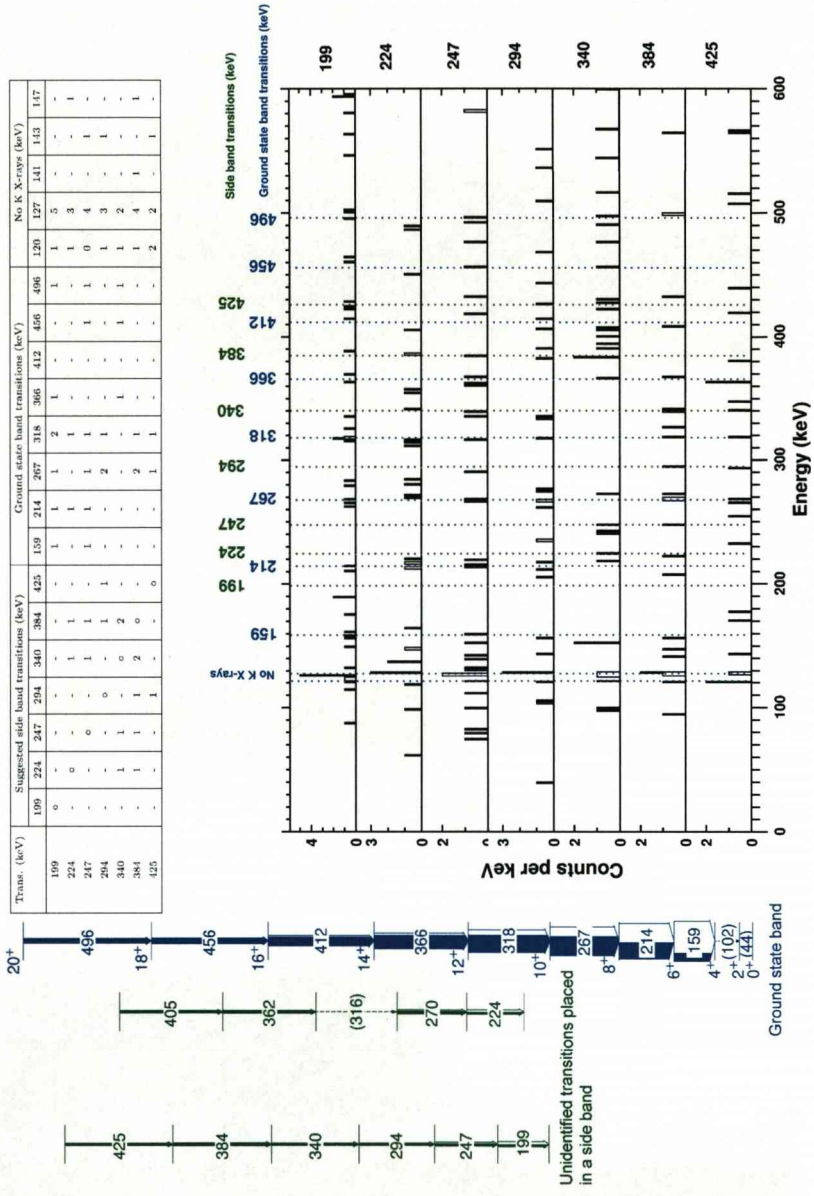

Figure 6.7: Gamma-gamma coincidence measurements. Gates on unidentified recoil-tagged transitions. The table shows the number of coincidences recorded for each transition. A decay scheme is shown for the ground state band (blue) and a proposed side band composed of the unidentified transitions (green), for which spin and parity are unknown. The decay scheme is used to direct the reader and will be discussed in Chapter 7.

Gamma-gamma coincidence measurements, Figure 6.7, show notable coincidences for several of these transitions with K_α X-rays and the most intense K_β X-ray at 143 keV. There are also coincidences with the ground-state band transitions in evidence, linking these newly identified transitions with the ground-state band. Several of the lower energy transitions display coincidences with the lower energy ground state band transitions at 159 and 214 keV. Almost all of the unidentified transitions hold coincidences with ground-state band transitions at 267 and 318 keV. Low statistics only

E_γ (keV)	I_γ	ICC $E2_{tot}$	$I^\dagger$
199 *1*	86 *15*	1.600 *23*	110 *19*
224 *1*	100 *16*	1.014 *15*	100 *16*
247 *1*	99 *15*	0.708 *10*	84 *13*
270 *1*	122 *19*	0.517 *8*	92 *14*
294 *1*	73 *14*	0.388 *6*	50 *10*
340 *1*	84 *15*	0.244 *4*	52 *9*
362 *1*	95 *16*	0.203 *3*	56 *9*
384 *1*	97 *16*	0.1708 *24*	56 *9*
405 *1*	96 *18*	0.1471 *21*	55 *10*
425 *1*	93 *17*	0.1291 *18*	52 *9*
447 *1*	124 *22*	0.1130 *16*	69 *12*
467 *1*	65 *16*	0.1010 *15*	36 *9*
489 *1*	94 *42*	0.0900 *13*	51 *23*
508 *1*	73 *20*	0.0819 *12*	39 *11*

Table 6.3: Currently unidentified recoil-tagged transitions. The intensities I_γ are corrected for the energy dependence of the detection efficiency. The intensities $I^\dagger$ are corrected for the probability of internal conversion using the total E2 ICC taken from reference [ICC]. All intensities are normalised to the 224 keV transition. The absolute intensity of the 199 keV transition in this new band is $\approx$10 % relative to the strongest observed transition in the ground state band.

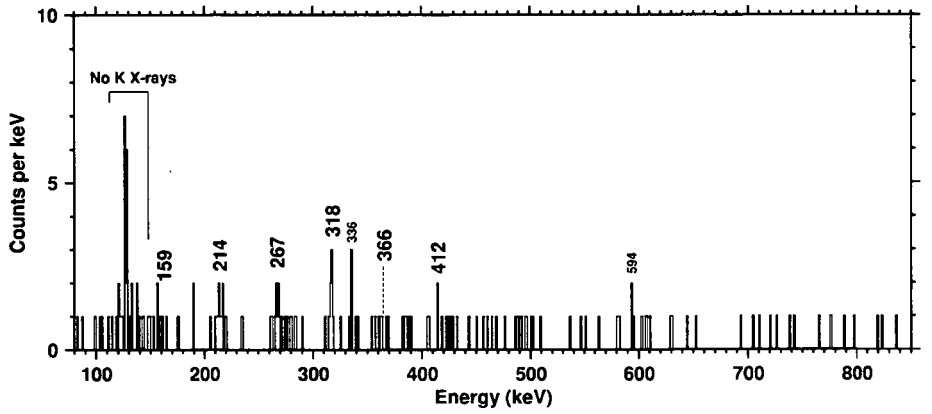

Figure 6.8: Sum of the γ-ray spectra projected from the recoil gated gamma-gamma coincidence matrix (figure 6.7). The spectrum is composed of spectra gated on the unidentified transitions at 199, 224, 247 and 294 keV. Ground-state band transitions are identified and labelled in black and high counts for which no identification can be made in blue.

reveal several single coincidences between the unidentified transitions. Coincidence measurements have not been recorded for unidentified transitions at 270, 316, 362 and 405 keV due to their proximity to ground-state band transitions which would interfere with the coincidence measurements. Figure 6.8 shows the sum of the γ-ray spectra projected from the gamma-gamma coincidence matrix from the gates on the lowest four unobstructed transitions.

We do not observe possible transitions which could link the proposed side band with the ground state band. No possible candidates are revealed in the coincidence measurements and it is feasible that the coincidences could be due to unclean gates or background to background correlations. The unidentified transitions are observed in the recoil-decay tagged spectrum (Figure 6.3) and thus do belong to ^{254}No and are not due to possible target contamination or a different evaporation residue neutron channel.

6.4 Focal plane slow isomer decay spectroscopy results

In this section the results of the slow isomer decay spectroscopy recorded at the focal plane are examined. Data is collected using the calorimetric method outlined in Section 4.4.4. Previous measurements and the definition of a decay scheme for a slow isomer are given in references [Ta06, He06] and presented in Figure 5.9.

6.4.1 Half-life measurement

The time distribution between the recoil implantation in the DSSSD and the decay of the slow isomer is shown in Figure 6.9. The data is fitted with the function

$$N = N_0 \cdot exp(-\lambda t) + c, \tag{6.6}$$

where c accounts for the background events. (We chose not to use a two component fit, similar to that shown in Section 6.2, because the data was flat at higher decay times and could therefore not be calculated with high precision). The correlation time difference is set at 6 s to accommodate the isomer decay. A half-life of 266±2 ms is measured which is in fine agreement with Ghiorso's primary measurement of 240±40 s [Gh73]. The first 50 ms bin is ruled out from the measurement since this channel is also filled with counts recorded for the decay of a fast isomer which is discussed in Section 6.5.1. The inset in Figure 6.9 shows the calorimetric electron signal from the isomer decay recorded in the Y-side of the DSSSD.

6.4.2 Observed decays

A correlation time of 1 ms $\leq t \leq$ 1 s between implanted recoils and detected γ-rays observed in the same position in the DSSSD is set to observe the decay cascade of the 266 ms isomer. The decay spectrum from the de-excitation of the 266-ms isomer followed by prompt electrons is shown in Figure 6.10. Low-energy transitions are observed at 53, 58, 70, 82, 105 and 151 keV and we deduce a decay path according to

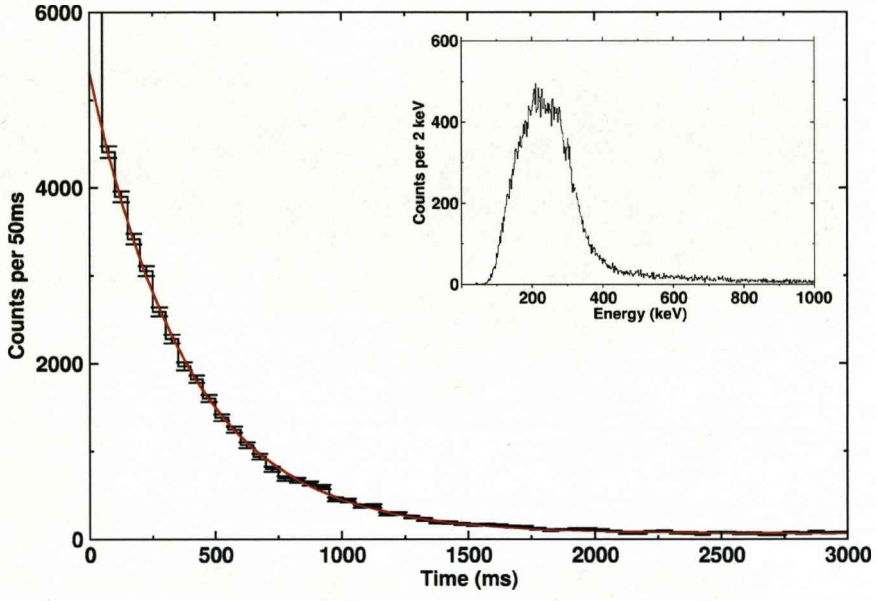

Figure 6.9: The time distribution between the recoil implantation and the decay of the slow isomer. The experimental data are shown in black and the fit is given in red. A half-life of 266±2 ms is measured. The first 50 ms bin is omitted from the measurement since this channel is also filled with counts recorded for the decay of a fast isomer which is discussed in Section 6.5.1.The inset shows the calorimetric electron signal from the isomer decay.

the conformity of the sum of their energies. The high intensity of the 53-keV transition and the low internal conversion leads us to assume that this is of E1 multipolarity and that the 266-ms isomer decays via this transition into a 7^+ rotational band member of a two quasi-particle band (parity and spin of the band head of this band is discussed in Section 6.4.3). The isomer is assigned spin and parity 8^- because no feeding is observed into levels with spin less than or equal to 6. The multipolarities of the transitions identified are shown in Table 6.4.

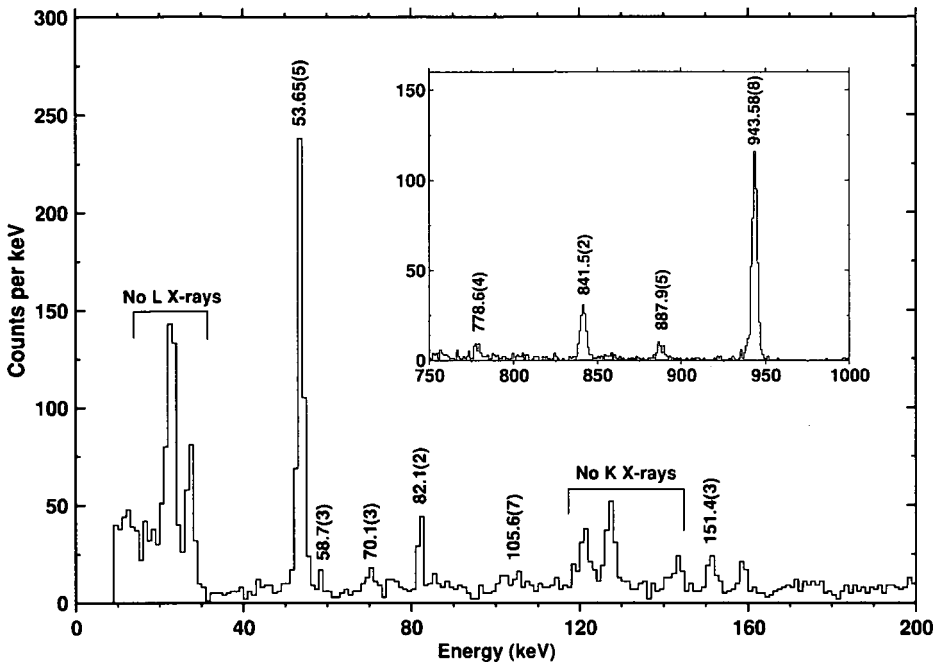

Figure 6.10: Focal-plane isomer decay spectroscopy results. A correlation time of 1 ms $\leq$ $t \leq$ 1 s between implanted recoils and detected γ-rays observed in the same position in the DSSSD is set to observe the decay cascade of the 266 ms isomer.

The suggested 128-keV stretched E2 transition (labelled 126 keV in the intermediate structure of Figure 5.9) is concealed under the 127-keV nobelium K X-ray but it is deduced from the sum of the 70-keV and 58-keV transitions. Simulations conducted for the purpose of obtaining an intensity for this transition have proved inconclusive, the 128-keV transition is expected to have the lowest intensity in the band. Figure 6.12 shows the results of the simulation. Each of the three JYFL data sets were independently simulated using customised efficiency correction data and then combined. Mixing ratios are calculated using the program *BM1BE2* [Pau07] where values of $g_R = 0.402$ and $g_K = 1.006$ were used. Transitions and X-rays are then generated using the program *CALOBRANCH* [He07] which includes input parameters of internal conversion coefficients.

The large error on I_γ of the 53.65-keV transition given in Table 6.4 is due to the

Transition	E_γ (keV)	I_γ	Multipolarity	Internal Conversion Coeff.
$4^+ \rightarrow 3^+$	46.9 *3*	-	E2/M1	201 *3*
$5^+ \rightarrow 4^+$	58.7 *3*	6.4 *13*	E2/M1	87.2 *13*
$6^+ \rightarrow 5^+$	70.1 *3*	8.2 *14*	E2/M1	46.6 *7*
$7^+ \rightarrow 6^+$	82.1 *2*	16.4 *19*	E2/M1	27.4 *4*
$5^+ \rightarrow 3^+$	105.6 *7*	5.3 *14*	E2	24.6 *4*
$6^+ \rightarrow 4^+$	128.8 *4*	≥ 1.9	E2	9.94 *14*
$7^+ \rightarrow 5^+$	151.4 *3*	17.0 *23*	E2	4.92 *7*
$8^- \rightarrow 7^+$	53.65 *5*	100 *500*	E1	0.807 *12*

Table 6.4: $K = 3$ band transitions. The intensities I_γ are corrected for the energy dependence of the detection efficiency. All intensities are normalised to 100 for the 8^- $\rightarrow$ 7^+ transition. The energy and error of the 128.8 keV transition is deduced from the sum of the 70.1 and 58.7 keV transitions. Internal conversion coefficients calculated using reference [ICC].

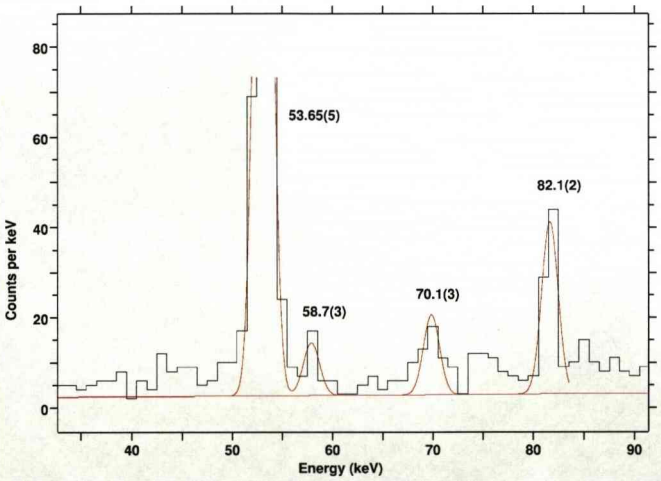

Figure 6.11: Focal-plane isomer decay spectroscopy results in the energy range of 30 - 90 keV. The graphic provides evidence for a transition at 58.7 keV.

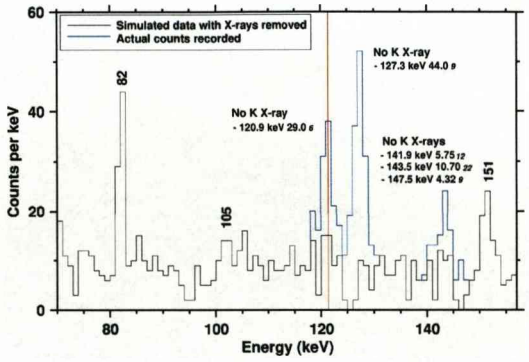

Figure 6.12: Simulated results produced an attempt to reveal possible transitions concealed within the K X-rays. Significant K X-rays are labelled with energy and intensities per 100 K-shell vacancies. Dashed lines represent the X-ray intensities which have been removed to reveal possible transitions. The simulated counts were normalised to the experimental counts in the 1 keV bin at 121 keV.

uncertainty in the measurement of efficiency at this energy using generic simulated efficiency data for the JYFL Ge focal plane detectors [An04]. The efficiency corrections are consistent throughout and the efficiency-corrected intensities are consistent with efficiency-corrected intensities obtained at GSI for the rotational-band transitions. Data taken at GSI is corrected using a specific efficiency model for the SHIP-Clover detector where the 53 keV transition, corrected for efficiency and internal conversion, is consistent with the combined sum of the corrected intensities of the 82 and 151 keV transitions. Several examples of transition intensities recorded at JYFL and GSI are shown in Table 6.6.

6.4.3 High-energy decays

Figure 6.10 also presents the higher-energy prompt transitions which were visible in the recoil-tagged in-beam spectrum (Figure 6.3). From data obtained in the May 2005 experiment the 943.5- and 841.5-keV γ rays were the only prominent high energy transitions recorded. These transitions depopulate the slow isomer and feed into the

Transition	E_γ (keV)	I_γ	Multipolarity	Internal Conversion Coeff.
$3^+ \rightarrow 2^+$	943.58 *8*	100 *4*	M1	0.1069 *15*
$3^+ \rightarrow 4^+$	841.5 *2*	26.6 *22*	M1	0.1459 *21*
$4^+ \rightarrow 4^+$	887.9 *5*	7.6 *13*	(M1)	(0.1261 *18*)
$6^+ \rightarrow 6^+$	857 *1*	2.5 *7*	(M1)	(0.1389 *20*)
$8^- \rightarrow 8^+$	778.6 *4*	4.7 *10*	E1	0.00844 *12*

Table 6.5: Prompt transitions observed in focal plane detectors which link the high-K bands to the ground state band. The intensities I_γ are corrected for the energy dependence of the detection efficiency. All intensities are normalised to 100 for the $3^+ \rightarrow 2^+$ transition. The 857 keV transition is only observed in the GSI SHIP-CLOVER results and therefore we have taken the intensities from that data set, they are consistent with the JYFL results shown in figure 6.10. The multipolarities of the 887 and 857 keV transitions could be mixed, there is no parity change and therefore they could have an M1 or E2 component. The intensities of the 943 and 841 keV transitions and the associated K X-rays (outlined in Section 6.4.3) suggest that these are pure M1 transitions. The absolute efficiency corrected intensity of the E1 53.6 keV transition is 36 % of the 943.5 keV transition. Internal conversion coefficients calculated using reference [ICC].

Transition (keV)	JYFL $I^\dagger$	GSI $I^\dagger$	
151.4 *3*	100 *14*	100 *10*	-
778.6 *4*	23 *6*	17 *3*	consistent
887.9 *5*	37 *8*	31 *5*	consistent

Table 6.6: An example set of slow isomer decay transition intensities obtained at JYFL and GSI. GSI results were obtained from reference [Sul07]. The intensities $I^\dagger$ are corrected for the energy dependence of the detection efficiency and the probability of internal conversion using the total ICC taken from reference [ICC]. All intensities are normalised to 100 for the 151.4 keV transition.

ground-state band. At this point we assign all of the K_α X-rays to the conversion of these two. One hundred K vacancies gives 73 K_α X-rays at energies 120.9 and 127.3 keV [Fi96] and if we assume equal multipolarity for the transitions 943.5 and 841.5 keV, then by using the relationship

$$\alpha_K = \frac{I_K}{0.73 \cdot I_\gamma}, \tag{6.7}$$

where α_K is the K shell internal conversion coefficient, I_K is the efficiency corrected K_α X-ray intensity and I_γ is the efficiency corrected γ-ray intensity, we obtain $\alpha_K = 0.093(10)$ which indicates M1 multipolarity according to Table 6.7. By determining the multipolarity of these transitions which depopulate the band head of the intermediate structure, by feeding the ground-state band at spins 4^+ and 2^+, we can deduce that the band head must have spin 3^+.

The difference in energies between the 943.5 keV and and 841.5 keV transitions allows one to provide a value for the $4^+ \rightarrow 2^+$ ground-state band transition. This transition is highly converted and is not observed in the γ-decay of this nucleus. The difference in energies, taken from Table 6.5, is equal to 102.08±0.22 keV, which is in agreement with the conversion-electron spectroscopic study conducted by Humphreys *et al.* [Hu04] where the $4^+ \rightarrow 2^+$ was measured to be 101.1±0.6 keV.

Multipolarity	α_K (841.5 keV)	α_K (943.5)	Av. α_K
M1	0.1129 *16*	0.0827 *12*	0.0978 *10*
M2	0.230 *4*	0.1691 *24*	0.1996 *23*
M3	0.371 *6*	0.269 *4*	0.320 *4*
E1	0.00588 *9*	0.00486 *7*	0.00537 *6*
E2	0.0181 *3*	0.01496 *21*	0.01653 *18*
E3	0.0412 *6*	0.0335 *5*	0.0374 *4*

Table 6.7: K shell internal conversion coefficients for an array of multipolarities for the transitions 841.5 and 943.5 keV which feed the ground state band from an intermediate $K^\pi = 3^+$ rotational band. Internal conversion coefficients calculated using reference [ICC].

We also record a transition at 887.9 keV (see Figure 6.10) which depopulates the $K^\pi = 3^+$ band at spin 4^+ and feeds the ground-state band at spin 4^+ according to the agreement with the sum of the γ-ray energies.

For the first time we have identified the direct decay from the $K^\pi = 8^-$ isomer to the ground-state band. This 778-keV transition, (see Figure 6.10), was recorded in the sum of the focal-plane Clover spectra observed in prompt coincidence with the slow isomer electron signal. The branching ratio of the direct decay from the 8^- band to the ground state band (gsb) is $I_\gamma(K = 8^- \rightarrow K = 3^+)/I_\gamma(K = 8^- \rightarrow \text{gsb}) = 30\pm7$.

6.4.4 Gamma-gamma coincidence measurements

A gamma-gamma coincidence measurement is shown for the slow isomer decay results in Figure 6.14 (overleaf). The same technique which was used to produce Figure 6.4 was applied. The gamma-gamma matrix of events in the focal plane Ge detectors is sliced for each transition energy. Few points of interest are noted due to the low statistics but the panels are clean with few random coincidences and we point to a number of coincidences with the 53 keV transition. The 53 keV transition is in coincidence with the higher energy transitions at 943 and 841 keV and coincidences are noted with transitions at 82 and 151 keV. Transitions at 70 and 128 keV also show single coincidences with the 943 keV transition. Figure 6.13 displays the sum spectra projected from the gamma-gamma coincidence matrix. Peaks at 53.6 and 943.5 keV are visible.

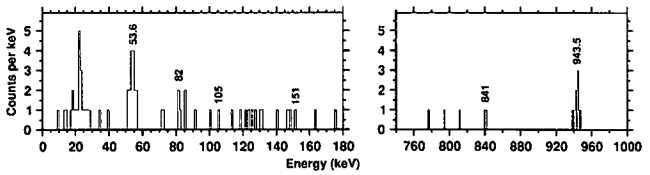

Figure 6.13: The panels show the sum spectra projected from the focal plane isomer decay gamma-gamma coincidence matrix (figure 6.14). Nobelium L X-rays are observed at low energy ($\approx$ 20 keV).

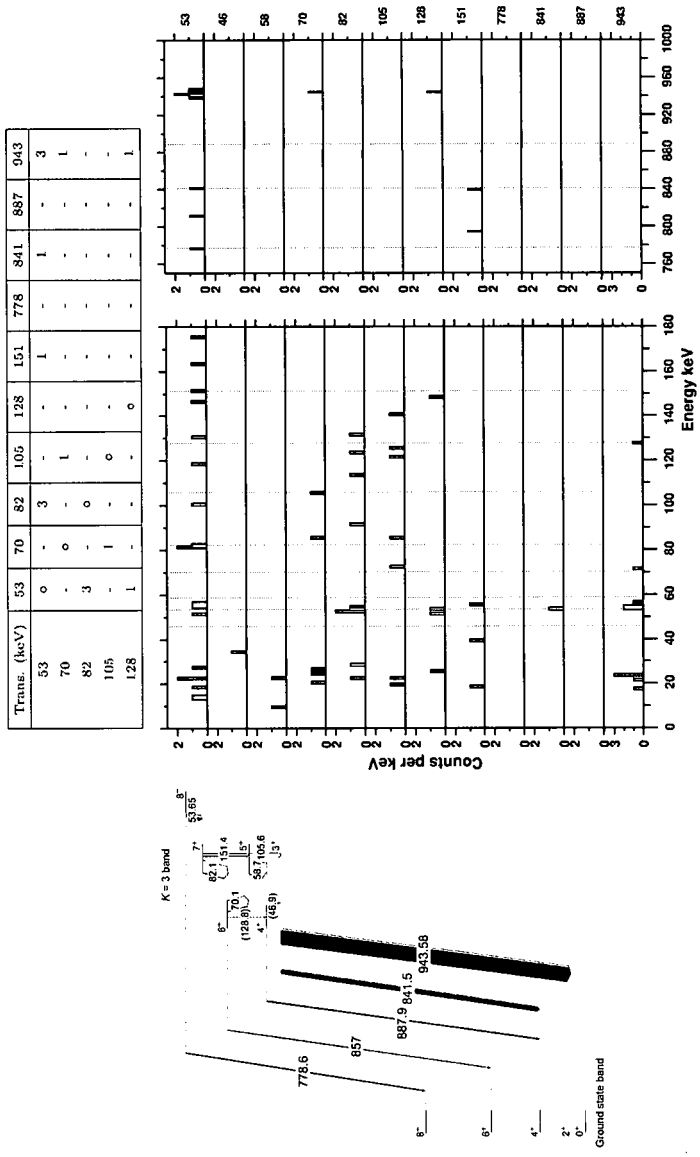

Figure 6.14: Gamma-gamma coincidence measurement for focal plane isomer decay spectroscopy results. Spectra produced by gating on the transitions observed in the focal plane germanium detectors. The red lines indicate the positions of the gates. We do not observe any coincidences with the 778 keV transition. The decay scheme is used to direct the reader and will be discussed in Chapter 7.

6.4.5 Determination of g_K

We can determine whether the $K = 3^+$ structure is built upon proton or neutron excitation from the in-band γ-ray intensity ratios, from which a g_K value is deduced using the relationship for the ratio of reduced transition rates. Simulated branching ratios were generated for two given transitions within the band using the program *BM1BE2* [Pau07] for g_K values in steps of 0.1, where the input parameters included the K value of the band, the collective g-factor g_R, and $Q_0 = 13.3$ eb (this value is approximate to $Q_0 = 13.1$ eb quoted in reference [Re05] and provides a good description of the band when simulated using *BM1BE2* [Pau07]). Two different values of g_R were used when simulating the branching ratio, with the values set at Z/A ($g_R = 0.402$) and $\lambda \cdot Z/A$, where λ represents a quenching factor equal to 0.7 ($g_R = 0.281$). A quenching factor of 0.7 was chosen because this is similar to the factor at which g_R is reduced below Z/A in an area of nuclei which exhibit rotational behaviour displayed in Figure 2.15. This reduction of the core contribution increases the value of g_K of the the predicted proton-proton and neutron-neutron two quasi-particle configurations displayed in Figure 6.15, which shows plots of branching ratios against g_K. Tables 6.9 and 6.10 show the data used to calculate the branching ratios for the suggested two-proton and two-neutron configurations,. where the value R(I) is the ratio of decay intensities I(E2'+M1')/I(E2), calculated using the program *BM1BE2* [Pau07]. The probability of whether a spin state depopulates via an (E2'+M1') or (E2) transition is given, Prob.($I \rightarrow I - 1$) and Prob.($I \rightarrow I - 2$), calculated via $R(I)/\ [1 + R(I)]$

R	R_γ	$R^\dagger$	g_K^{exp} ($g_R = 0.402$)	g_K^{exp} ($g_R = 0.281$)
I_γ(82 keV)/I_γ(151 keV)	0.96 *17*	4.6 *11*	1.03 *7*	0.90 *7*
I_γ(58 keV)/I_γ(105 keV)	1.21 *40*	4.2 *14*	0.73 *7*	0.61 *7*

Table 6.8: $K = 3$ band g_K values calculated from experimental branching ratios where g_R = 0.402 and 0.281. R_γ results are efficiency corrected only and $R^\dagger$ is corrected for internal conversion [ICC].

I	R(I)	Prob.($I \rightarrow I$ - 1)	Prob.($I \rightarrow I$ - 2)	N(I)	N($I \rightarrow I$ - 1)	N($I \rightarrow I$ - 2)
7^+	0.655	0.395	0.604	1000	395.8	604.2
6^+	1.088	0.521	0.478	395.8	206.3	189.5
5^+	2.586	0.721	0.278	810.5	584.5	226.0
4^+	∞	1.0	0.0	774.0	774.0	0

Table 6.9: $K = 3$ band transition intensities predicted for $g_K = 0.908$ (2 proton configuration) and $g_R = 0.402$.

I	R(I)	Prob.($I \rightarrow I$ - 1)	Prob.($I \rightarrow I$ - 2)	N(I)	N($I \rightarrow I$ - 1)	N($I \rightarrow I$ - 2)
7^+	0.119	0.106	0.893	1000	107.0	893.0
6^+	0.199	0.166	0.833	107.0	17.8	89.2
5^+	0.476	0.322	0.677	910.8	294.0	616.7
4^+	∞	1.0	0.0	383.3	383.3	0

Table 6.10: $K = 3$ band transition intensities predicted for $g_K = 0.573$ (2 neutron configuration) and $g_R = 0.402$.

and $1/\,[1 + R(I)]$. The band is initially populated with 1000 counts ($N(I)$) and these counts are fed through the band according to the probabilities.

Using the ratio $R_1 = I_\gamma(82\text{ keV})/I_\gamma(151\text{ keV})$ we determine $g_K^{exp} = 1.03 \pm 0.07$, ratio values are listed in Table 6.8. The 128 keV stretched E2 transition is concealed under the 127 keV nobelium K X-ray and in contrast to reference [He06], it has not been possible to determine the branching ratio $I_\gamma(70\text{ keV})/I_\gamma(128\text{ keV})$. It is possible that since that data set had lower statistics, it would have contained a larger amount of statistical fluctuations, leading the analyst to the interpretation that the 128-keV transition was of a greater intensity. Although an upper limit for the intensity is given in Figure 6.15 using the intensity of the 70-keV transition. However, we can introduce a further γ-ray intensity ratio to that of reference [He06], we now have sufficient statistics to calculate the ratio between the stretched electric quadrupole transition (E2) at 105 keV and the mixed E2/M1 transition at 58 keV, yielding $g_K^{exp} =$

0.73±0.07. The detection efficiency at 58 keV is poorly defined and uncertain and we do note that because of this the ratio calculated is extremely tentative. In addition, the 58-keV transition is observed in the shoulder of a tranistion of greater intensity and thus difficult to resolve and assign an intensity to; the 105-keV transition might contain a degree of intensity from the ground-state band $4^+ \rightarrow 2^+$ transition.

We compare the g_K^{exp} value taken from the ratio $I_\gamma(70\text{ keV})/I_\gamma(128\text{ keV})$ with values given by Herzberg, $g_K^{exp} = 0.87\pm0.14$ [He06] for the band, and the γ-ray intensity ratio, $I_\gamma(151\text{ keV})/I_\gamma(82\text{ keV}) = 1.1\pm0.4$, given by Tandel [Ta06].

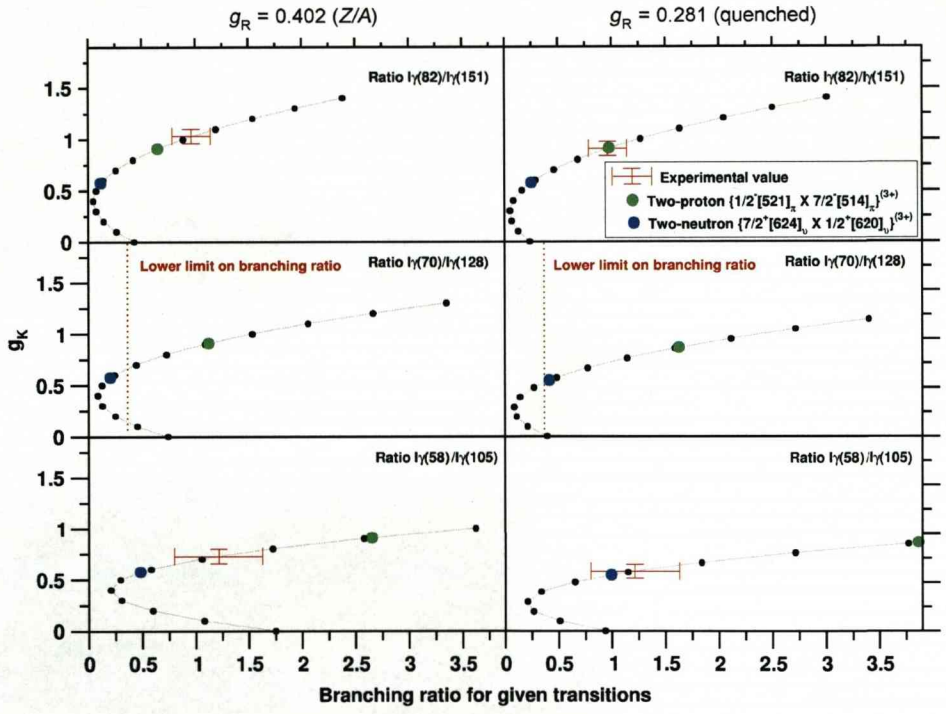

Figure 6.15: Experimental branching ratios used to determine a g_K value for the $K^\pi = 3^+$ band. A lower limit on the ratio $I_\gamma(70\text{ keV})/I_\gamma(128\text{ keV})$ is given where the 128 keV transition is concealed under the 127 keV K X-ray. Predicted two-proton and two-neutron configurations are displayed. Two plots are shown for each branching ratio to accommodate two different values of g_R, with the values set at Z/A ($g_R = 0.402$) and $\lambda \cdot Z/A$, where λ represents a quenching factor equal to 0.7 ($g_R = 0.281$).

6.5 In-beam recoil-isomer tagging and fast isomer decay results

A short-lived isomer has previously been identified and it is expected that this isomer decays into a rotational band built on top of the 266-ms isomeric $K^{\pi} = 8^{-}$ state [He06, Ta06].

6.5.1 Half-life measurement

The time distribution between the implanted ^{254}No nucleus and the isomeric electron signal in the same pixel of the DSSSD is shown for the first 3 ms after implantation in Figure 6.16. The bin counts were fitted using the same approach to that used when calculating the half-life of the 266 ms isomer. The half-life of this shorter-lived isomer was found to be 184±2 μs. We note that the end-point of the calorimetric electron signal extends further in energy than the signal given for the slow isomer.

6.5.2 Observed decays

The results of the focal plane fast isomer decay spectroscopy (performed at both JYFL and GSI) and in-beam experiments (performed at JYFL) are shown in Figure 6.17. The focal-plane decay spectra result from evaporation residue-$\gamma(e^{-})$ coincidences within 1 ms after the implantation of the evaporation residue. The in-beam spectrum results from the recoil-isomer tagging technique, where the prompt γ-rays observed in JUROGAM are associated with the recoils selected in Section 6.4, and are then thus assigned as transitions built on top of the isomeric state. The in-beam results provide validity to the placement of the transitions feeding the slow isomer shown in the focal plane spectrum. Transitions at 111, 134, 157, 168 and 179 keV are tentatively classified as mixed (E2+M1) transitions within a two quasi-particle band. This is upheld by the identification of transitions at 257, 302, 325 and 347 keV from GSI results, which are tentatively assigned as stretched E2 transitions due to the agreement with γ-ray sum differences.

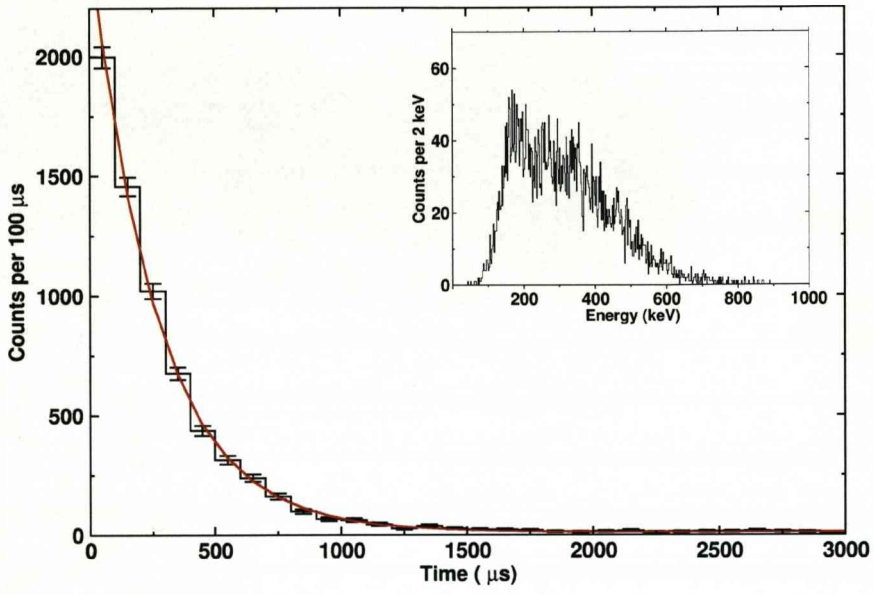

Figure 6.16: The time distribution between the recoil implantation and the decay of the fast isomer. The experimental data are shown in black and the fit is given in red. A half-life of 184±2 μs is recorded. The inset shows the calorimetric electron signal from the isomer decay.

Focal plane statistics from JYFL only provided evidence of M1 transitions within the $K^{\pi} = 8^{-}$ band, with no evidence of stretched E2 transitions (discussed later). The transitions at 111, 134, 157, 179 and 605 keV were all identified in the JYFL focal-plane detector results.

A possible mixed (M1+E2) 145-keV transition is believed to lie under several K_{β} X-rays. These X-rays, with energies of $K_{\beta 1} = 143.5$ keV, $K_{\beta 2} = 147.5$ keV and $K_{\beta 3} = 141.9$ keV, and intensities of 10.7, 4.3 and 5.7 per 100 K-shell vacancies, are hard to resolve and makes a confirmation, or certainly an estimate of the intensity, a difficult task. However, when we simulate the K X-ray intensities by applying the

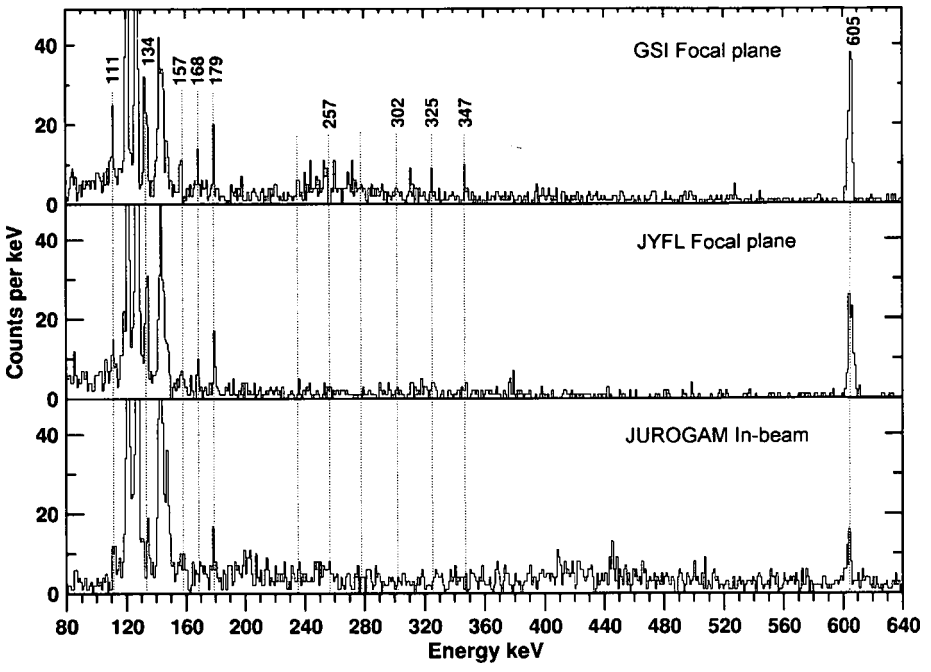

Figure 6.17: Top panel, GSI focal plane $K = 8$ band spectrum, resulting from coincidences with evaporation residues with γ-rays in prompt coincidence with electrons within 1 ms after implantation of ^{254}No nuclei. Centre, JYFL focal-plane results with the same specifications set for the GSI results. Bottom panel, in-beam recoil-isomer tagged spectrum, $K = 8$ band. Nobelium K X-rays dominate at 120, 127, 141, 143 and 147 keV.

same method used in Section 6.4.2, using mixing ratios corresponding to $g_K^{\pi\pi} = 1.006$ (similar mixing ratios are calculated for neutron-neutron configurations, Table 6.12) and remove them from the experimental spectrum (Figure 6.18), counts at 145 keV are observed and we tentatively assign them to this forecasted (M1+E2) transition. Evidence for a mixed (M1+E2) 123-keV transition embedded under the 120.9-keV $K_{\alpha 2}$ X-ray is also forthcoming, simulated K X-ray counts removed from the experimental spectrum indicate a transition at this energy. We do not use these intensities to make any conclusions on configurations.

Since the 605-keV transition is observed in the in-beam recoil isomer tagged re-

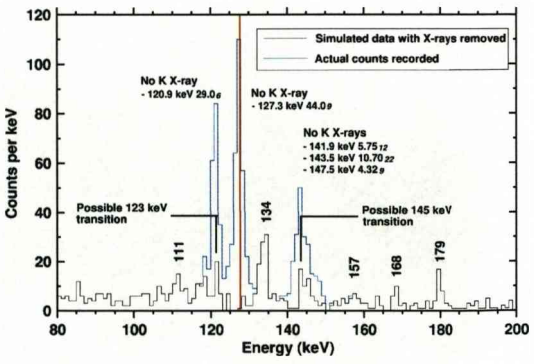

Figure 6.18: Simulated results produced in an attempt to reveal possible transitions concealed within the K X-rays. Significant K X-rays are labelled with energy and intensities per 100 K-shell vacancies. Dashed lines represent the X-ray intensities which have been removed to reveal possible transitions. The simulated counts were normalised to the experimental counts in the 1 keV bin at 127 keV.

sults, and is therefore prompt, we conclude that this transition does not directly depopulate the 184 μs isomer.

Figure 6.19 overlays the detector efficiencies on the spectra which are combined and/or used in Figure 6.17. It is unclear why we observe transitions at 325 and 347 keV for example in GSI data and not in the combined JYFL data, even though lower energy transitions (at 179 keV for example) are of a similar intensity. The fall in detector efficiency at higher energy is similar for each of the data sets and gives no indication as to why the higher energy transitions are visible only in the GSI data. The discrepancy could be due to differences in trigger periods. The data collection at JYFL is cleaner. It is unclear whether the differences are due to a physical or a statistical reason.

Transition	E_γ (keV)	Focal Plane I_γ	In-beam I_γ	Multipolarity	ICC
$9^- \rightarrow 8^-$	111.6 *8*	68 *11*	90 *18*	E2/M1	10.21 *15*
$10^- \rightarrow 9^-$	123 *1*	-	-	E2/M1	7.45 *11*
$11^- \rightarrow 10^-$	134 *1*	100 *13*	100 *16*	E2/M1	5.74 *8*
$12^- \rightarrow 11^-$	145 *1*	-	-	E2/M1	4.53 *7*
$13^- \rightarrow 12^-$	157 *1*	24 *6*	33 *10*	E2/M1	14.57 *21*
$14^- \rightarrow 13^-$	168.3 *7*	30 *6*	37 *11*	E2/M1	12.04 *17*
$15^- \rightarrow 14^-$	179.7 *7*	38 *7*	61 *13*	E2/M1	10.06 *14*
$10^- \rightarrow 8^-$	234 *1*	-	-	E2	0.862 *12*
$11^- \rightarrow 9^-$	257 *1*	-	-	E2	0.614 *9*
$12^- \rightarrow 10^-$	279 *1*	-	-	E2	0.462 *7*
$13^- \rightarrow 11^-$	302 *1*	15 *6*	-	E2	0.355 *5*
$14^- \rightarrow 12^-$	325 *1*	24 *8*	-	E2	0.281 *4*
$15^- \rightarrow 14^-$	347 *1*	28 *9*	-	E2	0.230 *4*
$16^+ \rightarrow 15^-$	605.6 *2*	600 *50*	144 *22*	M1	0.276 *4*

Table 6.11: $K = 8$ band transitions. The intensities I_γ are corrected for the energy dependence of the detection efficiency. All intensities are normalised to 100 for the $11^- \rightarrow 10^-$ transition. Internal conversion coefficients calculated using reference [ICC].

g_K	E_γ ($I \rightarrow I$-2)	E_γ ($I \rightarrow I$-1)	δ
$\pi\pi$ 1.006	348.0	179.7	0.246
$\upsilon\upsilon$ −0.021	348.0	179.7	0.218

Table 6.12: Mixing ratios calculated using program *BM1BE2* [Pau07].

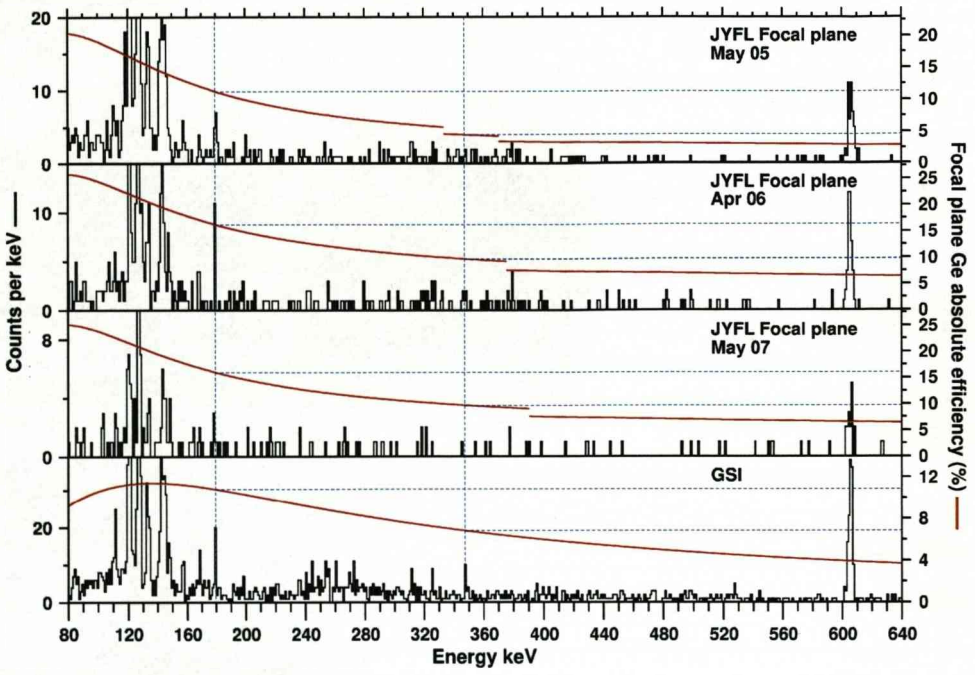

Figure 6.19: Detector efficiencies for each experimental setup overlaid on to the focal plane data displayed in Figure 6.17.

6.5.3 Multipolarity of the 605 keV transition

From the individual results obtained from the JYFL May 2005, April 2006 and GSI focal-plane fast-isomer decay data sets we shall propose a multipolarity for the 605-keV transition. The same approach was used to that discussed in Section 6.4.3. The number of K_α X-rays generated by the 157-, 168- and 179-keV transitions (and the 257-, 302-, 325- and 347-keV transitions observed in the GSI data set) are calculated using reference [ICC] and are then subtracted from the number of K_α X-rays observed. We assign the remaining number of K_α X-rays to that of the 605 keV transition in order to calculate the internal conversion coefficient α_K. Results are displayed in Table 6.13 and we note that these point favourably towards M1 multipolarity. How-

ever, conversion coefficients having values of between 0 and 0.57 are consistent with the data, and therefore the assignment is tentative. A list of α_K internal conversion coefficients for a number of multipolarities are displayed in Table 6.14.

Experiment	N_K (E2'+M1') & E2	N_K observed	N_γ 605 keV	α_K
JYFL May 2005	1380 *350*	1630 *110*	1340 *220*	0.26 *37*
JYFL Apr 2006	510 *120*	570 *50*	650 *100*	0.14 *27*
GSI	3320 *480*	3900 *200*	2660 *270*	0.30 *31*

Table 6.13: Results used to calculate the multipolarity of 605 keV transition. Column N_K (E2'+M1') & E2 is the number of X-rays generated by the (E2'+M1') & E2 transitions, N_K observed is the number of K_α X-rays observed, N_γ 605 keV is the number of counts recorded for the 605 keV transition and α_K is the internal conversion coefficient calculated using Equation 6.7.

Multipolarity	α_K (605.6 keV)
M1	0.276 *4*
M2	0.572 *8*
M3	1.576 *22*
M4	1.646 *23*
E1	0.01033 *15*
E2	0.0307 *5*
E3	0.0738 *11*
E4	0.1555 *22*

Table 6.14: K-shell internal conversion coefficients for an array of multipolarities for the transition 605 keV identified in the $K^\pi = 8^-$ rotational band, internal conversion coefficients calculated using reference [ICC].

6.5.4 Gamma-gamma coincidence measurements

Gamma-gamma coincidences are a rarity in the recorded events in the Ge detectors at the focal plane when the correlation times are set to observe decays in the $K^{\pi} = 8^{-}$ band. Figure 6.20 shows coincidences when gates are set on the two most intense peaks at 134 keV and 605 keV of the JYFL focal plane results. The low background recorded in the two panels gives assurance to the single-count coincidences observed. Each gate results in coincidences with K X-rays and a stretched E2 transition at 302 keV is observed in coincidence with 134 keV.

A gamma-gamma coincidence measurement was performed for the same transitions in reference [Sul07] using GSI focal plane results. Coincidences with a 133-keV transition were observed at 168 keV, 179 keV and with No K X-rays. There are a greater number of random coincidence counts in these measurements than what we observe in Figure 6.20.

No information can be drawn from gamma-gamma coincidence measurements taken from the recoil-isomer tagged in-beam data. A lower number of statistics for transitions and a greater background count were observed for the band using this method of data collection.

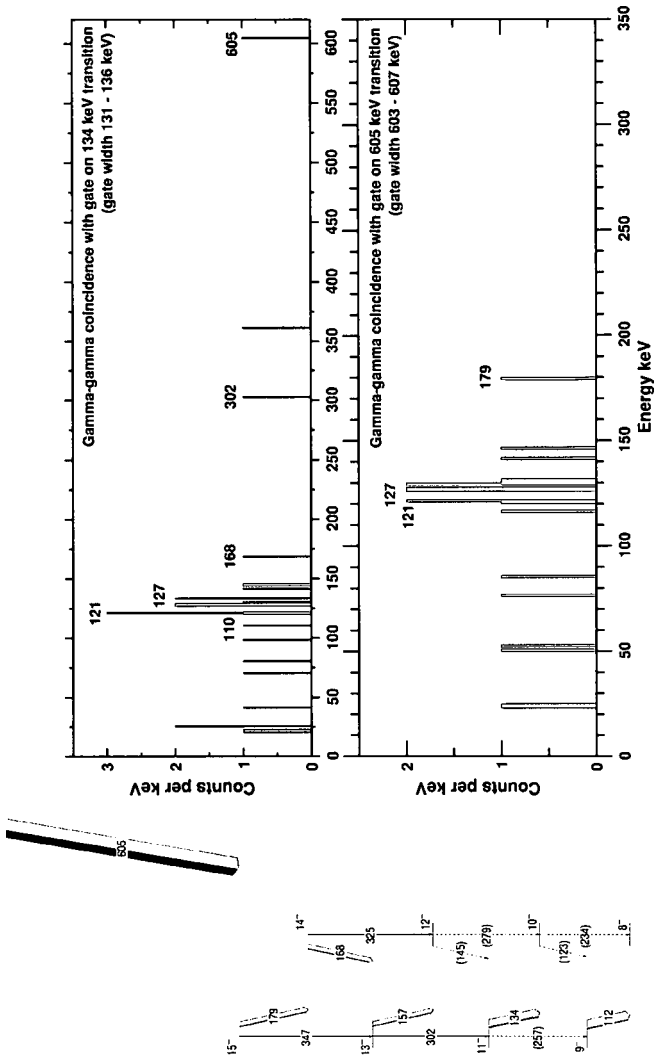

Figure 6.20: Gamma-gamma coincidence measurements for the $K = 8$ band using focal plane Ge detectors at JYFL.

6.5.5 Determination of g_K

Determination of g_K for the $K^\pi = 8^-$ band is performed using the same method applied to the calculation of g_K for the $K^\pi = 3^+$ band in Section 6.4.5.

Focal-plane data obtained at GSI has resulted in the identification of the stretched E2 transitions in the $K = 8$ band, Figure 6.17, and therefore from the intensities of both the M1 and E2 transitions we can deduce a branching ratio and hence a value of g_K and compare to theoretical values. Gamma-ray intensity ratios $R_1 = I_\gamma(179\text{ keV})/I_\gamma(348\text{ keV})$, $R_2 = I_\gamma(168\text{ keV})/I_\gamma(325\text{ keV})$ and $R_3 = I_\gamma(157\text{ keV})/I_\gamma(302\text{ keV})$ have been found, Table 6.18, and are overlaid onto Figure 6.21, where branching ratios have been calculated for values of g_K in increments of 0.1. Theoretical calculations of g_K for the predicted 8^- two quasi-particle configurations lie on either arm of the plot and so therefore the experimentally determined branching ratios are also given on both arms. For completeness, we have performed calculations using $g_R = Z/A$ and $0.7(Z/A)$ which is discussed in Section 6.4.5. Tables 6.15, 6.16 and 6.17 show the data used to calculate the branching ratios for the suggested two-proton and the two two-neutron configurations, where the value R(I) is the ratio of decay intensities I(E2'+M1')/I(E2), calculated using the program *BM1BE2* [Pau07]. The probability of whether a spin state depopulates via an (E2'+M1') or (E2) transition

I	R(I)	Prob.($I \rightarrow I$ - 1)	Prob.($I \rightarrow I$ - 2)	N(I)	N($I \rightarrow I$ - 1)	N($I \rightarrow I$ - 2)
15^-	1.129	0.530	0.469	1000	530.5	469.4
14^-	1.411	0.585	0.414	530.5	310.6	219.9
13^-	1.853	0.649	0.350	780.1	506.7	273.3
12^-	2.593	0.721	0.278	726.7	524.5	202.2
11^-	4.069	0.802	0.197	797.8	640.4	157.4
10^-	8.533	0.895	0.104	842.6	754.2	88.4
9^-	∞	1.0	0.0	911.6	911.6	0

Table 6.15: $K = 8$ band transition intensities predicted for $g_K^{\pi\pi} = 1.006$ $(\{7/2^-[514]_\pi \otimes 9/2^+[624]_\pi\}^{(8-)})$.

I	R(I)	Prob.($I \rightarrow I$ - 1)	Prob.($I \rightarrow I$ - 2)	N(I)	N($I \rightarrow I$ - 1)	N($I \rightarrow I$ - 2)
15^-	0.587	0.369	0.630	1000	369.9	630.1
14^-	0.733	0.423	0.576	369.9	156.6	213.3
13^-	0.964	0.490	0.509	786.7	386.1	400.5
12^-	1.349	0.574	0.425	599.5	344.3	255.1
11^-	2.118	0.679	0.320	744.9	506.0	238.8
10^-	4.446	0.816	0.183	761.2	621.4	139.7
9^-	∞	1.0	0.0	860.3	860.3	0

Table 6.16: $K = 8$ band transition intensities predicted for $g_K^{\upsilon\upsilon}$ = -0.021 ($\{7/2^+[624]_\upsilon \otimes 9/2^-[734]_\upsilon\}^{(8-)}$).

I	R(I)	Prob.($I \rightarrow I$ - 1)	Prob.($I \rightarrow I$ - 2)	N(I)	N($I \rightarrow I$ - 1)	N($I \rightarrow I$ - 2)
15^-	1.418	0.586	0.413	1000	586.6	413.4
14^-	1.772	0.639	0.360	586.6	375.0	211.5
13^-	2.327	0.699	0.300	788.5	551.5	236.9
12^-	3.256	0.765	0.234	763.0	583.7	179.2
11^-	5.108	0.836	0.163	820.7	686.4	134.4
10^-	10.708	0.914	0.085	856.6	791.7	73.9
9^-	∞	1.0	0.0	926.1	926.1	0

Table 6.17: $K = 8$ band transition intensities predicted for $g_K^{\upsilon\upsilon}$ = -0.279 ($\{7/2^+[613]_\upsilon \otimes 9/2^-[734]_\upsilon\}^{(8-)}$).

is given, Prob.$(I \rightarrow I-1)$ and Prob.$(I \rightarrow I-2)$, calculated via $R(I)/\ [1+R(I)]$ and $1/\ [1+R(I)]$. The band is initially populated with 1000 counts ($N(I)$) and these counts are fed through the band according to the probabilities.

Calculations of the available branching ratios result in a best estimate and accuracy of $g_K^{exp} = 1.00 \pm 0.08$ if one considers the upper-arm of the plot of branching ratio versus g_K, Figure 6.21, and if we consider the lower-arm, where the two neutron-neutron configurations predicted from theory lie, we calculate a best estimate and accuracy of g_K^{exp} = -0.20±0.01. All results are presented in Table 6.18.

R	R_γ	$R^\dagger$	$g_K^{exp\ upper\ value}$	$g_K^{exp\ lower\ value}$
$I_\gamma(179\ keV)/I_\gamma(347\ keV)$	1.4 *5*	12 *5*	1.07 *14*	-0.27 *2*
$I_\gamma(168\ keV)/I_\gamma(325\ keV)$	1.3 *5*	16 *6*	0.97 *13*	-0.16 *2*
$I_\gamma(157\ keV)/I_\gamma(302\ keV)$	1.6 *8*	18 *9*	0.96 *15*	-0.15 *3*

Table 6.18: $K = 8$ band g_K values calculated from experimental branching ratios where $g_R = 0.402$. R_γ results are efficiency corrected only and $R^\dagger$ results are corrected for internal conversion [ICC].

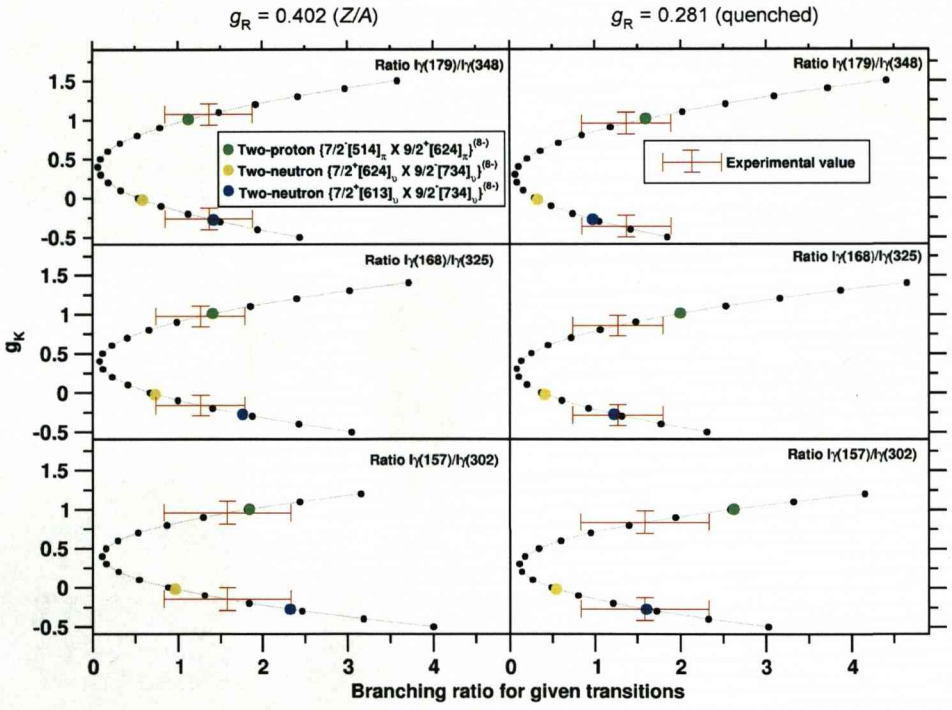

Figure 6.21: Experimental results from GSI used to determine a g_K value for the $K = 8$ band. Predicted two-proton and two-neutron configurations are displayed. Two plots are shown for each branching ratio to accommodate two different values of g_R, with the values set at Z/A ($g_R = 0.402$) and $\lambda \cdot Z/A$, where λ represents a quenching factor equal to 0.7 ($g_R = 0.281$).

Chapter 7

Discussion of Results

7.1 Discussion of the in-beam recoil tagged results

7.1.1 The ground-state band

The results outlined in Section 6.3 conform to the previous statements that the ^{254}No nucleus is deformed, established via the identification of a rotational band.

The $2^+ \rightarrow 0^+$ transition is not observed in the recoil-tagged spectra due to the high internal conversion. The deduced energy of the ground-state band $4^+ \rightarrow 2^+$ transition in Section 6.4.3 allows for a more precise extraction of the $2^+ \rightarrow 0^+$ energy than what has been previously measured (44±1 keV [Re99, Ee06]) using a Harris fit [Ha65]. The Harris fits use higher-order corrections to the cranking model to obtain the following equations:

$$\Im^{(1)} = J_0 + J_1\omega^2, \tag{7.1}$$

$$\Im^{(2)} = J_0 + 3J_1\omega^2, \tag{7.2}$$

where $\Im^{(1)}$ and $\Im^{(2)}$ are the kinematic and dynamic moments of inertia, ω is the rotational frequency and J_0 and J_1 are Harris parameters. Figure 7.1 shows the Harris fits applied to the ^{254}No data which result in Harris parameters of $J_0 = (68.16\pm0.04)$

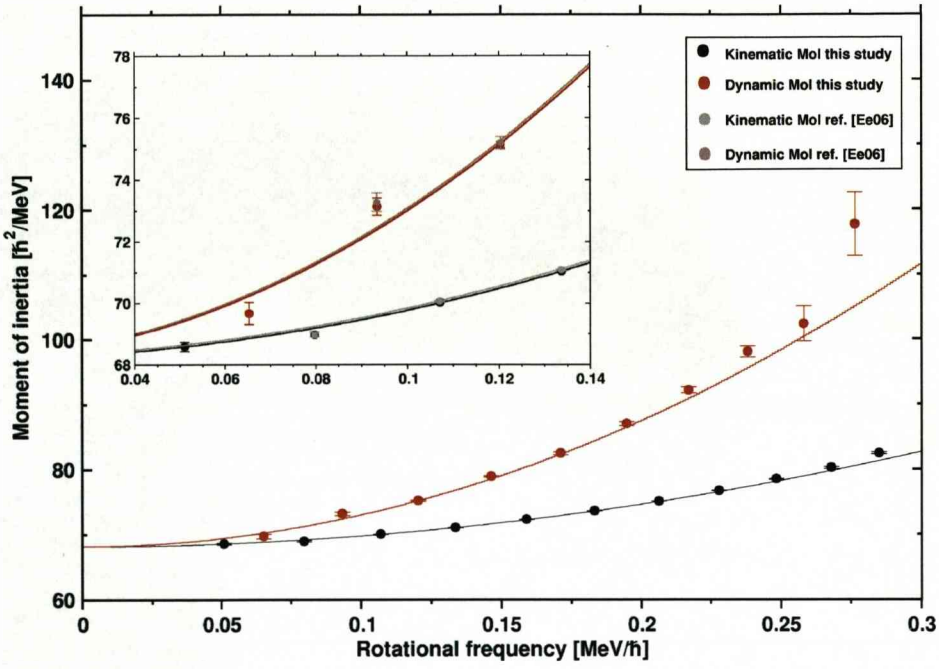

Figure 7.1: Harris fits applied to the kinematic and dynamic moments of inertia (MoI). The inset shows a comparison with data used in reference [Ee06] where the energy of the $4^+ \rightarrow 2^+$ transition was not used.

$\hbar^2\text{MeV}^{-1}$ and $J_1 = (161.3\pm2.3)\ \hbar^2\text{MeV}^{-3}$. Using the expression

$$I_x = J_0\omega + J_1\omega^3 + \frac{1}{2}, \tag{7.3}$$

we calculate the rotational frequency ω at spin-2 to be 0.02198±0.00002. The $2^+ \rightarrow 0^+$ transition energy is simply twice the rotational frequency. However, given the statistics observed it is unlikely that the fit error from the extrapolation procedure is the dominant error and we therefore increase it to be in line with the statistical uncertainties of the lowest energy transitions in the band. Hence, we determine the $2^+ \rightarrow 0^+$ transition energy to be (44.0±0.3) keV. The first four data points from the kinematic moment of inertia calculations and the first three points of the dynamic moment of inertia calculations are used for the calculation since the nuclear moment of inertia is roughly proportional to the rotational frequency at low spin.

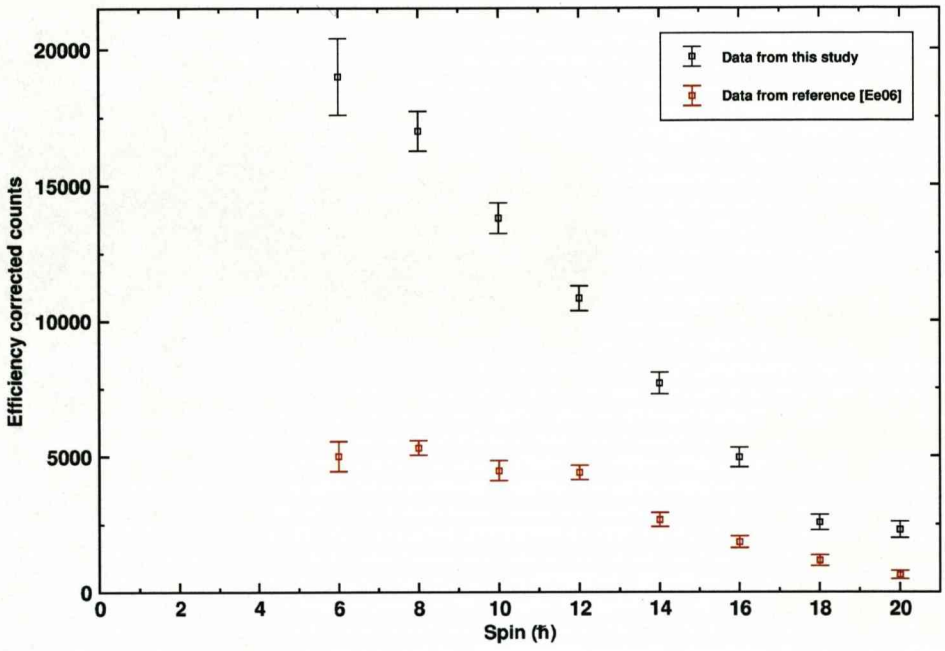

Figure 7.2: A plot of ground state band transition intensities as a function of spin. The intensities are corrected for detection efficiency and internal conversion (Table 6.2).

Figure 7.2 displays a plot of the ground-state band E2-transition intensities (corrected for detection efficiency and for internal conversion) as a function of spin. A similar plot is given in reference [Ee06] for a lower number of statistics and where an argument is put forward that the feeding of this band is mainly situated between spin 10 $\hbar$ to 20 $\hbar$ since a levelling off of intensity is observed at $\leq$ 10 $\hbar$. However, in contrast to reference [Ee06], Figure 7.2 shows that feeding appears to be continuous from spin 6 $\hbar$ to 18 $\hbar$ and that there is no move towards a stability of feeding within this spin region. The figure displays a dramatic difference in feeding patterns and one must question the efficiency used to correct the transition intensities at low energy.

7.1.2 Side band

Figure 7.3 shows the transitions identified in Section 6.3.3. Several important points should be made. The transition at 316 keV is tentatively assigned because any identification is obscured by the ground-state band 318-keV transition. We determine that the 199 keV transition feeds the band head because no further transitions are observed. If we continue the trend in the difference in energy between transitions as

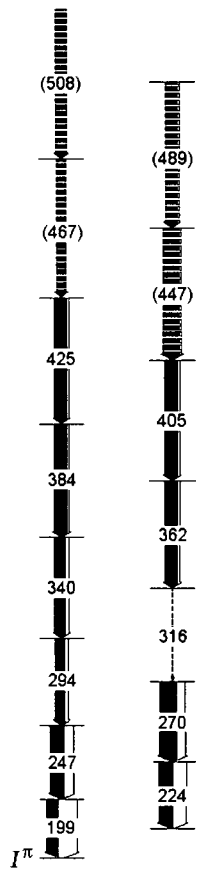

Figure 7.3: Placement of unidentified in-beam recoil decay tagged transitions within a side band. A spin assignment is made but this is extremely tentative. The transition at 316 keV is provisionally assigned because any identification is obscured by the ground-state band 318 keV transition.

spin decreases then we would expect transitions of approximately 177 keV and 151 keV to precede transitions 224 keV and 199 keV.

Unidentified transitions within a similar energy range are also observed in the recoil-tagged spectra of ^{250}Fm. However, statistics for these transitions are low and do not permit a placement within the level scheme [Ba06].

No provisional assignment of spin was made to the energy levels of the band but calculations of the kinematic moment of inertia were made for several band head spins, shown in Figure 7.4. The data points of a $K = 6$ band are positioned so that they lie flush with the ground-state band and data points of the $K = 5$ and $K = 4$

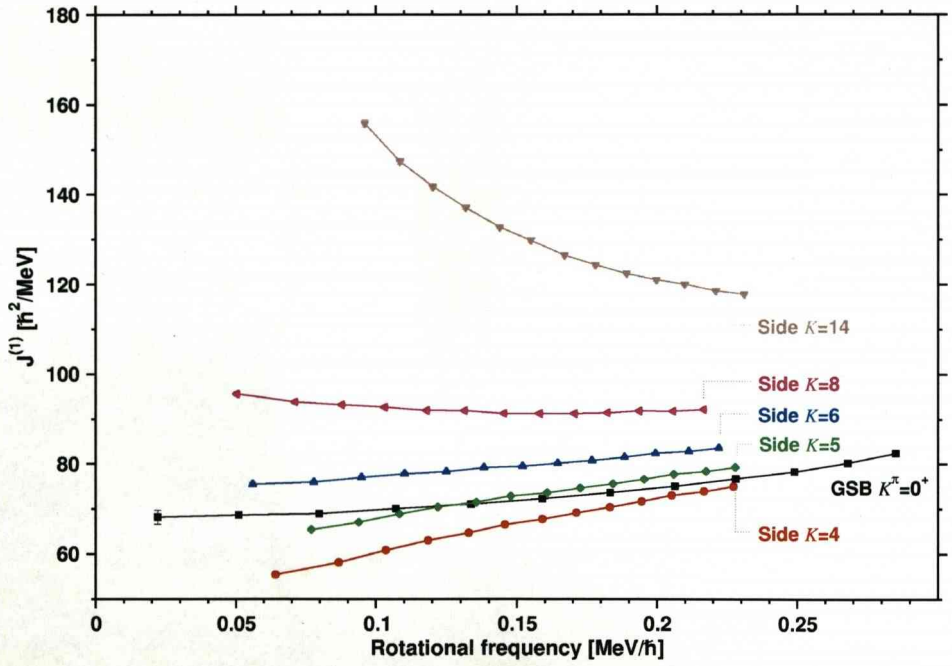

Figure 7.4: Kinematic moment of inertia plots for a proposed side band for different values of K. The ground state band is shown for completeness.

kinematic moment of inertia calculations cut through or lie below the ground state band.

Under this premise we have calculated the energies of several 2-quasiparticle K = 4, 5, 6 and 7 states, Table 7.1. The calculations of the 2-quasiparticle states are based on a Woods-Saxon potential using the "Universal" parameterisation (the program SWBETA is used to perform the calculations [Ćw87]). A Lipkin-Nogami treatment for the pair gap parameters Δ_p and Δ_n is used, and values are obtained from reference [Mö97] and quenched by 0.6. The quenching provides a good agreement with experimental 2-quasiparticle energy values obtained for the $K^\pi = 3^+$ and $K^\pi = 8^-$ states [Gr08]. No subtraction of a residual spin-spin interaction energy (approximately 100 keV [Ta06]) from the excitation energy is made in these calculations.

There is a wide range of possible K = 4, 5, 6 and 7 excitation energies thus making it difficult to underpin where the band lies in terms of excitation energy and how it feeds into the ground state band. We have omitted configurations for which the excitation energy is greater than 2 MeV and for completeness Table 7.1 also provides the g_K values for the suggested configurations (calculated for individual orbitals using the program SWBETA [Ćw87] and combined using Equation 2.66). Since we only observe E2 transitions and no M1 transitions this suggests that the value of g_K must be positive with a magnitude of $g_K \approx g_R$ (hence the intensity of the M1 transition tends to zero). There are several configurations for which this is true, notably $\{1/2^-[521]_\pi \otimes 7/2^-[514]_\pi\}^{(4+)}$ and $\{3/2^+[622]_\upsilon \otimes 7/2^+[624]_\upsilon\}^{(5+)}$.

K^π	Configuration		$E_{ex.}$ (keV)	g_K
	π^2	υ^2		
4^+	$\{1/2^-[521]_\pi \otimes 7/2^-[514]_\pi\}$		947	0.438
4^-	$\{9/2^+[624]_\pi \otimes 1/2^-[521]_\pi\}$		1244	1.572
4^-	$\{1/2^-[521]_\pi \otimes 7/2^+[633]_\pi\}$		1373	1.042
4^-	$\{1/2^+[400]_\pi \otimes 7/2^-[514]_\pi\}$		1868	1.038
4^-		$\{9/2^-[734]_\upsilon \otimes 1/2^+[620]_\upsilon\}$	1338	-0.067
4^+		$\{1/2^+[620]_\upsilon \otimes 7/2^+[613]_\upsilon\}$	1462	-0.491
4^-		$\{11/2^-[725]_\upsilon \otimes 3/2^+[622]_\upsilon\}$	1704	-0.501
4^+		$\{1/2^+[620]_\upsilon \otimes 7/2^+[624]_\upsilon\}$	1776	0.025
4^+		$\{9/2^-[734]_\upsilon \otimes 1/2^-[501]_\upsilon\}$	1781	-0.587
4^-		$\{1/2^-[501]_\upsilon \otimes 7/2^+[613]_\upsilon\}$	1904	0.028
5^+	$\{7/2^-[514]_\pi \otimes 3/2^-[521]_\pi\}$		1761	0.991
5^+		$\{3/2^+[622]_\upsilon \otimes 7/2^+[613]_\upsilon\}$	1563	-0.072
5^-		$\{11/2^-[725]_\upsilon \otimes 1/2^+[620]_\upsilon\}$	1602	-0.080
5^+		$\{3/2^+[622]_\upsilon \otimes 7/2^+[624]_\upsilon\}$	1878	0.341
6^+	$\{5/2^-[512]_\pi \otimes 7/2^-[514]_\pi\}$		1551	1.015
6^-	$\{5/2^-[512]_\pi \otimes 7/2^+[633]_\pi\}$		1977	1.417
6^-		$\{3/2^+[622]_\upsilon \otimes 9/2^-[734]_\upsilon\}$	1440	-0.047
6^-		$\{11/2^-[725]_\upsilon \otimes 1/2^+[620]_\upsilon\}$	1602	-0.336
6^+		$\{7/2^+[613]_\upsilon \otimes 5/2^+[622]_\upsilon\}$	1961	-0.355
7^-	$\{5/2^-[512]_\pi \otimes 9/2^+[624]_\pi\}$		1848	1.379
7^-		$\{5/2^+[622]_\upsilon \otimes 9/2^-[734]_\upsilon\}$	1838	-0.293

Table 7.1: Configurations for $K = 4$, 5, 6 and 7. Table 7.4 lists $K = 8$ configurations and excitation energies and Table 7.3 lists $K = 8$ g_K values. The first $K = 4$ configuration is identical to the one used for the $K = 3$ state in this study.

7.2 Discussion of focal plane slow-isomer decay spectroscopy results

The good experimental agreement with the theoretical two-proton structure for the ratio $I_\gamma(82\text{ keV})/I_\gamma(151\text{ keV})$ is indicated in Figure 6.15. The experimentally determined g_K^{exp} value of 1.03±0.07, determined from the $I_\gamma(82\text{ keV})/I_\gamma(151\text{ keV})$ ratio, points favourably towards the theoretical value given by the two-proton structure, formed from the single-particle orbitals predicted around the Fermi surface, $\{1/2^-[521]_\pi \otimes 7/2^-[514]_\pi\}^{(3+)}$, where $g_K^{\pi\pi} = 0.908$, compared to the two-neutron structure, $\{7/2^+[624]_\upsilon \otimes 1/2^+[620]_\upsilon\}^{(3+)}$, where $g_K^{\upsilon\upsilon} = 0.57$. We therefore define the $K^\pi = 3^+$ band head as a two-proton excitation comprising of the $1/2^-[521]_\pi$ state which arises from the $2f_{5/2}$ orbital from above the $Z = 114$ shell gap.

Figure 7.5 presents the agreement of the experimental data with the two-proton structure over that of the two-neutron structure. The data for the two configurations was obtained from Tables 6.9 and 6.10.

For the two transitions identified in Section 6.4, 53 keV and 778 keV, which link

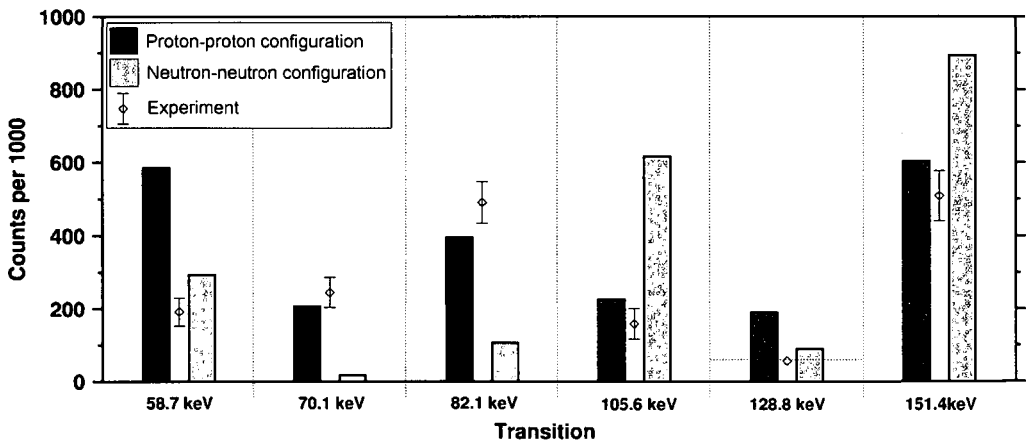

Figure 7.5: Graphical representation of data provided in Tables 6.9 and 6.10 compared to experiment.

the $K^\pi = 8^-$ isomer to the $K^\pi = 3^-$ band and the ground-state band, we have calculated the hindrance per degree of K forbiddenness f_ν using Equation 2.69. We have used GSI data to make the calculation from which we use $I_\gamma(778\text{ keV})/I_\gamma(53\text{ keV}) = 0.078\pm0.018$. When calculating the $\left(T_{1/2}\right)_{exp}$ component one needs to take into account additional branches of decay. This is achieved by calculating the partial γ-ray half-life term using the following method

$$(T_{1/2})_{exp} = T_{1/2}^{level}\left[\frac{\sum_i [I_{\gamma i}(1+\alpha_i)]}{I_\gamma}\right], \tag{7.4}$$

where $T_{1/2}^{level}$ is the half life of the isomeric state, α is the total internal conversion coefficient and I_γ is the intensity of the γ-ray transitions. The γ-ray transition intensity which forms the denominator is the intensity of the γ-ray transition for which f_ν is calculated.

For the $K^\pi = 8^- \rightarrow K^\pi = 3^+$ 53-keV transition, $f_\nu(E1) = 822\pm10$, which is in good agreement with the value given in reference [Ta06] of $f_\nu = 804$. For the direct decay to the $K^\pi = 0^+$ ground-state band, 778 keV, $f_\nu(E1) = 210\pm7$. Figure 7.6 compares reduced hindrance factors for $\Delta K = 8$ E1 transitions as a function of the ratio of the dynamic and kinematic moments of inertia for a number of nuclei. The nuclei ^{172}Hf, ^{250}Fm and ^{252,254}No have more than one decay branch from the $K^\pi = 8^-$ state. Intensities for the branches from the $K^\pi = 8^-$ state in ^{172}Hf were taken from reference [Wa94] (and the reference was also used to confirm the calculations of f_ν). Data was taken from reference [Dr06] to calculate f_ν for the $N = 106$ isotones and data was taken from reference [Fi96] to calculate f_ν for ^{180,182}Hf. Data for ^{250}Fm was obtained from reference [Gr08] which provides evidence of a $K^\pi = 8^-$ 1.92-s isomeric state. Reference [Gr08] states branching ratios for a 682-keV E1 transition (direct decay from the $K^\pi = 8^-$ state to the $K^\pi = 0^+$ ground state band) and a 23-keV M1 transition ($K^\pi = 8^- \rightarrow K^\pi = 2^-$) at approximately 18 % and 82 % respectively. From this we deduce $f_\nu(E1) = 442$ for 682 keV and $f_\nu(M1) = 185$ for 23 keV. Data for ^{252}No was obtained from reference [Su07] which gives evidence of a 710-keV direct decay from a $K^\pi = 8^-$ 110 ms isomeric state to the $K^\pi = 0^+$ ground-state band. The decay branch of the 710-keV transition is 4% compared to branches totalling 96%

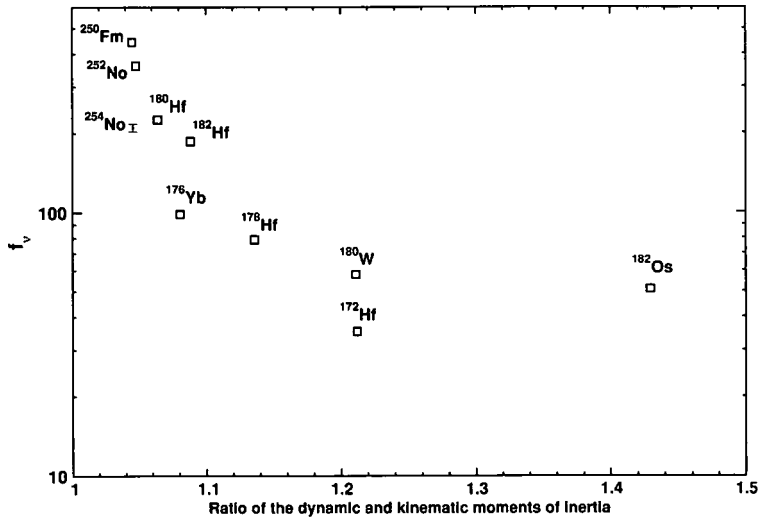

Figure 7.6: Reduced hindrance factors for $\Delta K = 8$ E1 transitions as a function of the ratio of the dynamic and kinematic moments of inertia for the $8^+ \rightarrow 6^+$ and $8^+ \rightarrow 6^+$ ground state band γ-ray transition energies.

which feed an intermediate $K^\pi = 2^-$ band. From this we deduce $f_\nu(E1) = 360$ for the 710-keV transition.

Figure 7.6 shows a trend of increasing f_ν as the ratio of the dynamic and kinematic moments of inertia approach one. If K is a good quantum number then we have a rigid body and the two moments of inertia are equal. A high value of f_ν indicates that K is very pure because some form of K mixing must exist to enable K-forbidden transitions [Wa94]. The greater the dynamic and kinematic moments of inertia deviate the less the decay is hindered.

7.3 Discussion of in-beam recoil-isomer tagged and fast-isomer decay results

Based on the experimentally determined g_K^{exp} values of 1.00±0.08 and -0.20±0.01 for the $K^\pi = 8^-$ band we will discuss a number of possible configurations for the 8^- band-head state.

The experimental g_K^{exp} value of 1.00±0.08 is in excellent agreement with the proton-proton configuration, $\{7/2^-[514]_\pi \otimes 9/2^+[624]_\pi\}^{(8-)}$ where $g_K^{\pi\pi} = 1.006$. The other possible experimentally determined g_K^{exp} value of -0.20±0.01 agrees with the neutron-neutron configuration, $\{7/2^+[613]_\upsilon \otimes 9/2^-[734]_\upsilon\}^{(8-)}$, where $g_K^{\upsilon\upsilon}$ = -0.279, and not $\{7/2^+[624]_\upsilon \otimes 9/2^-[734]_\upsilon\}^{(8-)}$, where $g_K^{\upsilon\upsilon}$ = -0.021.

When considering the two possible neutron-neutron configurations the coupling of the $9/2^-[734]_\upsilon$ with the $7/2^+[624]_\upsilon$ is favoured over the coupling of the $9/2^-[734]_\upsilon$ and $7/2^+[613]_\upsilon$ orbitals according to the coupling rules of Gallagher [Gal62] for even-even nuclei, where anti-parallel intrinsic spin-couplings for like-nucleon pairs are favoured over parallel couplings, Table 7.2.

The $\{7/2^+[613]_\upsilon \otimes 9/2^-[734]_\upsilon\}^{(8-)}$ cannot be entirely excluded based on the coupling rules but the excitation energies calculated in Table 7.4 also point favourably at the proton-proton configuration. We therefore propose that the $K^\pi = 8^-$ state is formed from the $\{7/2^-[514]_\pi \otimes 9/2^+[624]_\pi\}^{(8-)}$ two-proton configuration. Table 7.3 shows those two quasi-particle configurations predicted with corresponding g_K val-

Single particle orbital	Ω - Λ	Σ
$9/2^-[734]_\upsilon$	9/2 - 4	+1/2
$7/2^+[624]_\upsilon$	7/2 - 4	-1/2
$7/2^+[613]_\upsilon$	7/2 - 3	+1/2

Table 7.2: The projection of the total angular momentum on the symmetry axis for the given single-particle orbitals.

Configuration	g_K
$\{7/2^-[514]_\pi \otimes 9/2^+[624]_\pi\}^{(8-)}$	1.006
$\{7/2^+[624]_\upsilon \otimes 9/2^-[734]_\upsilon\}^{(8-)}$	-0.021
$\{7/2^+[613]_\upsilon \otimes 9/2^-[734]_\upsilon\}^{(8-)}$	-0.279

Table 7.3: Suggested configurations for the $K = 8$ state.

ues and Figure 7.7 reiterates the good experimental agreement with the proposed two-proton structure. Although other configurations cannot be ruled out.

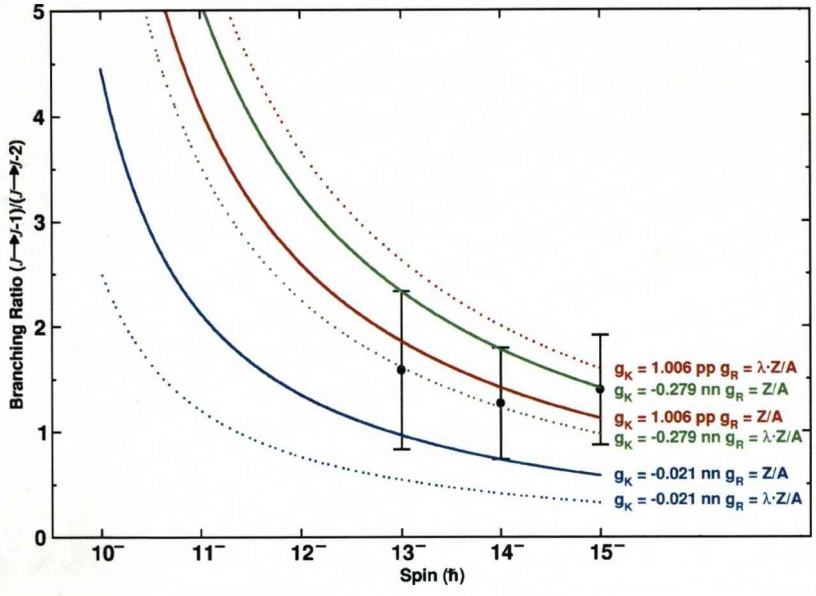

Figure 7.7: A plot of branching ratio versus spin for data collected at GSI for the $K^\pi = 8^-$ band. Experimental results are given for the ratios at spins 15^-, 14^- and 13^-. Theoretical values for the branching ratios with g_K set at 1.006 (proton-proton configuration), -0.021 and -0.279 (neutron-neutron configurations) are overlaid and are acquired from Tables 6.15, 6.16 and 6.17. We have also varied g_R, with the value set at Z/A ($g_R = 0.402$) and $\lambda \cdot Z/A$, where λ represents a quenching factor equal to 0.7 ($g_R = 0.281$). The previously ruled out g_K = -0.279 configuration is shown for completeness.

7.4 A general overview

7.4.1 Intermediate K bands

Figure 7.8 displays the level scheme which is configured via the results and arguments put forward in the previous sections. We are unable to determine the excitation energy at which the side band lies and we are unable to determine how this decays into the ground state band. However, we are able to determine the configuration of the band head of the $K^{\pi} = 3^{+}$ structure, comprising of the $1/2^{-}[521]_{\pi}$ and $7/2^{-}[514]_{\pi}$ orbitals which lie close to and on either side of the Fermi level, Figure 7.9. We resolve via the energies of the high-energy M1 transitions and the ground-state band $2^{+} \rightarrow 0^{+}$ transition that the band head lies at an excitation energy of (987.6±0.3) keV. We can compare this experimental energy value to that of the excitation energy for the configuration $\{1/2^{-}[521]_{\pi} \otimes 7/2^{-}[514]_{\pi}\}^{(3+)}$ calculated in Table 7.4 based on the same Woods-Saxon potential (WS) calculations made in Section 7.1.2. The forecasted excitation energy of 943 keV agrees favourably with the experimental value.

We can also compare the experimental excitation energy to those which are produced using two further models. Reference [Ta06] calculates a $K^{\pi} = 3^{+}$ proton two-quasiparticle state at 1180 keV using the Skyrme Hartree-Fock Bogolyubov (SHFB) model with the SLy4 force [Be03a] which is close to the experimental value. Reference [Ta06] also cites Figure 5 of reference [Af03] where calculations have been performed using the relativistic mean-field (RMF) model. Reference [Ta06] yields an energy of greater than 2 MeV using the RMF model for the $K^{\pi} = 3^{+}$ state which is too high in energy.

7.4.2 $K^{\pi} = 8^{-}$ band

The $K^{\pi} = 8^{-}$ isomeric state has an experimental excitation energy of (1298.2±0.8) keV. The excitation energy calculated using the WS model in Table 7.4 of the proposed configuration, $\{7/2^{-}[514]_{\pi} \otimes 9/2^{+}[624]_{\pi}\}^{(8-)}$, of this state is equal to 1255 keV which is in good agreement with the experimental value. Once more we compare

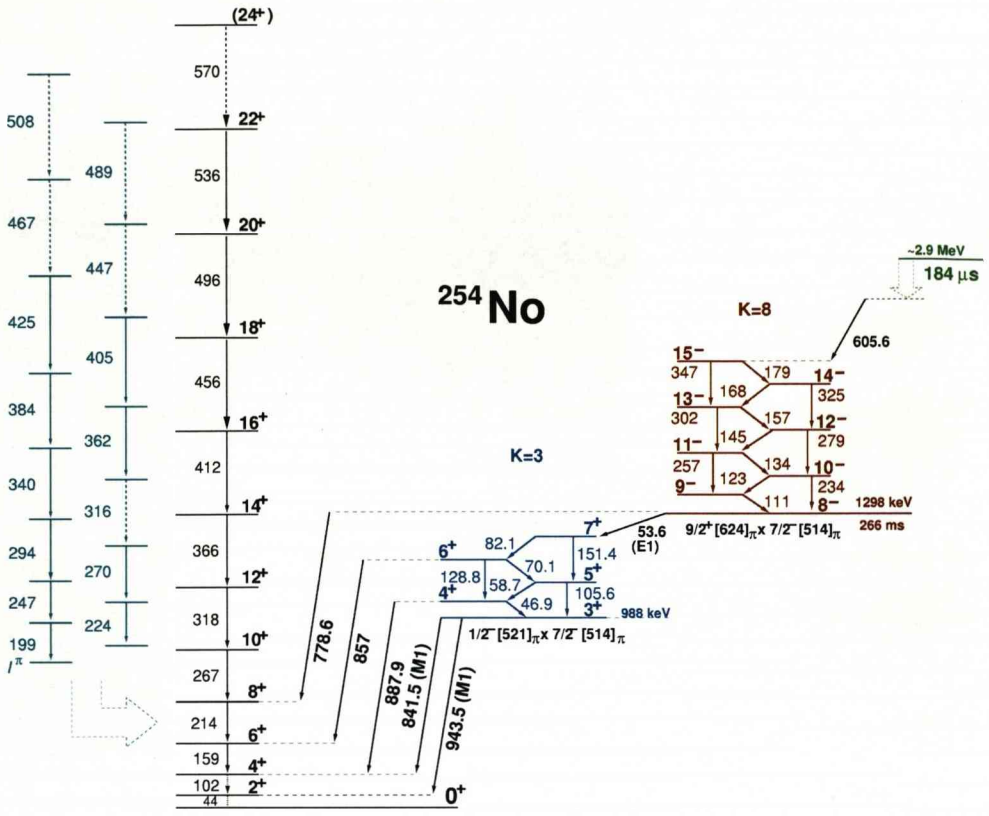

Figure 7.8: Proposed level scheme of ^{254}No. The transitions at energy 778.6 keV and 857 keV, the floating side band, and transitions built on top of the $K^{\pi} = 8^{-}$ isomeric state are new additions to the level scheme modified from reference [He06].

the experimental excitation energy value to those calculated by different models in reference [Ta06]. The SHFB model with the SLy4 force produces a proton two-quasiparticle $K^{\pi} = 8^{-}$ state at 2200 keV and the RMF model produces an energy greater than 2000 keV, both are far higher than the experimental values and the calculated WS value.

The $\{7/2^{+}[613]_{\upsilon} \otimes 9/2^{-}[734]_{\upsilon}\}^{(8-)}$ configuration, previously ruled out in Section 7.3, has a calculated excitation energy (Table 7.4) which is close to the experimental value, especially if one subtracts a residual spin-spin interaction of 100 keV [Ta06]. But we feel that the argument put forward for the classification of the $K^{\pi} = 8^{-}$ isomeric state

K^π	Configuration		Energy (keV)		
	υ^2	π^2	$E_{ex.}$	$E_{expt.}$	ΔE
3^+		$\{1/2^-[521]_\pi \otimes 7/2^-[514]_\pi\}$*	947	988	-41
8^-	$\{7/2^+[613]_\upsilon \otimes 9/2^-[734]_\upsilon\}$		1412	1293	+119
8^-	$\{7/2^+[624]_\upsilon \otimes 9/2^-[734]_\upsilon\}$		1727	1293	+434
8^-		$\{7/2^-[514]_\pi \otimes 9/2^+[624]_\pi\}$*	1255	1293	-38
8^+		$\{7/2^+[633]_\pi \otimes 9/2^+[624]_\pi\}$	1681	1293	+388
16^+	$\{7/2^+[613]_\upsilon \otimes 9/2^-[734]_\upsilon\}$	$\{7/2^-[514]_\pi \otimes 9/2^+[624]_\pi\}$	2667	-	-
16^+	$\{7/2^+[624]_\upsilon \otimes 9/2^-[734]_\upsilon\}$	$\{7/2^-[514]_\pi \otimes 9/2^+[624]_\pi\}$	2982	-	-
17^+	$\{11/2^-[725]_\upsilon \otimes 7/2^+[613]_\upsilon\}$	$\{7/2^-[514]_\pi \otimes 9/2^+[624]_\pi\}$	2932	(2920)	(+12)
17^+	$\{11/2^-[725]_\upsilon \otimes 7/2^+[624]_\upsilon\}$	$\{7/2^-[514]_\pi \otimes 9/2^+[624]_\pi\}$	3246	(2920)	(+326)
18^-	$\{11/2^-[725]_\upsilon \otimes 9/2^-[734]_\upsilon\}$	$\{7/2^-[514]_\pi \otimes 9/2^+[624]_\pi\}$	2808	-	-

Table 7.4: Configurations and excitation energies. Calculations of the excitation energies for ^{254}No are performed using a Woods-Saxon potential with "Universal" parameterisation. An asterisk denotes an assigned configuration.

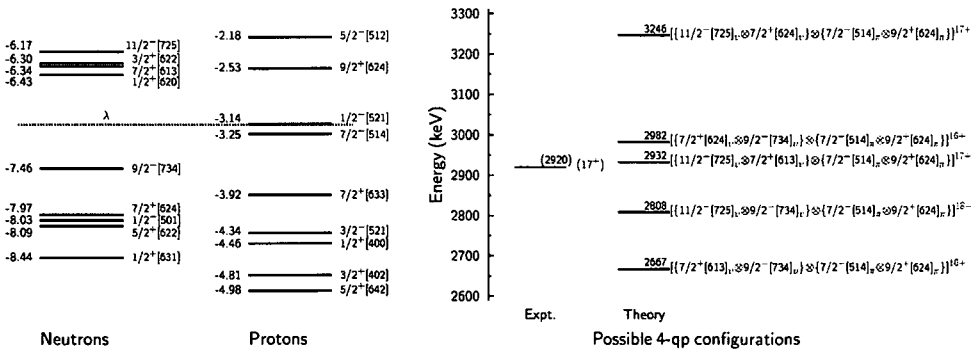

Figure 7.9: Four-quasiparticle excitation energies and single-particle energies. The experimental value is enclosed within brackets because it is still highly provisional.

as a proton two-quasiparticle structure is well grounded. If the $K^{\pi} = 8^{-}$ isomeric state was defined as a neutron two-quasiparticle structure then the decay from the 8^{-} state to the 3^{+} state would involve the transition of two neutrons and two protons rather than a single proton.

The 605 keV transition in the $K^{\pi} = 8^{-}$ band is observed prompt in the JUROGAM recoil-isomer tagged spectrum of Figure 6.17 and therefore does not directly depopulate the 184-μs isomer. Consequently, if it feeds the band in a way in which is displayed in Figure 7.8, then the 184-μs isomeric state does not have spin and parity 16^{+} as proposed in reference [He06]. It is conceivable that the isomer is depopulated by a transition too low in energy, and hence highly converted, to be detected, similar to the 23 keV M1 transition which is believed to depopulate the isomeric $K^{\pi} = 8^{-}$ state in ^{250}Fm [Gr08]. If this is the case then the isomeric state would be of spin $17\hbar$. Calculations of excitation energies for several suggested $K = 16$, 17 and 18 states are put forward in Table 7.4 and are displayed in Figure 7.9. It is expected that residual proton-neutron interactions would require an energy of approximately 0.2 MeV to be subtracted from the WS calculations made in Table 7.4 for four-quasiparticle configurations [Ta06].

One distinct caveat still remains, the intensity of the 134-keV transition is far greater than one would expect for a M1 transition and leads us to turn to an analogy with ^{178}Hf. In ^{178}Hf two $K^{\pi} = 8^{-}$ two-quasiparticle bands are observed, if this is the case for ^{254}No, with similar interband transition energies, then it would be very difficult to assign each transition to the correct band without the high statistics required for γ - γ angular correlation measurements, but would explain discrepancies in the intensities of transitions.

7.4.3 Collective picture

Figure 7.10 shows the dynamical moment of inertia calculated for the ground state band and for the $K^{\pi} = 8^{-}$ band in the upper panel and the total aligned angular momentum for the ground state, $K^{\pi} = 3^{+}$ and $K^{\pi} = 8^{-}$ bands in the lowel panel.

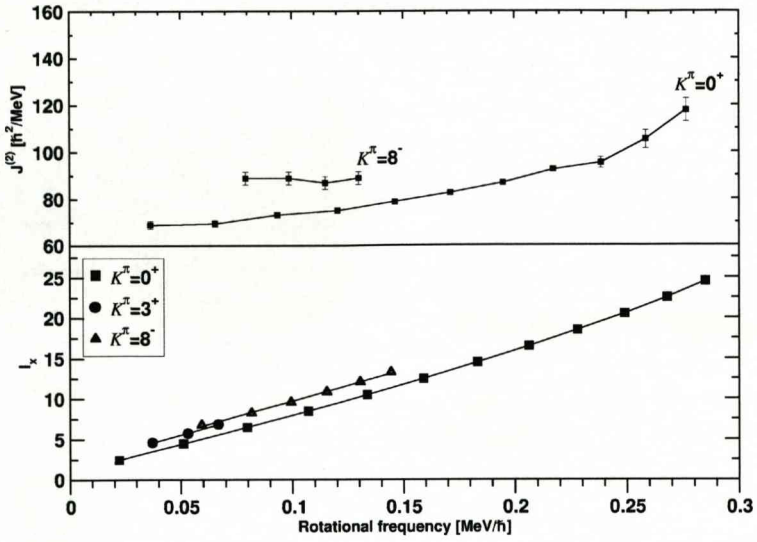

Figure 7.10: Dynamical moment of inertia and total aligned angular momentum as a function of rotational frequency for ^{254}No.

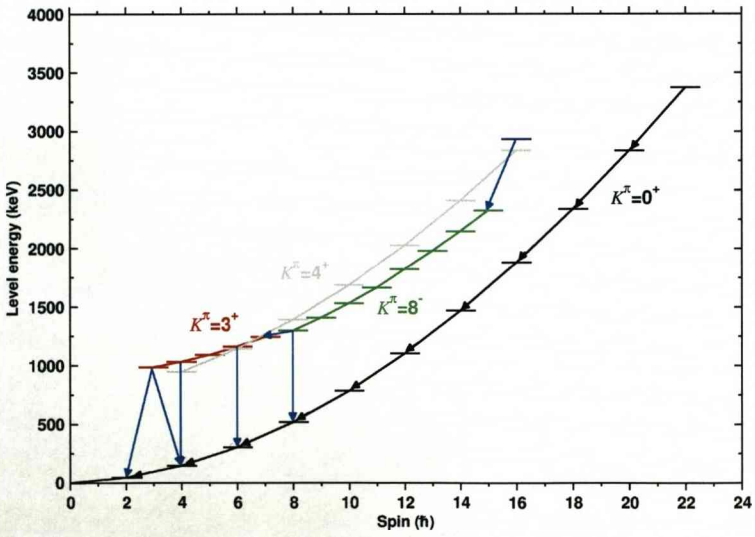

Figure 7.11: Yrast plot for ^{254}No. The plot includes proposed side band transitions built on top of the favoured $K^\pi = 4^+$ $\{1/2^-[521]_\pi \otimes 7/2^-[514]_\pi\}$ configuration.

The upbend in moment of inertia predicted for ^{254}No lies at a rotational frequency of $\simeq 0.3$ MeV/$\hbar$ due to the simultaneous alignment of a proton $i_{13/2}$ pair and a neutron $j_{15/2}$ pair. However, current experimental data does not indicate a sudden upbend, but that a more gradual upbend should arise resulting from the simultaneous alignment of two high-j orbitals. Studies by reference [Eg00] predict that the stability of nucleus may persist up to spin value of $\approx 40\hbar$ or even higher. The feeding of the ground-state band is shown schematically in the yrast plot of Figure 7.11. We have overlaid the transitions within the proposed side band using a band-head energy calculated using the $K^{\pi} = 4^{+}$ $\{1/2^{-}[521]_{\pi} \otimes 7/2^{-}[514]_{\pi}\}$ configuration.

7.4.4 Systematics

Figure 7.12 displays the systematics of the known K isomers and lowest-lying non-yrast states in the $N = 150$ and $N = 152$ isotones. Information on the $N = 152$ isotones is sparse and we view a more extensive picture for the $N = 150$ isotones. The 8^{-} states in the $N = 150$ isotones all possess the $\{7/2^{+}[624]_{\upsilon} \otimes 9/2^{-}[734]_{\upsilon}\}^{(8-)}$ configuration.

The question arises as to why the $Z = 102$ isotopes of ^{252}No and ^{254}No have different neutron and proton two-quasiparticle configurations for each 8^{-} isomer. Figure 7.9 shows that the deformed shell gap at $N = 152$, enclosed by the $1/2^{+}[620]_{\upsilon}$ and $9/2^{-}[734]_{\upsilon}$ states, would result in neutron configurations lying at a much higher excitation energy than experimental values. Counter to this, for ^{252}No, $N = 150$, the Fermi surface moves below the $N = 152$ gap between the $9/2^{-}[734]_{\upsilon}$ and $7/2^{+}[624]_{\upsilon}$ states. Thus the energy of the possible neutron configuration is lowered substantially.

A similar analysis can be made if we consider proton two-quasiparticle configurations for ^{250}Fm. Much higher excitation energies are calculated because the Fermi surface is positioned in the deformed shell gap at $Z = 100$, lying between the $1/2^{-}[521]_{\pi}$ and $7/2^{+}[633]_{\pi}$ states.

From the systematics we can conclude that the experimental data indicates deformed shell gaps at $Z = 100$ and $N = 150$. This is in contradiction to recent cal-

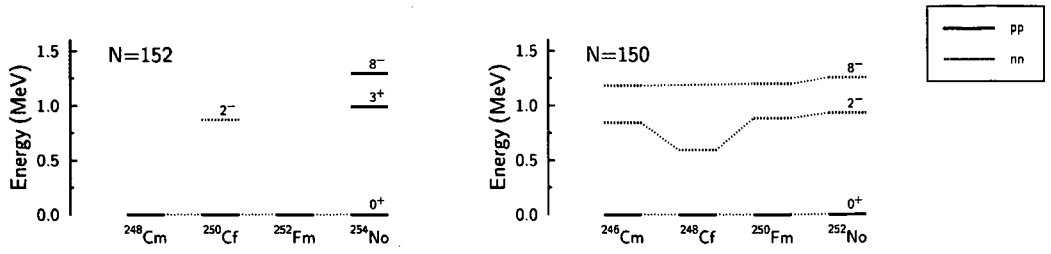

Figure 7.12: K isomers and lowest-lying non-yrast states in the N=150,152 isotones. Figure modified from [He08].

culations made by Chatillon *et al.* using the Skyrme SLy4 interaction, displayed in Figure 5.4 [Cha06]. From Figure 5.4 we observe that the $1/2^-[521]_\pi$ state from the $2f_{5/2}$ shell and the $7/2^-[514]_\pi$ state from the $1h_{9/2}$ shell are in close proximity and replicates the 3^+ state in ^{254}No. However, the $9/2^+[624]_\pi$ state from the $1i_{13/2}$ shell is more than likely positioned too far away from the $7/2^-[514]_\pi$ state to agree with the excitation energy calculated by the experiment.

These disagreements call for a further reanalysis of the theoretical calculations. There is a growing systematic picture of single-particle states within this region which can provide a test to models predicting the location of the island of stability and beyond.

Chapter 8

Summary and Future Prospects

8.1 Summary

A number of experiments have been performed to investigate the structure of ^{254}No using the ^{208}Pb(^{48}Ca,2n)^{254}No fusion evaporation reaction. The main aims of the experiments were to clarify and build on the structure and decay path of a previously identified isomeric state [Gh73]. We have also employed the RDT technique and in-beam γ-ray spectroscopy to increase the accuracy of the measurement of the half-life of the isotope and to propose an additional structure feeding the ground-state band.

We have determined the half-life of the ^{254}No α decay to be $T_{1/2}$=(51.0±0.3) s which is consistent with the most recent data evaluation in the ENSDF data base (June 2008) of (48±3) s [Le99].

Our γ-γ coincidence results of in-beam γ-ray spectroscopy data of the ground-state band are in agreement with previously published results [Ee05], extending the ground state band up to spin 24$\hbar$. Furthermore, we have placed previously unidentified transitions into a side band. Several of the transitions exhibit γ-γ coincidences with the low-energy ground-state band transitions. We have been unable to determine how this side band feeds into the ground-state band and hence we are unable to determine an excitation energy, but we have been able to suggest several possible band-head configurations, notably $\{1/2^-[521]_\pi \otimes 7/2^-[514]_\pi\}^{(4+)}$ and $\{3/2^+[622]_\upsilon \otimes 7/2^+[624]_\upsilon\}^{(5+)}$.

These configurations have values of $g_K \approx g_R$ which would be consistent with our proposal that the transitions identified are of multipolarity E2 and that we have not identified interleaving M1 transitions due to their relatively weak intensities.

Analysis of the focal plane slow isomer decay spectroscopy data has resulted in the confirmation of an isomer of 266±2 ms at spin and parity, 8^-. The half life is in fine agreement with Ghiorso's primary measurement [Gh73]. We have established a decay scheme from the isomer to the ground-state band. The isomer decays via an E1 778-keV transition direct to the ground-state band (f_ν = 210±7) and via an E1 53-keV transition (f_ν = 822±10) into a $K = 3^+$ band. Calculations performed using the branching ratios of transitions within the band resulted in $g_K^{exp} = 1.03\pm0.07$ and from this we deduce a two-proton structure of $\{1/2^-[521]_\pi \otimes 7/2^-[514]_\pi\}^{(3+)}$ for the band head. The configuration comprises of the $1/2^-[521]_\pi$ state which arises from the $2f_{5/2}$ orbital from above the $Z = 114$ shell gap.

Observations of high-energy decays depopulating the $K^\pi = 3^+$ band into the ground-state band established a measurement of the ground state band $4^+ \rightarrow 2^+$ transition energy to a far greater degree of accuracy than what has been previously measured, Section 6.4.3. Using this transition energy we were able to improve our measurement of the ground-state band $2^+ \rightarrow 0^+$ transition energy using a Harris fit, Section 7.1.1.

A study of the decay of a fast isomer permitted the measurement of its half-life and shows that it decays into a rotational band built on top of the 266-ms isomeric $K^\pi = 8^-$ state. The half-life of this shorter lived isomer was found to be 184±2 μs.

In-beam recoil-isomer tagging and fast isomer decay results from JYFL and isomer decay results from GSI were analysed to establish the structure built on top of the $K^\pi = 8^-$ isomer. Results from GSI permitted the deduction of $g_K^{exp} = 1.00\pm0.08$ or -0.20±0.01. Unfortunately, both values agreed with the g_K results calculated for both two-proton and two-neutron structures. However, Section 7.3 puts forward an argument in which we propose a two-proton $\{7/2^-[514]_\pi \otimes 9/2^+[624]_\pi\}^{(8-)}$ configuration for the $K^\pi = 8^-$ state.

We have proposed several configurations for the structure of the 184 μs isomer and these are listed in Table 7.4.

The experimental two-quasiparticle data obtained in the $Z \approx 102$ region can provide a stringent test for self-consistent theories. But presently few theoretical calculations exist and those that do require modifications in order to reproduce the correct ordering of single-particle levels.

8.2 Future prospects

One limiting factor in this investigation has been the inability to simultaneously detect γ rays and conversion electrons at the target position. In the $Z \gtrsim 100$ region the low-energy transitions are dominated by internal conversion. For example, the total internal conversion coefficient of an E2 transition energy of approximately 200 keV in a $Z = 102$ nucleus is 1.6, meaning that any transition of lower energy is more than 60 % converted. This implies that it is very difficult to study nuclei via the in-beam recoil isomer tagging technique used in this study using only γ-ray spectroscopy to identify low-energy transitions belonging to the structure above isomeric states. In order to attempt to overcome this and other problems a spectrometer is currently being constructed at the target position at JYFL. The SAGE (Silicon And GErmanium) spectrometer builds on the success of the SACRED spectrometer [Ka04]. The spectrometer will operate in conjunction with RITU and GREAT and will consist of a segmented silicon detector (90 pixels) for detection of conversion electrons and a Ge array to detect γ rays. From the target position the conversion electrons will follow spiral trajectories in a system of solenoidal magnetic fields back upstream of the beam direction to the Si detector allowing for the simultaneous detection of both conversion electrons and γ rays (via the Ge detector array).

Furthermore, important measurements on the border of the super-heavy region can be conducted by SAGE on odd-mass nuclei, for example ^{251}Md, ^{253}No and ^{255}Lr. These measurements will provide a probe into the single-particle structure of super-

heavy nuclei, permitting the detection of M1 transitions via in-beam conversion electron spectroscopy and E2 transitions via in-beam γ-ray spectroscopy simultaneously to build up a picture of coupled bands. The experimentally observed bands allow the calculation of *B(M1)/B(E2)* ratios from which configurations can be deduced. The results will provide an insight into the relative positioning of several key orbitals critical for the establishment of a possible shell closure at $Z = 114$.

Recently, the use of digital electronics was explored at JYFL using the TNT (Tracking Numerical Treatment) digital pulse processing cards to instrument germanium detectors. The TNT modules [Ar06] exploit FPGAs (field programmable gate arrays) which provide a parallel data treatment capability, enabling a greater throughput and the reduction of event processing time. The module can sustain an event rate of 50 kHz per channel, thus ideal for high beam intensity experiments at JYFL (although it is expected that experiments will run at a maximum of 30-40 kHz per detector when SAGE comes online [Pa08]).

Figure 8.2 displays a trial data collection run of TNT digital pulse processing

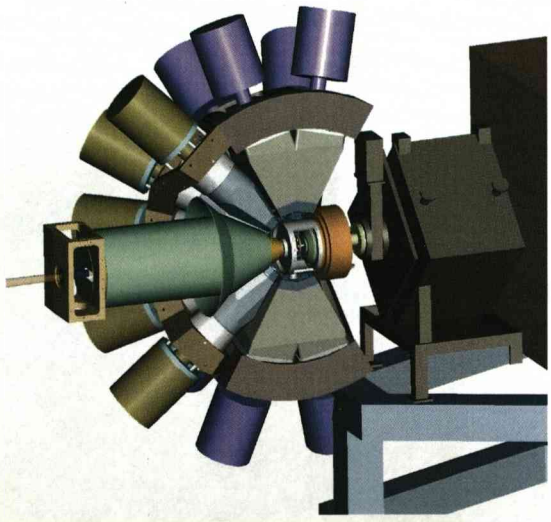

Figure 8.1: Schematic drawing of the SAGE spectrometer and a cross-section of the JUROGAM II Ge detector array coupled to RITU [Se07].

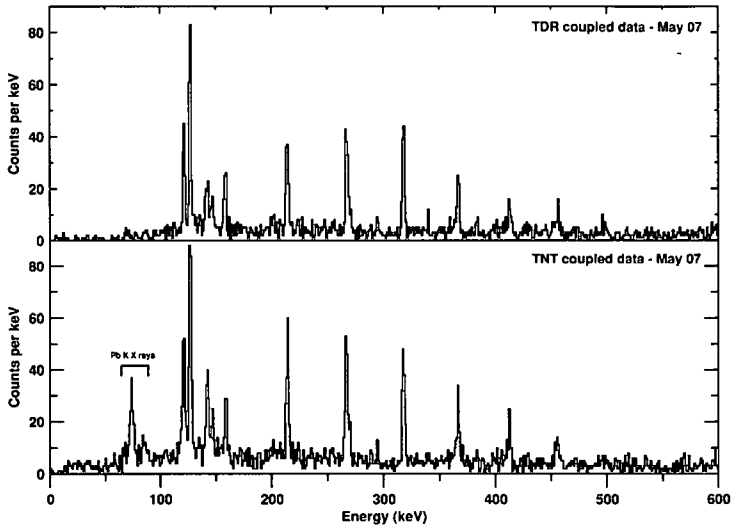

Figure 8.2: A comparison of data collected at JYFL using two different data acquisition systems. The ground state rotational band of ^{254}No is shown. The bottom panel shows the data collected by the TNT data acquisition system over a period of approximately 50 % of the total run time of the ^{254}No May 2007 experiment. The top panel shows the data collected by the TDR data acqisition system over the same period. The TNT data provides better data collection at lower energy which is confirmed by the collection and identification of target Pb X-rays.

(coupled to TDR over the same period of time) taken during the May 2007 experiment. Due to the shorter trapezoidal pulse shaping time (replacing the analogue Gaussian shaping) we see more counts and peaks with better energy resolution.

These improvements will permit the experimentalist to investigate new cross-section limits in heavier mass regions which we have yet to fully explore. Odd-mass isotopes of lawrencium, rutherfordium and dubnium will become accessible to gain information on the single-particle structure. The experimentalist will have the advantage of being able to probe the nuclear chart, gaining a first reasonable glimpse into the most inaccessible regions, and to also build on what has already been studied with the aid of greater precision and detail.

Bibliography

[Ab04] K. Abu Saleem *et al.*, "Alignments in the odd-proton actinides ^{237}Np and ^{241}Am", *Phys. Rev.* C **70** (2004) 024310

[Af03] A.V. Afanasjev *et al.*, "Cranked relativistic Hartree-Bogoliubov theory: Probing the gateway to superheavy nuclei", *Phys. Rev.* C **67** (2003) 024309

[Ah84] I. Ahmed and J.L. Lerner, "Alpha-decay properties of ^{247}Cf, ^{248}Cf, ^{252}Fm and ^{254}Fm", *Nucl. Phys.* A **413** (1984) 423

[An04] A.N. Andreyev *et al.*, "GEANT Monte Carlo simulations for the GREAT spectrometer", *Nucl. Instrum. Meth.* A **533** (2004) 422

[Ar06] L. Arnold *et al.*, "TNT Digital Pulse Processor", *IEEE Trans. Nucl. Sci.* **53** (2006) 3

[Ba80] R. Bass, "Nuclear Reactions with Heavy Ions", *Springer-Verlag Berlin*, (1980)

[Ba06] J.E. Bastin *et al.*, "In-beam gamma ray and conversion electron study of ^{250}Fm", *Phys. Rev.* C **73** (2006) 024308

[Be99] M. Bender *et al.*, "Shell structure of superheavy nuclei in self-consistent mean-field models", *Phys. Rev.* C **60** (1999) 034304

[Be01] M. Bender, W. Nazarewicz, P.-G. Reinhard, "Shell stabilization of super- and hyperheavy nuclei without magic gaps", *Phys. Lett.* B **515** (2001) 42

[Be03a] M. Bender *et al.*, "Skyrme mean-field study of rotational bands in transfermium isotopes", *Nucl. Phys.* A **723** (2003) 354

[Be03b] M. Bender and P.-H. Heenen, "Self-consistent mean-field models for nuclear structure", *Rev. Mod. Phys.* **75** (2003) 121

[Bo40] N. Bohr, "Scattering and Stopping of Fission Fragments", *Phys. Rev.* **58** (1940) 654

[Bo98] A. Bohr and B.R. Mottelson, "Nuclear Structure", *W.A. Benjamin Inc.*, (1998)

[Br05] B.A. Brown, "Lecture Notes in Nuclear Structure Physics", *National Superconducting Cyclotron Laboratory and Department of Physics and Astronomy Michigan State University* (2005)

[Bu02] P.A. Butler *et al.*, "Conversion Electron Cascades in ^{254}No", *Phys. Rev. Lett.* **89** (2002) 202501

[Ca00] R.F. Casten, "Nuclear Structure From A Simple Perspective", *Oxford University Press Inc.* (2000)

[Ch77] R.R. Chasman, I. Ahmad, A.M. Friedman and J.R. Erskine, "Survey of single-particle states in the mass region A 228", *Rev. Mod. Phys.* **49** (1977) 4

[Cha06] A. Chatillon *et al.*, "Spectroscopy and single-particle structure of the odd- Z heavy elements ^{255}Lr, ^{251}Md and ^{247}Es", *Eur. Phys. J.* A **30** (2006) 397

[Ch04] E.A. Cherepanov, "Production Cross Sections of Super Heavy Elements", *Brazilian Journal of Physics* **34** 3A 954 (2004)

[Co58] B.L. Cohen and C.B. Fulmer, "Fission-fragment mass separator and the nuclear charge distribution of fission fragments of a single mass", *Nucl. Phys.* **6** (1958) 547

[Ćw87] S. Ćwiok, J. Dudek, W. Nazarewicz, J. Skalski and T. Werner, "Single-particle energies, wave functions, quadrupole moments and g-factors in an axially deformed woods-saxon potential with applications to the two-centre-type nuclear problems", *Comp. Phys. Comm.* **46** (1987) 379

[Ćw96] S. Ćwiok *et al.*, "Shell structure of the superheavy elements", *Nucl. Phys.* A **611** (1996) 211

[Ćw05] S. Ćwiok, P.-H. Heenen and W. Nazarewicz, "Shape coexistence and triaxiality in the superheavy nuclei", *Nature* **433** (2005) 705

[Dr06] G.D. Dracoulis *et al.*, "Two-quasiparticle K-isomers and pairing strengths in the neutron-rich isotopes ^{174}Er and ^{172}Er", *Phys. Lett.* B **635** (2006) 200

[Ee05] S. Eeckhaudt *et al.*, "Evidence for non-yrast states in ^{254}No", *Eur. Phys. J.* A **26** (2005) 227

[Ee06] S. Eeckhaudt, "Spectroscopy in the Transfermium Region: Probing Rotational, Non-Yrast and Isomeric Structures in ^{253,254}No", *PhD Thesis, The University of Jyväskylä* (2006)

[Eg00] J.L. Egido and L.M. Robledo, "Fission Barriers at High Angular Momentum and the Ground State Rotational Band of the Nucleus ^{254}No", *Phys. Rev. Lett.* **85** (2000) 1198

[Fi96] R.B. Firestone, "Table of Isotopes", *John Wiley and Sons Inc.* (1996)

[Fr77] M.S. Freedman *et al.*, "Two-quasiparticle states in ^{250}Cf populated by electron capture decay of 8.6-h ^{250}Es isomer", *Phys. Rev.* C **15** (1977) 760

[Gä89] H.W. Gäggeler *et al.*, "Cold fusion reactions with ^{48}Ca", *Nucl. Phys.* A **502** (1989) 561

[Gal62] C.J. Gallagher, Jr., "Coupling of Angular Momenta in Two-Particle States in Deformed Even-Even Nuclei", *Phys. Rev.* **126** (1962) 1525

[Gh73] A. Ghiorso *et al.*, "Isomeric States in ^{250}Fm and ^{254}No", *Phys. Rev.* C **7** (1973) 2032

[Gh88] A. Ghiorso *et al.*, "Sassy, a gas-filled magnetic separator for the study of fusion reaction products", *Nucl. Instrum. Meth.* A **269** (1988) 192

[Gr04] P.T. Greenlees *et al.*, "In-beam spectroscopy at the RITU gas-filled recoil separator", *Eur. Phys. J.* A **20** (2004) 87

[Gr08] P.T. Greenlees *et al.*, "High-K Structure in ^{250}Fm and the Influence of the Deformed Shell Gaps at N=152 and Z=100", *To be published.*

[Ha98] G. Hackman *et al.*, "High-spin properties of octupole bands in ^{240}Pu and ^{248}Cm", *Phys. Rev.* C **57** (1998) R1056

[Ha65] S.M. Harris, "Higher Order Corrections to the Cranking Model", *Phys. Rev.* **138** (1965) B509

[He01] R. -D. Herzberg *et al.*, "Spectroscopy of transfermium nuclei: ^{252}No", *Phys. Rev.* C **65** (2001) 014303

[He06] R. -D. Herzberg *et al.*, "Nuclear isomers in superheavy elements as stepping stones towards the island of stability", *Nature* **442** (2006) 896

[He07] R. -D. Herzberg, *private communication*, rdh@ns.ph.liv.ac.uk

[He08] R. -D. Herzberg and P.T. Greenlees, "In-beam and decay spectroscopy of transfermium nuclei", *To be published.*

[Hey04] K. Heyde, "Basic ideas and concepts in nuclear physics", *Institute of Physics Publishing* (2004)

[Ho78] P.E. Hodgson, "Nuclear Heavy Ion Reactions", *Oxford Clarendon Press* (1978)

[Ho95] S. Hofmann *et al.*, "The new element 111", *Z. Phys.* A. **350** (1995) 281

[Ho98] S. Hofmann *et al.*, "New elements - approaching Z=114", *Rep. Prog. Pys.* **61** (1998) 639

[Ho00] S. Hofmann and G. Münzenberg, "The discovery of the heaviest elements", *Rev. Mod. Phys.* **72** (2000) 733

[Ho01] S. Hofmann *et al.*, "The new isotope ^{270}110 and its decay products ^{266}Hs and ^{262}Sg", *Eur. Phys. J.* A **10** (2001) 5

[Ho03] S. Hofmann, "Synthesis and Properties of Superheavy Elements", *J. Nucl. Radiochem. Sci.* **4** (2003) R1

[Hu04] R.D. Humphreys *et al.*, "In-beam electron spectroscopy of ^{226}U and ^{254}No", *Phys. Rev.* C **69** (2004) 064324

[ICC] Website: http://wwwrsphysse.anu.edu.au/nuclear/bricc/

[In54] D.R. Inglis, "Particle Derivation of Nuclear Rotation Properties Associated with a Surface Wave", *Phys. Rev.* **96** (1954) 1059

[Jo02] G.D. Jones, "Detection of long-lived isomers in super-heavy elements", *Nucl. Instrum. Meth.* A **488** (2002) 471

[JYU] Website: http://www.phys.jyu.fi

[Ka04] H. Kankaanpää *et al.*, "In-beam electron spectrometer used in conjunction with a gas-filled recoil separator", *Nucl. Instrum. Meth.* A **534** (2004) 503

[Kn00] G.F. Knoll, "Radiation Detection and Measurement", *John Wiley and Sons* (2000)

[Kr88] K.S. Krane, "Introductory Nuclear Physics", *John Wiley and Sons* (1988)

[Lam40] W.E. Lamb, "Passage of Uranium Fission Fragments Through Matter", *Phys. Rev.* **58** (1940) 696

[Laz89] Yu.A. Lazarev, "Study of the stability of the ground states and K-isomeric states of ^{250}Fm and ^{254}102 against spontaneous fission", *Phys. Scripta* **39** (1989) 422

[La01] I.H. Lazarus *et al.*, "The GREAT Triggerless Total Data Readout Method", *IEEE Trans. Nucl. Sci.* **48** (2001) 567

[Le95] M. Leino, "Gas-filled recoil separator for studies of heavy elements", *Nucl. Instrum. Meth.* B **99** (1995) 653

[Le97] M. Leino, "In-flight separation with gas-filled systems", *Nucl. Instrum. Meth.* B **126** (1997) 320

[Le99] M. Leino *et al.*, "In-beam study of ^{254}No", *Eur. Phys. J.* A **6** (1999) 63

[Lö68] K.E.G Löbner, "Systematics of absolute transition probabilities of K-Forbidden gamma-ray transitions", *Phys. Lett.* B **26** (1968) 369

[Mö97] J.P. Möller, J.R. Nix and K.-L. Kratz, "Nuclear properties for astrophysical and radioactive ion-beam applications", *At. Dat. Nuc. Dat. Tab.* **66** (1997) 131

[Mn08] S. Moon, *PhD Thesis, The University of Liverpool* (2008)

[Mo04] K. Morita *et al.*, "Production and decay of the isotope ^{271}Ds (Z = 110)", *Eur. Phys. J.* A **21** (2004) 257

[Mü79] G. Münzenberg *et al.*, "The velocity filter ship, a separator of unslowed heavy ion fusion products", *Nucl. Instrum. Meth.* **161** (1979) 65

[Ni55] S. G. Nilsson, *Mat. Fys. Medd. Dan. Vid. Selsk.* **29** (1955) 16

[No94] P.J. Nolan, F.A. Beck and D.B. Fossan, "Large Arrays of Escape-Suppressed Gamma-Ray Detectors", *Ann. Rev. Nucl. Part. Sci.* **44** (1994) 561

[Pa05] J. Pakarinen, "Probing Non-Yrast Structures of ^{186}Pb in a RDT Measurement Employing the JUROGAM Array", *PhD Thesis, University of Jyväskylä* (2005)

[Pa08] J. Pakarinen, *private communication*, jp@ns.ph.liv.ac.uk

[Pa03] R.D. Page *et al.*, "The GREAT spectrometer", *Nucl. Instrum. Meth.* B **204** (2003) 634

[Pau03] E.S. Paul, *postgraduate lecture series, The University of Liverpool* (2003)

[Pau07] E.S. Paul, *private communication*, esp@ns.ph.liv.ac.uk

[Rad95] D.C. Radford, "ESCL8R and LEVIT8R: Software for interactive graphical analysis of HPGe coincidence data sets", *Nucl. Instrum. Meth.* A **361** (1995) 297

[Rag95] P.H. Ragen *et al.*, "High-spin proton and neutron intruder configurations in ^{106}Cd", *Nucl. Phys.* **586** (1995) 351

[Rah07] P. Rahkila, "Grain - A Java Analysis Framework for Total Data Readout", *To be published.*

[Ras59] J.O. Rasmussen, "Alpha-Decay Barrier Penetrabilities with an Exponential Nuclear Potential: Even-Even Nuclei", *Phys. Rev.* **113** (1959) 1593

[Rei79] C.W. Reich, R.G. Helmer and R.J. Gehrke, "Energy levels of ^{250}Cf populated in the β^- decay of ^{250}Bk", *Phys. Rev.* C **19** (1979) 188

[Re99] P. Reiter *et al.*, "Ground-State Band and Deformation of the Z = 102 Isotope ^{254}No", *Phys. Rev. Lett.* **82** (1999) 509

[Re00] P. Reiter *et al.*, "Entry Distribution, Fission Barrier, and Formation Mechanism of $^{254}_{102}$No", *Phys. Rev. Lett.* **84** (2000) 3542

[Re05] P. Reiter *et al.*, " Structure of the Odd-A, Shell-Stabilized Nucleus $^{253}_{102}$No" *Phys. Rev. Lett.* **95** (2005) 032501

[Ri04] P. Ring and P. Schuck, "The Nuclear Many-Body Problem", *Springer-Verlag Berlin*, (2004)

[Ru61] L.I. Rusinov, "Nuclear Isomerism", *Sov. Phys. Usp.* **4** (1961) 282

[Sa96] Š. Šaro *et al.*, "Large size foil-microchannel plate timing detectors", *Nucl. Instrum. Meth.* A **381** (1996) 520

[Se07] D.A. Seddon, *private communication*, das@ns.ph.liv.ac.uk

[So91] V.G. Solv'ev *et al.*, "Desciption of nonrotational states of ^{250}Cf and ^{256}Fm", *Sov. J. Nucl. Phys.* **54** (1991) 1232

[St67] V.M. Strutinsky, "Shell effects in nuclear masses and deformation energies", *Nucl. Phys.* A **95** (1996) 420

[St68] V.M. Strutinsky, ""Shells" in deformed nuclei", *Nucl. Phys.* A **122** (1968) 1

[Sul07] B. Sulignano, "Search for K isomers in ^{252,254}No and ^{260}Sg and investigation of their structure", *PhD Thesis, Johannes Gutenberg University Mainz* (2007)

[Su07] B. Sulignano, private communication, barbara.sulignano@cea.fr

[Su07] B. Sulignano *et al.*, "Identification of a K isomer in ^{252}No", *Eur. Phys. J.* A **33** (2007) 327

[Ta06] S.K. Tandel *et al.*, "K Isomers in 254No: Probing Single-Particle Energies and Pairing Strengths in the Heaviest Nuclei", *Phys. Rev. Lett.* **97** (2006) 082502

[Tr90] W.H. Trzaska, "Recommended data on selected gamma-ray and conversion-electron calibration sources", *Nucl. Instrum. Meth.* A **297** (1990) 223

[Wa94] P.M. Walker *et al.*, "$K^{\pi} = 6^{+}$ and 8^{-} isomer decays in ^{172}Hf and $\Delta K = 8$ E1 transition rates", *Phys. Rev.* C **49** (1994) 1718

[Wa99] P.M. Walker and G. Dracoulis, "Energy traps in atomic nuclei", *Nature* **399** (1999) 35

[Wa05] P.M. Walker, "High-K structures under extreme conditions", *Act. Phys. Pol.* B **36** (2005) 1055

[Wei51] V.F. Weisskopf, "Radiative Transition Probabilities in Nuclei", *Phys. Rev.* **83** (1951) 1073

[Xu04] F. R. Xu, E. G. Zhao, R. Wyss, and P. M. Walker, "Enhanced Stability of Superheavy Nuclei Due to High-Spin Isomerism", *Phys. Rev. Lett.* **92** (2004) 252501